

N 44
5/2/92

**NASA
Technical
Memorandum**

P.91

NASA TM -103578

HIGH ALTITUDE SOLAR POWER PLATFORM

By M.D. Bailey and M.V. Bower

Structures and Dynamics Laboratory
Science and Engineering Directorate

April 1992

(NASA-TM-103578) HIGH ALTITUDE SOLAR POWER
PLATFORM (NASA) 91 0 CSCL 10P

N92-21546

Uncl. is
G3/44 0083775



National Aeronautics and
Space Administration

George C. Marshall Space Flight Center

REPORT DOCUMENTATION PAGE

Form Approved
OMB No. 0704-0188

Public reporting burden for this collection of information is estimated to average 1 hour per response, including the time for reviewing instructions, searching existing data sources, gathering and maintaining the data needed, and completing and reviewing the collection of information. Send comments regarding this burden estimate or any other aspect of this collection of information, including suggestions for reducing this burden, to Washington Headquarters Services, Directorate for Information Operations and Reports, 1215 Jefferson Davis Highway, Suite 1204, Arlington, VA 22202-4302, and to the Office of Management and Budget, Paperwork Reduction Project (0704-0188), Washington, DC 20503.

1. AGENCY USE ONLY (Leave blank)		2. REPORT DATE April 1992	3. REPORT TYPE AND DATES COVERED Technical Memorandum	
4. TITLE AND SUBTITLE High Altitude Solar Powered Platform			5. FUNDING NUMBERS	
6. AUTHOR(S) M.D. Bailey and M.V. Bower*				
7. PERFORMING ORGANIZATION NAME(S) AND ADDRESS(ES) George C. Marshall Space Flight Center Marshall Space Flight Center, Alabama 35812			8. PERFORMING ORGANIZATION REPORT NUMBER	
9. SPONSORING / MONITORING AGENCY NAME(S) AND ADDRESS(ES) National Aeronautics and Space Administration Washington, DC 20546			10. SPONSORING / MONITORING AGENCY REPORT NUMBER NASA TM-103578	
11. SUPPLEMENTARY NOTES Prepared by Structures and Dynamics Laboratory, Science and Engineering Directorate. *University of Alabama, Huntsville				
12a. DISTRIBUTION / AVAILABILITY STATEMENT Unclassified — Unlimited			12b. DISTRIBUTION CODE	
13. ABSTRACT (Maximum 200 words) Solar power is a preeminent alternative to conventional aircraft propulsion. Previously, relatively small solar powered aircraft with limited usefulness have flown for short durations. With continued advances in solar cells, fuel cells, and composite materials technology, the solar powered airplane is no longer a simple curiosity constrained to flights of several feet in altitude or minutes of duration. A high altitude solar powered platform (HASPP) has several potential missions, including communications and agriculture. In remote areas, a HASPP could be used as a communications link. In large farming areas, a HASPP could perform remote sensing of crops. The impact of a HASPP in continuous flight for 1 year on an agriculture monitoring mission is presented. This mission provides farmers with near real-time data twice daily from an altitude which allows excellent resolution on water conditions, crop diseases, and insect infestation. Accurate, timely data will enable farmers to increase their yield and efficiency. A design for a HASPP for the foregoing mission is presented. In the design power derived from solar cells covering the wings is used for propulsion, avionics, and sensors. Excess power produced midday will be stored in fuel cells for use at night to maintain altitude and course.				
14. SUBJECT TERMS Solar Power, High Altitude Platform, Airplane, Agricultural Monitoring			15. NUMBER OF PAGES 91	
			16. PRICE CODE NTIS	
17. SECURITY CLASSIFICATION OF REPORT Unclassified	18. SECURITY CLASSIFICATION OF THIS PAGE Unclassified	19. SECURITY CLASSIFICATION OF ABSTRACT Unclassified	20. LIMITATION OF ABSTRACT Unlimited	

TABLE OF CONTENTS

	Page
PART I. INTRODUCTION	1
Chapter I. INTRODUCTION	1
A. Alternatives to HASPP's	2
B. Proposed Mission	3
C. Reference Mission	4
D. Organization	4
Chapter II. LITERATURE REVIEW	5
PART II. DESIGN METHODOLOGY	10
Chapter III. DESIGN TO REFERENCE MISSION	11
Chapter IV. SOLAR RADIATION	19
Chapter V. SOLAR CELLS	24
A. Solar Array Configuration	25
B. Solar Cell Characteristics	25
C. Semiconductors	26
1. Gallium Arsenide	26
2. Single-Crystal Silicon	27
3. Amorphous Silicon	27
4. Cadmium Telluride	28
5. Copper Indium Diselenide	28
6. Concentrator Solar Cells	28
7. Tandem Solar Cells	28
8. Comparisons Between Cells	28
Chapter VI. CONSTRUCTION	29
A. Detailed Construction of <i>Solar Challenger</i>	30
Chapter VII. AERODYNAMICS	31
A. Equilibrium Flight and Airspeed	33
B. Fluid Statics	35
C. Fluid Dynamics	37
D. Lift and Drag	37
E. Airfoils	39

TABLE OF CONTENTS (Continued)

	Page
Chapter VII. ENERGY STORAGE	43
A. Lead-Acid Batteries	44
B. Nickel-Cadmium Batteries	45
C. Nickel-Hydrogen Batteries	45
D. Silver-Zinc Batteries	46
E. Fuel Cells	47
Chapter IX. PROPULSION SYSTEM	49
A. Motor	49
B. Controller	50
C. Inverter	51
D. Reduction Gearing	51
E. Power Conditioning	51
F. System Efficiency	51
Chapter X. PAYLOAD	52
Chapter XI. AVIONICS	54
Chapter XII. WIND AND ATMOSPHERE STUDY	54
PART III. METHOD OF ANALYSIS	62
Chapter XIII. DESIGN SOLUTION	63
A. Solar Radiation	63
B. Endurance Parameter	64
C. Weights	66
D. Aerodynamics	67
E. Design Specifications	71
F. Mission and Aircraft Specifications	74
Chapter XIV. CONCLUSIONS	77
REFERENCES	80

LIST OF ILLUSTRATIONS

Figure	Title	Page
1.	Design methodology	11
2.	Daily energy balance algorithm	13
3.	Top view of wing (planform)	16
4.	Air mass definition	21
5.	Definition of incidence angle, etc.	23
6.	Forces and moments on an airplane in a steady climb	33
7.	Standard atmosphere	36
8.	Wortmann FX 74-CL5-140; FX 74-CL6-140	40
9.	Drag polar, $C_L(\alpha)$, of the FX 74-MS-150B at Reynolds numbers of 1.5 and 3.0×10^6	40
10.	Wortmann FX 74-CL5-140, FX CL6-140	41
11.	Wortmann FX 63-137	42
12.	Wortmann FX 63-137	42
13.	HASPP power system	52
14.	Wind speeds, Oakland, CA, spring	56
15.	Wind speeds, Oakland, CA, winter	57
16.	Wind speeds, Oakland, CA, summer	57
17.	Wind speeds, Oakland, CA, fall	58
18.	Wind speeds, Vandenberg, CA, spring	58
19.	Wind speeds, Vandenberg, CA, winter	59
20.	Wind speeds, Vandenberg, CA, summer	59
21.	Wind speeds, Vandenberg, CA, fall	60
22.	Daily energy balance algorithm	64

LIST OF ILLUSTRATIONS (Continued)

Figure	Title	Page
23.	Wing loading versus endurance parameter	65
24.	Wing loading versus endurance parameter without payload	66
25.	Wing area versus aspect ratio	68
26.	Wing area versus endurance parameter	70
27.	Critical wind speed	70
28.	Solar versus aerodynamic endurance parameters	72
29.	Solar versus aerodynamic endurance parameters	73
30.	Solar versus aerodynamic endurance parameters	73
31.	Change in flight conditions with time, latitude 36°	75
32.	Change in flight conditions with time, latitude 40°	75
33.	Power required curve	77

LIST OF TABLES

Table	Title	Page
1.	Flight and propulsion parameters	12
2.	Symbols and subscripts	12
3.	Annual variation of solar radiation from orbital eccentricity	20
4.	Coefficients a_0 , a_1 , and k calculated for the 1962 Standard Atmosphere for use in determining solar transmittance t	22
5.	Symbols used in aerodynamic analysis	32
6.	Standard sea level values of atmosphere	35
7.	Standard atmosphere values	35
8.	Fuel cell terminology	43
9.	Lead-acid battery (1982)	44
10.	Rechargeable batteries	46
11.	Wind speeds	55
12.	Design input parameters	63
13.	Initial design specifications using data from Youngblood	71
14.	Final design specifications	74
15.	Summary of design	79

TECHNICAL MEMORANDUM

HIGH ALTITUDE SOLAR POWER PLATFORM

PART I. INTRODUCTION

Chapter I. INTRODUCTION

For years, the feasibility of aircraft with unconventional power sources has been explored. A remotely piloted aircraft, *Sunrise*, made the first unmanned solar-powered flight in 1974 when it flew to an altitude of over 5 km. Human-powered flight was seen with the *Gossamer Condor* and *Gossamer Albatross* first flown in 1977 and 1979, respectively. The *Gossamer Penguin*, a $3/4$ size version of the *Gossamer Albatross*, was fitted with solar cells and first flown with a pilot in 1980. A direct descendent of these aircraft is *Solar Challenger*, a piloted aircraft powered by solar cells that flew in 1980.

The success of these aircraft and the continued increase in solar cell and fuel cell efficiencies have generated an ever increasing interest in solar-powered flight. The National Aeronautics and Space Administration's (NASA's) Langley Research Center (LaRC) and others have investigated unmanned airborne, high-altitude solar powered platforms (HASPP's) designed for long-endurance flight driven by electric propulsion and solar energy collection/storage devices. The HASPP is proposed as an alternative to orbiting satellites, manned aircraft, remotely piloted vehicles (RPV), or balloons. Satellites are limited by the cost and difficulties associated with placing them in orbit as well as the intermittent coverage they provide and the loss of resolution from high orbits. There is also a time delay associated with receiving information from a satellite. Manned airplanes suffer similar constraints in that their coverage cannot be continuous without several airplanes taking shifts, which would be prohibitively expensive. Military RPV concepts, such as the *Compass Cope*, are limited to flights of 24 h or less. The Boeing *Condor*, an unmanned aerial vehicle, is capable of flying up to 2 $1/2$ days continuously. Thus, the current RPV's would be impractical for a number of applications due to their limited flight time. Furthermore, RPV's that are used repeatedly would necessarily have to enter the widely used airspace often. This creates the issue of how to operate them autonomously within the air traffic control system. Observation balloons are limited by the weather conditions in which they can operate, in the altitude they can attain, as well as in ground coverage, since they must be stationary. High-altitude powered platforms (HAPP's) with power sources other than solar energy have been examined, but have not proven to be as practical or to have the endurance capabilities of the HASPP. NASA briefly considered nuclear power and dismissed it. Chemically fueled engines have been examined for use on a HAPP and have been considered a near-term solution for limited endurance flights of only 2 to 3 days. Microwave-powered HAPP's have been examined as well.

The HASPP is a highly flexible tool which is very well suited to a number of missions. In addition to the flexibility of HASPP's, while they are expensive, they are highly cost effective and will become increasingly cost effective as use grows. Another highly significant advantage for the HASPP is that it is nonpolluting. Further, and just as important, HASPP's will fly at altitudes which are above those normally used by conventional aircraft, thus it will not interfere with the routing

operation of conventional aircraft. Moreover, competing vehicles, particularly satellites and reconnaissance aircraft, have very limited availability unlike a HASPP. Finally, the altitude at which a HASPP operates would preclude any loss of resolution due to high orbits as experienced with satellites.

Photovoltaic technology continues to increase and the increases in efficiencies will be coupled with decreases in costs as production is increased and standardized. Thus, it is expected that the cost of producing a HASPP will decrease in the future, following the trend of personal computer prices and other "high-tech" products.

The HASPP lends itself well to a variety of missions by station keeping, i.e., circling at a given location. The Coast Guard could make use of such an aircraft for monitoring coastal boundaries, ice flow, and traffic in the Great Lakes or sea lanes. A HASPP could serve as a communications relay in military or civilian applications such as microwave, ultra high frequency (UHF), and very high frequency (VHF) communications, or cellular telephone systems. One specific civilian communications application is as a high-latitude communications link in remote areas of Canada. Boeing proposes that high-altitude, long-endurance airplanes should be capable of reaching any place in the world and providing remote sensing. Boeing's *Condor* is proposed to be useful in military surveillance, electronic intelligence gathering, arms verification duty, scientific data gathering, weather monitoring, and drug enforcement. The mission proposed in this report is agricultural monitoring over the San Joaquin Valley.

The purpose of this research is to design a high-altitude, solar-powered platform. This report presents the research necessary to determine the components of the aircraft as well as the method of the design. The end results of this study are the specifications, capabilities, and limitations of such an aircraft.

A. Alternatives to HASPP's

All of the missions listed earlier can optimally be performed by remote sensing. The remote sensing equipment must be carried by a vehicle, and a number of such vehicles or vehicle designs exist today. These options are discussed below.

The microwave HAPP would station-keep about a microwave beam or fly between beams. The airplane would climb during exposure to one beam and glide until another beam was intercepted. This would result in a variable ground resolution from the roller coaster flight path. If the HAPP were used for remote sensing of crops, this could present difficulties in obtaining and interpreting the data collected.

The 1983 preliminary design of a chemically fueled HAPP is a turboprop-powered airplane. The fuel would be JP-7 (kerosene), liquid methane (CH₄), or liquid hydrogen (H₂) used in small engines proposed to be available in the 1990's. The maximum altitude obtainable for this design is about 21 km (70,000 ft) based on the engine constraints. The payload has been sized at 91 kg (200 lb), with a total takeoff weight of 1,365 kg (3,000 lb) and a wing span of 26 m (85 ft).

The ER-2, NASA's derivation of the U-2, is capable of obtaining data at altitudes from 60,000 to 70,000 ft. Boeing's *Condor*, first flown on October 9, 1988, is a drone capable of operating altitudes above 65,000 ft for several days at a time. The *Condor* weighs approximately 20,000 lb and is propelled by two six-cylinder, 175-hp, liquid-cooled engines, similar to those on the Scaled

Composites *Voyager*. The fuel is carried in wing tanks and accounts for 12,000 lb of the aircraft weight. This is about 60 percent of the total weight. The unmanned aerial vehicle (UAV) is capable of carrying a sizable payload. During testing, 1,800 lb of instrumentation was flown as payload. *Condor* has a 200-ft wing span with an aspect ratio of 36.6. The wing tips deflect up to 12.5 m (41 ft) from static condition to a 2-g load in flight. The wing tips droop 4.9 m (16 ft) when static. The estimated cost for the *Condor* is \$20 million without the payload, and Boeing suggests that the payload could double the price of the airplane.

B. Proposed Mission

For this research, a mission is proposed for development of a baseline design. The proposed mission is for the Department of Agriculture. In this mission, the HASPP will function as a high-altitude agricultural observation platform. Numerous farming areas have farms of great expanse, fields measured in square miles instead of acres. Due to the size of these fields, inspection of the crops is a practical impossibility. Nevertheless, inspection and observation of the entire field is needed for maximum production. A specific example is the San Joaquin Valley in California. In this area, crop irrigation is heavily used, increasing the importance of crop inspection. Sensors on the HASPP will give thermal images that provide information on water conditions, crop diseases, and insect infestation.

In 1983, it was stated that farmers in the San Joaquin Valley pay consultants \$10 per acre (4,047 m²) annually for information relating to water conditions, crop diseases, and insect infestation. It is not likely that this information could be provided with a frequency greater than once a week. These consultants typically make observations from a ground vehicle and occasionally walk into a sample field taking random observations. The consultants could fly over the fields in piloted aircraft at relatively low altitudes. Current airborne systems record the data, and a report is sent to the farmer by mail or telephone. A near-future system proposes sending video data from a low altitude aircraft to the farmer in real time. A charged couple device (CCD) camera has recently been developed which results in data within the 0.4-to 1.1-micrometer range. The currently available alternatives to the private consultants are satellites and the U.S. Air Force U-2. The Landsat satellite, first launched into a polar orbit in 1972, provides data on any given area every 18 days, and the U-2 manned airplane can provide a maximum of 6 h of data at 20 km (65,000 ft), meaning that a given area of land would be covered once a day or half that area twice a day. The usefulness of remotely sensed data decays rapidly with time. In order to properly cater to the current needs of a crop, data must be available within minutes. A maximum delivery time for useful data would be a few hours. Data delivered to a farmer 5 days after being collected would be practically useless. The frequency of coverage also decays rapidly with time. A system that provides repeat coverage every 10 to 20 days would be of little use to farmers. Landsat is an appropriate tool for measuring net trends in crop growth and conditions. However, the satellite cannot provide the timely data necessary for agricultural management decisions. In addition, the length of time between images of a given area could easily be doubled if it is cloudy when Landsat makes its pass. If the farmers in a 5,000-km² (1,235,200-acre) area would pay the same as they currently pay ground observers, for twice daily HASPP coverage, over \$10,000,000 per year would be available for operation of the planes and ground station.¹ Twice-daily coverage would provide the timely information necessary for determining when and where to irrigate as well as when to stop irrigation. Furthermore, twice-daily coverage would insure against interruption of data due to cloud cover, also it would allow the crops to be observed at different Sun angles to derive plant canopy data from composite soil scenes.

In the past, such aircraft have proven theoretically impossible due to low solar cell efficiencies, low energy densities of fuel cells, and high structural weight. In more recent years, it has been proposed that a HASPP would be feasible by pushing existing technology to its limits. Such an airplane design is presented in this report.

C. Reference Mission

The proposed flight for a typical HASPP would be a minimum of 1 year in duration. The HASPP would be towed to near position by a balloon, then released and put on course by the ground station using remote piloting techniques. The plane will fly a racetrack course sending agricultural information to the ground station continuously during daylight hours. The ground station will process the data, and farmers will access the data from personal computers. The currently available agricultural sensors dictate the flight altitude (20 km or 65,600 ft) and racetrack width. The design altitude is also above weather and falls within the altitude range of relatively calm winds (discussed in chapter XII). The radius or half width of the course will be half the scan width of the sensors, and the length will be dependent on the speed of the aircraft, using the constraint that the course be completed in 6 h in order to provide twice-daily coverage for any given area. The speed of the aircraft must be sufficient to overcome 90-percentile winds at altitude.

The power to propel the aircraft and operate the avionics and payload during daylight hours is supplied by the solar cells on the airplane's wings and horizontal tail. Excess power produced during the peak hours of sunlight is stored in rechargeable batteries or fuel cells to be used at night to maintain altitude and course. For brief periods around sunrise and sunset, a combination of stored energy and converted sunlight will be used.

After approximately a year of service, the HASPP will be brought down for maintenance, dependent on the lifetime of the Mylar covering. A time of light winds will be chosen for the landing, and the craft will be brought in and landed like a glider.

D. Organization

Part I of this report provides a preface to the subject of the research. A background study of a HASPP and its need is presented, with a comparison study of the alternate methods of accomplishing those needs. A particular purpose for the HASPP is selected, that mission is outlined, and the specifications of the HASPP for that mission are discussed. Part I concludes with a review of the literature examined for this report.

Part II consists of an outline of the design process, discussions of each of the aircraft components, and other studies necessary for the operation of a HASPP. This section lists the characteristics of several options for each subsystem needed in the aircraft.

Part III contains the design of the aircraft with the components chosen from part II. The design is discussed in detail with the specifications necessary to meet the proposed mission. Some performance characteristics of the aircraft are considered, and the general airplane configuration is presented. The conclusions examine the usefulness of the design HASPP for the mission proposed and for extended missions.

Chapter II. LITERATURE REVIEW

The following section is a discussion of the literature reviewed for this report. The literature reviewed is a compilation of papers, articles from journals, sections from books, personal interviews, and correspondence. The following review addressed the subjects of design methodology, mission requirements, solar radiation, solar cells, aircraft structure, aircraft aerodynamics, motor/controller, fuel cells, payload, and avionics.

Henderson² writes about the Boeing *Condor*, an unmanned aerial vehicle capable of flying autonomously at altitudes above 65,000 ft for several days continuously. The *Condor* is made of a composite structure with wing loadings just slightly higher than the solar powered airplanes that have flown. The flight control system for the *Condor* is also discussed along with an estimated cost.

Kuhner, Earhart, Madigan, and Ruck³ list a number of possible missions for a HAPP in the paper "Applications of a High-Altitude Powered Platform (HAPP)." Forest fire detection, ice mapping in the Great Lakes, communications, and enforcement of the 200-mi fisheries zone are discussed. The paper discusses the usefulness of the various missions, relative merit, and the cost of using a HAPP as compared to satellites and/or airplanes.

Morris⁴ gives a comparison of a HAPP's performance to that of satellites. The paper concludes that a HAPP would offer better observation resolution than satellites, local persistence, and capability of reuse. The paper also lists several possible missions including Earth-resource monitoring, atmospheric sampling, and surveillance.

Graves⁵ explored the feasibility of a solar HAPP in 1982. Information on batteries, fuel cells, and motors was taken from this document. The batteries examined were nickel-cadmium and nickel-hydrogen couples, and the fuel cell was a hydrogen oxygen system. Rare Earth magnet motors were discussed, in particular, the samarium cobalt electric motor.

"Solar-Powered Airplane Design for Long-Endurance, High-Altitude Flight" by Youngblood and Talay⁶ is the baseline for this report. Reference 6 presents a design methodology for a solar-powered aircraft with a mission similar to that proposed here. The equations Youngblood and Talay used for sizing an aircraft will be used in this report, however, the mission characteristics and power train characteristics will be different, due to advances in technology.

Stender⁷ presents equations and sample calculations which are used in the design methodology. A HASPP is similar in configuration to a sailplane, thus the airframe weight loading for a HASPP is estimated using methods proven for sailplanes. Wing geometry is discussed in the paper as well as the airplane sizing information.

MacCready, Lissaman, Morgan, and Burke⁸ discuss previous attempts at solar-powered flight. *Sunrise II*, the Gossamer series, and *Solar Challenger* are examined. This paper gives a detailed description of the construction of *Solar Challenger*, the tests that were performed on all the aircraft components, lessons that were learned during the flights, and suggested improvements.

Stansell⁹ discusses the construction and performance of *Solar Challenger*. The article lists the materials used in making the aircraft structure. Solar cell technology is discussed, with a variety of semiconductors and substrates being listed. Further, thin-film manufacturing techniques for solar cells are examined.

Boucher¹⁰ gives a more detailed description of the components and characteristics of *Sunrise II*. *Sunrise II* is an unmanned solar-powered airplane with a wing loading of 1.22 kg/m² (0.25 lb/ft²) and a gross weight of 10.35 kg (22.8 lb). Wing and fuselage construction are outlined in the paper along with the solar power and propulsion systems.

Another solar-powered aircraft design is presented in Youngblood and Talay's 1984 paper.¹¹ The aircraft proposed in this paper differs from that in Youngblood's previous paper in that it is designed for a shorter duration of flight and hence is smaller and has a nonregenerative fuel cell. This paper also presents useful information on the structure of the craft and the design process. It gives data on the avionics and on the payload for an agricultural mission.

Youngblood, Darrell, Johnson, and Harriss¹² presented a general design for a HAPP. Their paper concluded that a long endurance HAPP was not feasible at that time, being 1979. The limitations chiefly were high material and structural weights and the lack of a proven propulsion system.

Parry¹³ presents another solar HAPP design. The possible missions proposed for the aircraft are communications relay, weather related sensors, geophysical measurements, ballistic missile early warning, and aircraft tracking. The conclusion at that time, which was 1974, was that the plane was infeasible with current technology due largely to the relatively high weight of the structure.

Hall, Fortenbach, Dimiceli, and Parks¹⁴ for Lockheed under contract to NASA conducted a preliminary study of solar-powered aircraft and associated power trains. In the resulting paper, solar radiation is discussed at length, as well as propeller design and single versus multiple propeller performance. Motor/controller and gearbox designs are given in the paper. The structure of the aircraft is also discussed, claiming that a wire-braced structure is preferable to cantilevered wings. This conclusion is contrary to the other solar airplane designs.

Hall and Hall¹⁵ of Lockheed produced another report on solar powered aircraft for NASA. In this report, the sizing of the structural members of a HASPP was done. The report resulted in the detailed weight and size of all the members necessary to the structure of a HASPP airframe.

An agricultural monitoring mission is discussed in Youngblood and Jackson's¹ 1983 paper. The paper provides information on the sensors necessary to do thermal imaging of crops. A cost analysis is presented for a typical mission profile. A comparison of coverage between a HAPP and the alternatives (manned airplanes, satellites, and ground observation) was performed. The paper also lists another possible mission for an unmanned solar-powered aircraft, the monitoring of the Gulf Stream for commercial fishermen or shipping interests.

Jackson and Youngblood¹⁶ propose the advantages of a solar HAPP for agricultural monitoring. This paper is a good source of information on the agricultural sensors needed in the HAPP. A basic design, launch, and mission are discussed, suggesting a launch site of Palestine, TX, due to the amount of information the U.S. Weather Bureau can provide for this area and a launch time of 3 a.m. due to minimal winds at that time. A comparison is presented between the Landsat satellite and a solar HAPP.

Jackson¹⁷ presents a detailed study of the plant characteristics that can be obtained through remote sensing. Various remote sensing systems and past, current, and proposed methods of employing those systems are discussed in his paper. Jackson writes about the wavelengths

necessary to collect various information on crops, as well as the optimum time, altitude, and resolution to collect this data.

Bill Barnes¹⁸ was interviewed on the agricultural sensors that could be used on the HASPP. He discussed the advanced solid-state array spectroradiometer (ASAS) and its performance characteristics. The ASAS was determined to be the payload for the HASPP, and the spatial resolution, field-of-view, size, and weight of the package were given.

Background information on the concentrator solar cells is provided by reference 19. The Solar Energy Research Institute (SERI)²⁰ presents detailed and current data on gallium arsenide, copper indium diselenide, cadmium telluride, and amorphous silicon thin film cells, as well as the leading crystalline cells. Record-breaking efficiencies were registered along with some of the characteristics and manufacturing methods for the cells. In addition, the summary listed the company names and addresses that have made record-breaking efficiencies in their solar cell research.

Zweibel²¹ discusses the basic operation of solar cells and some of the potential improvements, such as the coupling of solar cells and room-temperature superconductors.

Irving and Morgan²² suggest methods of constructing cell arrays for use on airplanes. The paper also provides some background information on voltage and current properties of cells. The paper goes on to provide extensive information on solar radiation calculations, the properties of silicon solar cells, and the design and construction of a solar-powered aircraft. The paper concludes that a machine capable of flying several hours per day in favorable conditions is feasible, but the cost would be high and the payload small.

Keith and Frank²³ are another source of solar radiation data. Calculations that are presented in other resources are detailed in this book. The air mass, transmittance, and radiation calculations presented are used in this report to determine the operating conditions for the HASPP.

Vogt and Proeschel²⁴ outline the design of solar arrays for space applications. The paper details the substrate, cells, wiring, and electrical components within an array.

“Space Station Battery System Design and Development”²⁵ discusses the characteristics of the nickel-hydrogen batteries proposed for use on the space station.

Hubbard²⁶ discusses how a solar cell operates, power losses in cells, and cell limitations. The article goes on to list the possible advances in photovoltaic technology, the bandgaps, and other properties of polycrystalline and gallium arsenide cells.

Information on various solar cells was obtained from a number of manufacturers. Stan Vernon²⁷, a representative of Spire Corporation, Gary Virshup²⁸ of Varian, and Ronald Gale²⁹ of the KOPIN Corporation have responded with data on gallium arsenide solar cells. ARCO Solar, Inc.,³⁰ has provided information on the newest copper indium diselenide and amorphous silicon thin film cells, and the University of New South Wales³¹ forwarded information on crystalline silicon cells. These companies and the university were listed in the Photovoltaic Energy Program Summary²⁰ as having produced solar cells with record-breaking efficiencies. The efficiencies, the temperature and air mass associated with the efficiency, sizes, and various other solar cell characteristics are discussed in this correspondence.

Regarding the components of a HASPP, airfoils with high lift characteristics are examined by Wortmann.³² Four different airfoils are compared, giving lift coefficients and endurance parameters.

Althaus³³ provides illustrations of several airfoil cross sections. The characteristics of a variety of airfoils are compared in graphs of drag polars.

Ghia, Ghia, and Osswald³⁴ analyze the Wortmann FX 63-137 airfoil. The airfoil is assumed to be used in a low Reynolds number regime, and the flow of air over the airfoil is studied. Wo and Covert³⁵ also examine the Wortmann FX 63-137 airfoil in the low Reynolds number range. Corning³⁶ lists equations for lift and drag for subsonic flight in terms of the lift and drag coefficients. A method for determining the total drag coefficient is given, also a discussion of the lift coefficient in terms of airplane weight, Mach number, wetted area, and pressure ratio is presented.

McCormick³⁷ provides the equations needed to analyze airplane aerodynamics. Among the topics in the book are airspeed calculations, lift and drag ratios, and wing geometry.

Von Mises³⁸ furnishes aircraft performance equations and aircraft design methods. The entire range of aerodynamics is expressed from an examination of the atmosphere to aircraft control and stability.

Liebeck³⁹ discusses the airfoils designed by Wortmann and their application on modern high performance sailplanes. Wortmann's work is also mentioned by Miley⁴⁰ along with a history of the NACA airfoil series.

A variety of batteries will be considered in this research. Four different rechargeable batteries are compared in the paper by Karpinski.⁴¹ The cells examined are nickel-cadmium, nickel-hydrogen, and two silver-zinc cells. These cells range in energy density from 18 to 77 percent Wh/lb.

Paul Prokopius⁴² of NASA's Lewis Research Center (LeRC) was interviewed about fuel cells. The components of fuel cells were discussed, including weights and dimensions. The fuel cells in use on the space shuttle and those proposed for use on the Martian mission were also discussed. Tom Maloney⁴³ of Sverdrup Technology, Inc., at LeRC was interviewed about fuel cells and stated that realistic fuel cell efficiencies are still on the order of 65 percent.

Bechtel National, Inc.,⁴⁴ developed the "Handbook for Battery Energy Storage in Photovoltaic Power Systems." Many of the terms common to fuel cell technology are defined in this source. The characteristics of lead-acid and nickel-cadmium batteries are also given.

Haas and Chawathe⁴⁵ give the specifications of an 81 Ah battery design for use in space. The design life cycle is 38,000 cycles, the assembly mass is 110 kg (242 lb), and it has an average discharge voltage of 37.5 V minimum.

Jeff Brewer⁴⁶ of the NASA's Marshall Space Flight Center (MSFC) was consulted on battery energy storage systems. Brewer provided a model for sizing a battery system as well as data on nickel-hydrogen and silver-zinc batteries.

The graduate students at the Harvard Business School⁴⁷ prepared a study of fuel cells that provided a detailed look at fuel cell construction and operation. The book lists the possible components for fuel cells and explains the way in which electricity is produced.

Appleby and Foulkes⁴⁸ discuss the history and evolution of fuel cells. They also provide an explanation of how a fuel cell operates.

Roy Lanier⁴⁹ of MSFC was consulted on batteries for use in a HASPP. He was able to suggest four candidate batteries and their relative energy densities.

Curran and Faulkner⁵⁰ present the specifications of the motor used in the electrically powered Air Force XBQM-106 remotely piloted vehicle (RPV). The motor is capable of a maximum of 7,830 W (10.5 hp) and 3,730 to 4,480 W (5 to 6 hp) continuous with a variable motor speed of 6,700 r/min maximum. Sundstrand Corp., of Rockford, Illinois, was the manufacturer of the motor/controller, and a letter⁵¹ dated October 24, 1989, gives more current information.

Spotts⁵² provides the necessary calculations for power and work produced by the electric motor. Horsepower and watts are defined in relation to each other.

Cary Spitzer⁵³ of LaRC was interviewed about the avionics power and weight requirements. Spitzer suggested that weight and power estimates used for RPV of 1,000 lb or greater would approximate the HASPP requirements. The weight and power demands would be 3 percent and 6 W/lb, respectively, for modular avionics.

An examination of the winds the HASPP will encounter during the duration of its flight was made possible with a paper by Thomas W. Stragnac⁵⁴. In this paper, the winds at altitudes from the surface to 10 millibars are graphed for each season and for a variety of locations. The results of the study are favorable to the present HASPP design, showing that high altitude winds were minimum between 18 and 22 km of altitude.

Turner and Hill⁵⁵ supply wind information from synthetic wind profile calculations and from radiosonde data. Their information gives an altitude range for minimum wind speeds and the wind speeds at certain locations for a variety of percentages of time.

The U.S. Air Force⁵⁶ provides detailed data on the atmosphere content, as well as the various stages of the atmosphere. They offer definitions of terms used in the solar engineering calculations. In addition to a variety of information on the effects of atmospheric particles, the effects of ozone are explained.

William H. Phillips⁵⁷ and James W. Youngblood⁵⁸ of LaRC were interviewed about their previous solar HAPP designs. They suggested some areas of possible interest for solar aircraft: the Department of Agriculture, the Coast Guard, the military, and the Canadian government. Some of the ground work for this report came from their suggestions, such as: the length of duration of the mission, the methods for launch and recovery of the craft, and the basic design process. They also provided sources for more information on the subject.

Tom Nelson⁵⁹ of Dupont was consulted regarding Mylar sheeting, proposed for use as the aircraft covering. The thickness and weight of Mylar was discussed, as well as the transmittance of the transparent Mylar and the ultraviolet light resistant coating available.

PART II. DESIGN METHODOLOGY

It is quite common in engineering to deal with problems which are well defined, where the number of unknown variables equals the number of independent equations and the system is solvable. On the other hand, in the design of engineering systems, it is also quite common to be faced with ill-defined problems; problems which may be over or under constrained, and hence not solvable in a classical sense. Further, the object of design is not merely to produce a design, but rather to produce the "best" design, where "best" is a term which is defined in some optimal sense. Therefore, to develop a HASPP which meets the mission profile and is the best design, many different factors must be taken into consideration. The design process presented here⁶ is an iterative process in which all of the characteristics of the HASPP are related to each other. There will be, however, an optimum design which takes into account all of the subsystems of the plane: energy storage; the powerplant consisting of the solar cells, their associated wiring, and the motor/controller; avionics; payload; the structural makeup and materials used in the craft; solar radiation as the power source; and the aerodynamics of a HASPP. This iterative procedure for determination of the optimum design is outlined in this section.

A HASPP with the mission profile presented earlier will be designed based on the assumptions that flight is in the Northern Hemisphere and between 32° and 38° latitude at an altitude of 20 km (65,600 ft). The HASPP is to be designed for level, unaccelerated flight; launch and recovery are not dealt with in this section. Operation of the payload, avionics, and remote piloting will be treated in chapters VIII and IX of this report. The design requirements of flight in the Northern Hemisphere and the latitude restrictions allow for the San Joaquin Valley mission proposed earlier.

The airplane design procedure is illustrated in figure 1. The three categories of input parameters are the flight and propulsion system parameters, the payload weight, and the aerodynamics data. The following discussion describes the specific processes associated with the steps shown in figure 1.

The mission and power train characteristics are used in the daily energy balance algorithm, as shown in figure 1, to compute the wing loading as a function of the endurance parameter. The endurance parameter is defined as $C_L^{3/2}/C_D$ where C_L is the coefficient of lift and C_D is the total drag coefficient.

The output from the daily energy balance algorithm and the payload weight are used in the airplane sizing algorithm as shown in figure 1. The sizing algorithm yields the wing's aspect ratio as a function of wing area, airframe weight, and ultimate load factor. The aspect ratio determines the wing span and wing loading.

The aerodynamics algorithm computes the endurance parameter based on estimated vehicle aerodynamics. Referring again to figure 1, this algorithm incorporates the input parameters from the aerodynamics data and the output from the sizing algorithm.

The procedure at this point is to compare the maximum computed endurance parameter from the aerodynamic algorithm with that required by the energy balance algorithm. If no match exists, a new wing area (and aspect ratio) is chosen. The calculations performed in the sizing algorithm are then repeated and a new endurance parameter function is produced. The smallest wing area to

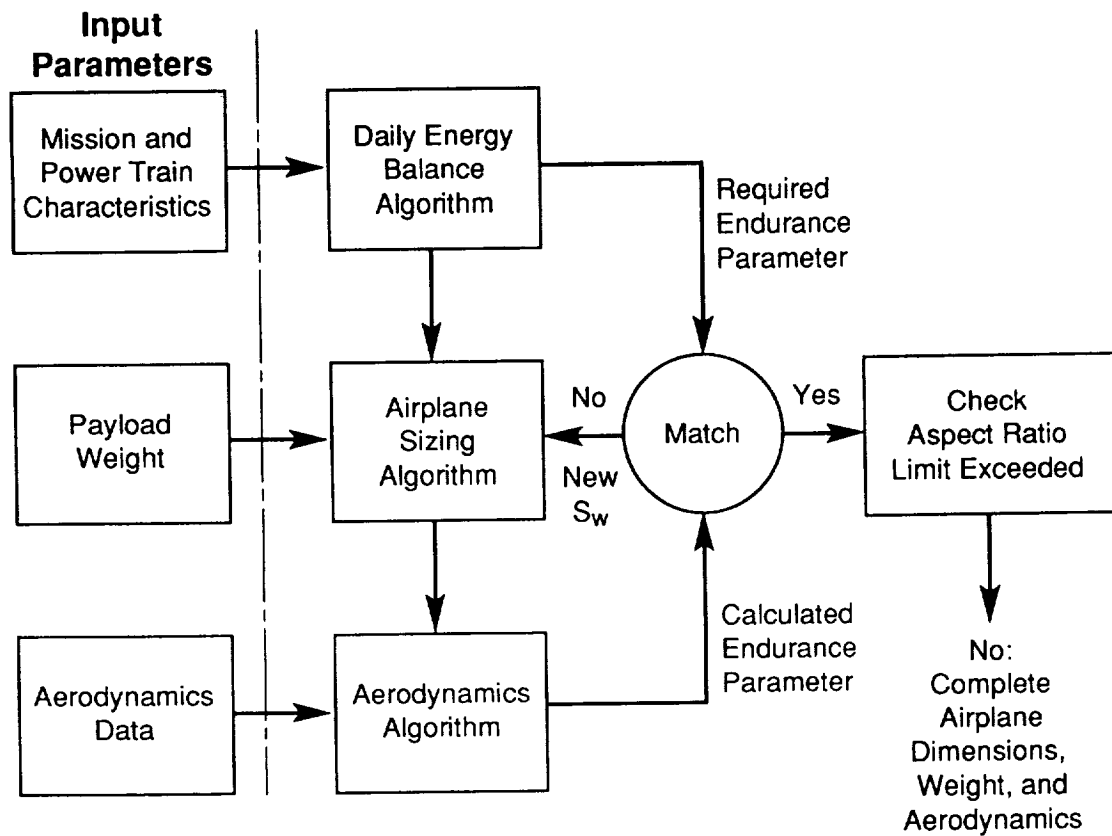


Figure 1. Design methodology.

produce an endurance parameter equality is designated a minimum area for equilibrium solution. There will be a specific wing aspect ratio associated with this endurance parameter equality. Based on a study of current sailplanes, an upper limit of 30 is imposed on the aspect ratio. If the aspect ratio exceeds this limit, a new wing loading is chosen and input to the daily energy balance algorithm. The procedure then continues as before.

In addition to the requirements presented in figure 1, a restriction is imposed on the wing area of 651 m² (7,000 ft²). By comparison, a C5A has a wing area of 576.6 m² (6,200 ft²). Furthermore, the lift coefficients limited by a requirement to station keep against 90-percentile winds. Endurance parameters must not violate this requirement.

Chapter III. DESIGN TO REFERENCE MISSION

As indicated, the purpose of the research is to design a HASPP for agricultural monitoring over the San Joaquin Valley. The input parameters are further subdivided into flight and propulsion system parameters. The flight parameters used in the design include cruise altitude, latitude, mission duration, and payload power requirements. The propulsion system parameters consist of the subsystem efficiencies (propulsion system, solar cells, and fuel cells) and power allocations for systems other than payload and propulsion. Table 1 lists the flight and propulsion parameters for the proposed flight taken from the following chapters. Table 2 is a list of the symbols and subscripts used in the design.

Table 1. Flight and propulsion parameters.

Cruise Altitude, H ; km (ft)	20 (65,600)
Latitude	36
Mission Duration	1 calendar year approximately
Payload Power, P_{pl} ; Watts (hp)	200 (0.27)
Propulsion Efficiency, η_{prop}	76.18 percent
Solar Cell Efficiency, η_{sc}	21 percent
Fuel Cell Efficiency, η_{fc}	65 percent
Avionics Power, P_{av} ; Watts	6 W_{av}
Avionics Weight, W_{av} ; lb	0.03 W_{tot}

Table 2. Symbols and subscripts.

<u>Symbols</u>	
m	air mass
b	span, m (ft)
F	specific energy, W-h/kg (hp-h/lb)
AR	aspect ratio
C_D	drag coefficient
n	ultimate structural load factor
P	power, W (hp)
S	area, m^2 (ft^2)
T_D	fuel cell discharge time, hours
V	velocity, m/s (ft/s)
W	weight, kg (lb)
η	efficiency
A	solar elevation angle, degrees
ρ	atmospheric density, kg/m^3 (slugs/ ft^3)
T	fraction of free space energy incident on horizontal surface
D	drag
<u>Subscripts</u>	
af	airframe
b	booms
e	equilibrium
fc	fuel cell
p	pod
sc	solar cells
t	tail
tot	total
w	wing
$prop$	propulsion
re	required
pl	payload
av	avionics
$wind$	wind
$para$	parasite

The goal of the design methodology is to compare all of the parameters and determine if stable flight is feasible under the prescribed conditions. The airplane is defined to be in equilibrium when there is an energy balance between the available solar power per unit area and the required total power per unit wing planform area. When the airplane is in equilibrium, it is said that it cruises at an equilibrium altitude. Equilibrium conditions are shown by the sketch in figure 2, describing the daily energy balance algorithm. Figure 2 illustrates the power produced and the total power consumption for any particular day.

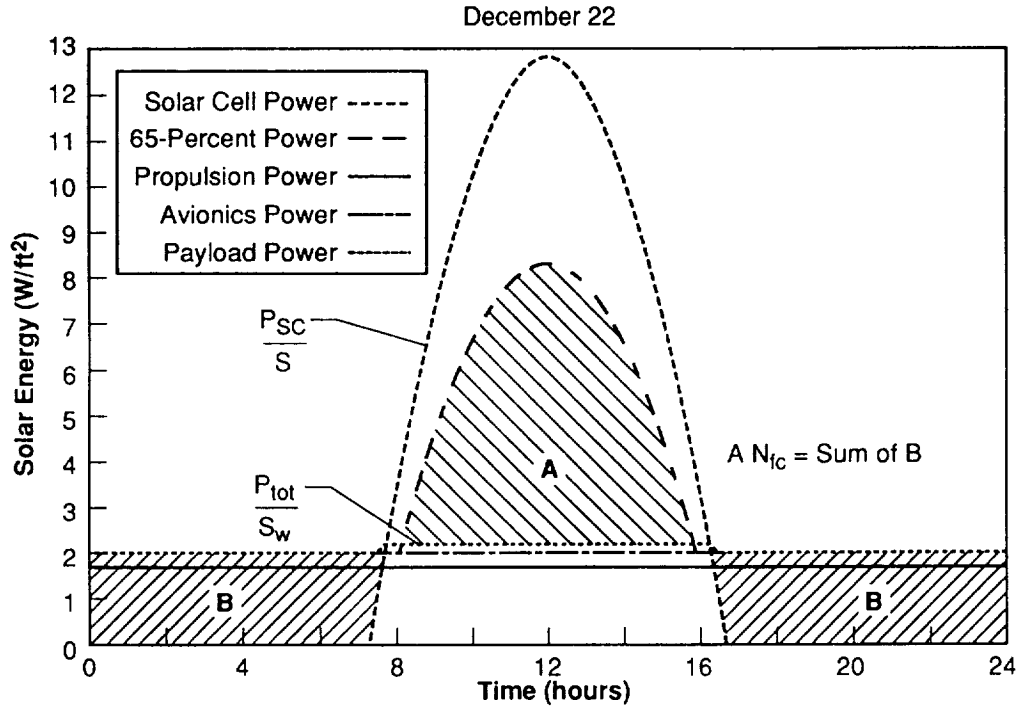


Figure 2. Daily energy balance algorithm.

The total power required for flight is:

$$P_{tot} = P_{prop} + P_{av} + P_{pl} \quad (1)$$

The avionics power, P_{av} , is the power component required for maneuvering flight and vehicle control. The payload power, P_{pl} , is the power component required by the payload and all of its functions. For the mission proposed here, the payload will be the agricultural sensors, and the payload power requirements will include data handling and transmission.

The power produced by the solar cells, P_{sc} , is a function of the solar constant, the atmospheric transmittance, the efficiency of the solar cells, and the solar elevation angle. It is given by:

$$P_{sc}/S = 1,353 T \eta_{sc} \sin A \quad (\text{W/m}^2) \quad (2)$$

The atmospheric transmittance or the fraction of free-space radiation is discussed in chapter IV. The solar constant, $1,353 \text{ W/m}^2$ (125.8 W/ft^2), is the amount of solar radiation available at the edge of the atmosphere computed for all wavelengths. Equation (2) may be evaluated to produce P_{sc}/S as a function of time as shown in figure 2. In figure 2, the total power area B must be provided by the fuel cell to maintain equilibrium flight, while area A represents the total power per unit area produced by

the solar cells above what is required to maintain flight. This solution accounts for both stored energy and direct energy from the solar cells being used during brief periods at sunrise and sunset. Equilibrium conditions exist when:

$$(\text{area A}) (\eta_{fc}) = \text{the sum of (area B)} \quad . \quad (3)$$

Minimum design specifications require that the energy balance calculation be performed for the day of least available solar radiation, December 22.

The power required to maintain cruise flight is defined as :

$$p_{\text{prop}}/S_w = (2/\rho)^{1/2} (W_{\text{tot}}/S_w)^{3/2} (C_D/C_L^{3/2}) (1.356/\eta_{\text{prop}}) \quad , \quad (4)$$

where the constant 1.356 converts ft-lb/s to Watts using an English system of units. In typical airplane design, the power required is given as a function of the velocity of the vehicle and its total drag. Equation (4) is derived in the following manner:

Assuming:

$$\text{Lift} = \text{Weight}/\cos(\alpha) \quad (5a)$$

(where $\cos(\alpha)$, the angle of incidence, is ≈ 1)

$$\text{Lift} = (\rho/2) (V^2) (S_w) (C_L) \quad (5b)$$

$$\text{Drag} = (\rho/2) (V^2) (S_w) (C_D) \quad (5c)$$

$$P_{re} = (V) (D) \quad . \quad (5d)$$

Combining equations (5a) and (5b) yields:

$$V = [(2W)/(\rho S_w C_L)]^{1/2} \quad , \quad (5e)$$

and substituting equation (5c) into (5d) yields:

$$P_{re} = (\rho/2) (V^3) S_w (C_D) \quad . \quad (5f)$$

Now, combining equations (5e) and (5f) results in:

$$P_{re} = (\rho/2) [2(W)/\rho(S_w) (C_L)]^{3/2} (S_w) (C_D) \quad ,$$

or

$$P_{re} = [2/\rho]^{1/2} W^{3/2} [1/S_w^{1/2}] C_D/C_L^{3/2} \quad ,$$

which is equation (4) when divided by S_w and multiplied by the propulsion system efficiency factor.

Equations (1) and (4) can be combined to give the total power required per unit wing area as:

$$P_{\text{tot}}/S_w = (2/\rho)^{1/2} (W_{\text{tot}}/S_w)^{3/2} (C_D/C_L^{3/2}) (1.356/\eta_{\text{prop}}) + P_{\text{av}}/S_w + P_{\text{pl}}/S_w . \quad (6)$$

Equation (6) can also be written as a wing loading:

$$W_{\text{tot}}/S_w = [(P_{\text{tot}}/S_w - P_{\text{av}}/S_w - P_{\text{pl}}/S_w) (\rho/2)^{1/2} (C_L^{3/2}/C_D) (\eta_{\text{prop}}/1.356)]^{2/3} . \quad (7)$$

Equation (7) becomes a function of the endurance parameter, when the mission requirements and the calculated P_{tot}/S_w are incorporated:

$$W_{\text{tot}}/S_w = f(C_L^{3/2}/C_D) . \quad (8)$$

The solution of equation (8) will result in a curve of the endurance parameter versus the wing loading. This curve is used in the airplane sizing algorithm.

The sizing algorithm results in the weights, wing span, and wind aspect ratio of the HASPP. An estimation of the weight is necessary for an analysis of the flight performance, estimation of aircraft center-of-gravity location, and load and stress analysis. "Sailplane Weight Estimation"⁷ employs a statistical method to establish the weight of a sailplane. A HASPP is essentially a powered sailplane; therefore, an airframe weight estimation for manned sailplanes can be used for a HASPP with minimal error.

Figure 3 is an illustration of wing geometry, showing definitions of wing chord and taper. A wing section with a low root thickness and moderate wing taper or rectangular wing planform will result in high empty weight wing loadings. Another design that yields higher wing loadings is a cantilever wing. However, the braced wing causes shading of the solar cells. A cantilever wing adds 10 to 20 percent in material weight over a braced wing.

The empty weight of a cantilever wing airplane can be estimated from:

$$W_E = C_E K_E^{3/8} , \quad (9)$$

where C_E is an empty weight factor and,

$$K_E = n S_w b^3 , \quad (10)$$

where K_E is an empty weight parameter and includes the wing dimensions: ultimate structural load factor, wing area, and wing span. Equations (9) and (10) are combined to give the airframe weight,

$$W_{\text{af}} = A (n S_w b^3)^B , \quad (11)$$

where the constants A and B are evaluated using a regression analysis^{6 11} with data from man-powered airplanes, *Solar Challenger*, and several unpublished high-altitude airplane designs. For ultralight, cantilever wing airplanes, A was calculated as 0.086 and B was 0.357 in Youngblood's 1982 paper⁶ and A as 0.310 and B as 0.311 in Youngblood's 1984 paper¹¹ for ultralight, cantilever, twin-boom tails.

An understanding of wing geometry is needed to complete the sizing algorithm. Referring again to figure 3, the distance from one wing tip to another is the wing span, b . The chord, c , is the distance from the leading edge to the trailing edge measured parallel to the plane of symmetry in which the centerline chord, c_o , lies. The chord will vary along the length of the wing, so a mean chord, c_m , is used. The wing planform area is expressed as:

$$S_w = c_m b . \tag{12}$$

The aspect ratio, AR , is a ratio of the square of the wing span to wing area or,

$$AR = b^2/S_w = b/c = S_w/c^2 . \tag{13}$$

For sailplanes,⁷ the wing chord typically changes with the span to maintain a constant wing area. The aspect ratio is usually proportional to the square of the span for spans up to 15 m (49.2 ft). For spans greater than 15 m, the aspect ratio tends to be proportional to the first power of the span. Figure 3 also illustrates a wing taper or taper ratio, λ , the ratio of the tip chord, c_t , to the midspan chord, c_o . It is:

$$\lambda = c_t/c_o . \tag{14}$$

For sailplanes with wings that are not straight tapered, a taper ratio of root chord, c_r , to mean chord has proven to be more practical.

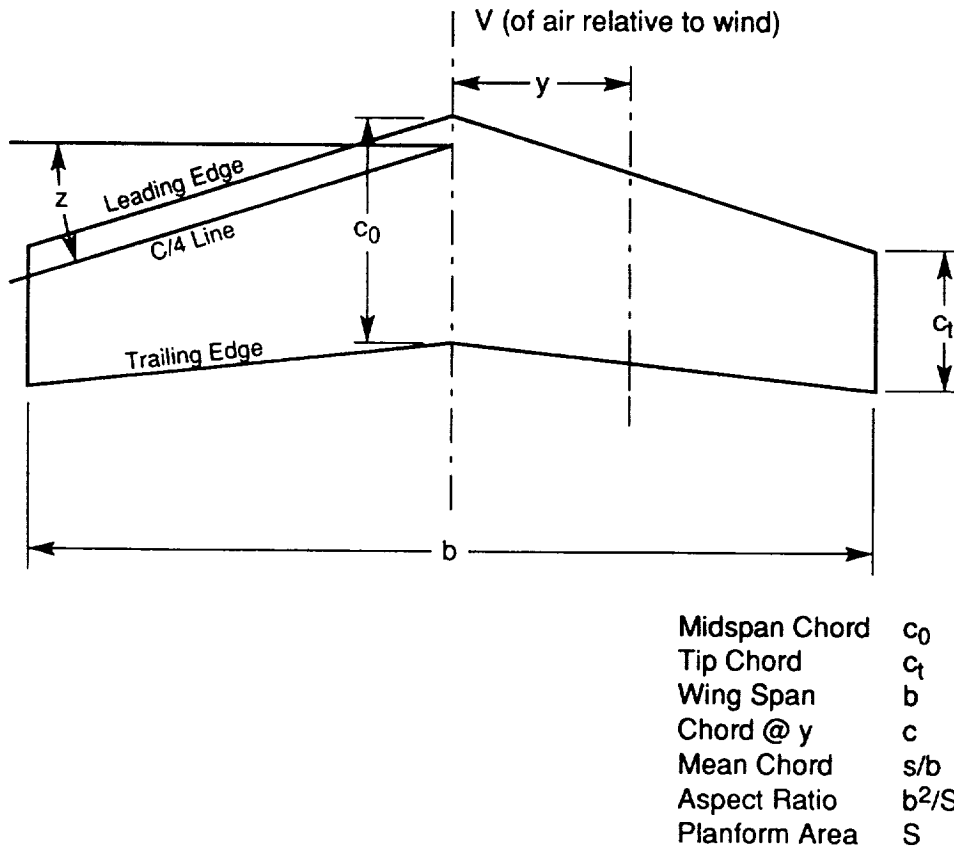


Figure 3. Top view of a wing (planform).

The airframe weight can now be derived from equation (11) as:

$$W_{af} = 0.310 (nS_w b^3)^{0.311} , \quad (15)$$

or, with equation (13) as:

$$W_{af} = 0.310 [nS_w (AR S_w)^{3/2}]^{0.311} . \quad (16)$$

Equation (16) yields the airframe weight loading:

$$W_{af}/S_w = 0.310 [n^{0.311} AR^{0.467} S_w^{-0.222}] . \quad (17)$$

The total airplane weight is determined by summing the airframe weight, propulsion, solar cell, fuel cell, avionics, and payload weights. Based on data in chapter IX, the proposed HASPP will use a samarium-cobalt motor and the propeller design based on that of *Solar Challenger*. Following methods used previously,⁶ the propulsion system weight per unit wing area is scaled linearly with the power requirements by:

$$W_{prop}/S_w = 0.012 P_{prop}/S_w , \quad (18)$$

for a samarium-cobalt motor. The propulsion system includes the motor, controller, inverter, reduction gear, power conditioning, and propeller. The weight loading of the solar cell assembly has previously been estimated as:

$$W_{sc}/S_w = 0.150 S_{sc}/S_w .^6 \quad (19)$$

This estimation is derived from past solar-powered airplanes.^{6 8 10} The ratio, S_{sc}/S_w , in equation (19), includes the solar cells on the horizontal tail as well as the wings. A prior analysis⁶ used a value of 1.0 for S_{sc}/S_w .

For a previous HASPP design,⁶ also with an agricultural mission, the nominal time of discharge, T_D , for the regenerative alkaline fuel cells was given as 13.2 h. A location with latitude within the San Joaquin Valley has a length of night on December 22 of 14:23 h, however, there is 1:26 h of twilight at sunrise and sunset, making the length of total darkness on the ground only 11:31 h. The time of discharge listed above is considered a good assumption. The weight loading for the fuel cell system was given as:

$$W_{fc}/S_w = T_D/F (P_{tot}/S_w) , \quad (20)$$

where F is the specific energy of the fuel cells.

The payload for the HASPP consists of agricultural sensors as discussed in chapter X. Previous designs⁶ have assumed a payload weight of 45.4 kg (100 lb). Expressed as a weight loading, this is:⁶

$$W_{pl}/S_w = 45.4/S_w . \quad (21)$$

The HASPP avionics weight loading, W_{av}/S_w , is given by approximations presented in chapter XI.

The airframe wing loading can be expressed as:

$$W_{af}/S_w = W_{tot}/S_w - W_{prop}/S_w - W_{sc}/S_w - W_{fc}/S_w - W_{pl}/S_w - W_{av}/S_w , \quad (22)$$

where the components of this equation can be seen in equations (18) through (21). This airframe weight loading was also seen in equation (17), which can be written in terms of the aspect ratio as:

$$AR = [(W_{af}/S_w) S_w^{0.222} / (0.310 n^{0.311})]^{2.141} . \quad (23)$$

Substituting equation (22) into equation (24) yields the aspect ratio in terms of airframe weight loading, wing area, and ultimate load factor.

The load factor is the ratio of the load supported by the wings to the actual weight of the aircraft and its contents. The load factor is expressed in "G" units or multiples of the local gravitational constant measured at the Earth's surface. The load on the wings of an aircraft increases in a bank and with aircraft speed. For example, an aircraft in level turning flight with a 60° bank undergoes a centripetal acceleration of 2 G's. Wind gusts will increase the load factor, more so at higher aircraft speeds. The limit load factor is the load factor that an aircraft can sustain without incurring permanent structural damage, while the ultimate load factor is twice the limit load factor. Airplanes certified by the Federal Aviation Administration (FAA) in the normal category are required to have a minimum limit load factor of 3.8, for a 75° bank. Typically,⁷ the ultimate load factor for sailplanes is 8, however, since the HASPP is unmanned and will fly slowly at altitudes above most turbulence, an ultimate load factor of 4 is used here.

The calculations presented in the sizing algorithm are sufficient to determine the dimensions and weights of the HASPP, which are necessary for the aerodynamics algorithm as shown in figure 1.

An endurance parameter based on vehicle aerodynamics must be derived with this algorithm. This endurance parameter should equal or exceed that calculated by the energy balance algorithm. The aerodynamics of the surfaces of the HASPP must be studied in order to calculate the endurance parameter. Due to the low speed of a HASPP, the airfoils will operate in a Reynolds number range of 10^5 to 10^6 .

Typically, the horizontal and vertical tail surfaces operate at low values of C_L . As a result, the induced drag of these surfaces is small. The NACA 0008-34 airfoil has been used in previous designs⁶ for the tail, providing thin, low drag surfaces. The zero-lift tail drag coefficient for this airfoil is:⁶

$$(C_{Do})_t = 0.0075 S_t/S_w , \quad (24)$$

where S_t is the area of both the vertical and horizontal tail surfaces. Since the horizontal tail is oversized to allow for mounting of solar cells on the stabilizer, S_t/S_w was assumed to be 0.36. This value will be used in this design.

The fuel cells, avionics, and payload will be carried in a low-drag pod beneath the center section of the wing. A previous design assumed the pod to have a length-to-diameter ratio of 3 to 1.⁶ For a Reynolds number of 10^6 , this pod has a drag coefficient of 0.06.⁶ This gives a zero-lift drag coefficient for the pod of:⁶

$$(C_{Do})_p = 0.06 S_p/S_w . \quad (25)$$

For a past solar HAPP design,⁶ a twin boom tail configuration was used with an estimated drag coefficient of:

$$(C_{Do})_b = 0.0003 . \quad (26)$$

The drag buildup method allows the component zero-lift drag coefficients to be added together to give the total airplane drag coefficient. The resultant equation is:

$$C_D = (C_{Do})_w + (C_{Do})_t + (C_{Do})_p + (C_{Do})_b + [(1 + \delta)/(\pi * AR)] C_L^2 . \quad (27)$$

The last term in equation (27) is the wing-induced drag where δ is a constant equal to 0.11 for an outer wing panel taper ratio of 0.5. The $(1 + \delta)$ term also refers to an airplane efficiency factor of 90 percent.

With the definition of the endurance parameter and the drag coefficient given by equation (27), the endurance parameter reduces to a function of a single variable, the lift coefficient. This endurance parameter is compared with that obtained from the energy balance algorithm, equation (8) as shown in figure 1. This procedure is repeated until an endurance parameter equality is achieved at the smallest wing area possible. Equilibrium flight will be possible only at the lift coefficient associated with this endurance parameter.⁶ The additional limitations on aspect ratio and wing area, mentioned earlier, must also be maintained for equilibrium flight to exist.

The lift coefficient must enable the HASPP to stay on course against 90-percentile winds. This requirement is:⁶

$$C_L \leq (C_L)_{\text{wind}} = 2 (W_{\text{tot}}/S_w)/(\rho V_{\text{wind}}^2) . \quad (28)$$

When this design procedure is completed with all of the requirements satisfied, the specifications of a feasible HASPP for the given mission will be determined.

Chapter IV. SOLAR RADIATION

A study of solar radiation is instrumental in the calculation of power available to the airplane. The radiation available varies as a function of time throughout the mission as well as a number of other parameters which are determined by the mission profile. Thus, the power available to maintain flight and operate equipment is continually changing. The maximum available radiation changes from minute to minute due to the rotation of the Earth. Further, there is a day-to-day change due to the change of the inclination of the Earth's rotational axis. Optimum aircraft design specifications must be based on minimum solar radiation availability.

At the operating altitude of 20 km (65,600 ft), a HASPP will be above all cloud cover so there will be no daytime interruption of sunlight. The solar radiation, incident on the solar cells of the airplane, is a function of the air mass and the solar-altitude angle. The air mass is defined as the path length of sunlight, or the quantity of atmosphere that solar radiation can pass through, and is equal to the cosecant of the solar altitude angle, A . Air mass is also a function of altitude and is represented by $m(z,A)$ where sea level is given by $z = 0$. The solar-altitude angle is the angle between the incident solar rays and the horizontal. It is a function of the declination of the Sun, the time of year, the time of day, and the latitude.

The average solar radiation received at the edge of the Earth's atmosphere is $1,353 \text{ W/m}^2$ (125.8 W/ft^2), which is defined as the solar constant, I_0 . This represents the total energy in the solar spectrum measured at Earth's mean distance from the Sun. However, the Sun-Earth orbit is elliptical, resulting in a Sun-Earth distance variation of ± 1.7 percent during a year. Because of this, the extraterrestrial radiation also varies slightly by the inverse-square law as shown in table 3. For this analysis, the average value of $1,353 \text{ W/m}^2$ was used.

The wavelengths of the Sun's energy range from 10^{-7} to greater than 10^5 micrometers. The vast majority of the electromagnetic energy from the Sun, 99.8 percent, are wavelengths from 0.22 to 20.0 micrometers. Ultraviolet light has wavelengths less than 0.38 micrometers and accounts for 7.00 percent of the total spectrum, while infrared light is above 0.75 micrometers and accounts for 48.3 percent. The remaining 44.7 percent of the energy has wavelengths between 0.38 and 0.75 micrometers.

Table 3. Annual variation of solar radiation from orbital eccentricity.

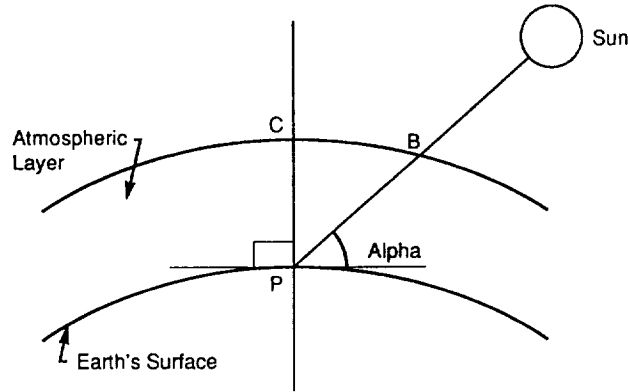
<u>Date</u>	<u>Radius Vector*</u>	<u>Ratio of Flux to Solar Constant</u>	<u>Solar Radiation</u>
Jan. 1	0.9832	1.034	1,399 W/m^2
Feb. 1	0.9853	1.030	1,394
Mar. 1	0.9908	1.019	1,379
Apr. 1	0.9993	1.001	1,354
May 1	1.0076	0.985	1,333
Jun. 1	1.0141	0.972	1,312
Jul. 1	1.0167	0.967	1,308
Aug. 1	1.0149	0.971	1,312
Sep. 1	1.0092	0.982	1,329
Oct. 1	1.0011	0.998	1,350
Nov. 1	0.9925	1.015	1,373
Dec. 1	0.9860	1.029	1,392

*Ratio of Sun-Earth distance to mean Sun-Earth distance.

Bouger's law is used in calculating the atmospheric absorption of solar radiation for clear skies. It is:

$$I_b = I_o e^{-km} \quad , \quad (29)$$

where I_b and I_o are the terrestrial and extraterrestrial intensities of beam radiation, respectively, k is an absorption constant for the atmosphere, and m is the air mass as shown in figure 4.



Alpha = Solar Altitude Angle
 Air Mass = Path Length of Sunlight
 = BP/CP = csc ALPHA = M
 M = 0, Extraterrestrial Radiation
 M = 1, Sun is Directly Overhead
 Atmosphere is Idealized as a Constant Thickness Layer.

Figure 4. Air mass definition.

The solar-altitude angle, A , can be calculated using the law of cosines for spherical triangles. The result is:

$$\sin A = \cos D \cos H \cos L + \sin L \sin D \quad , \quad (30)$$

where D is the declination of the Sun between $+23.5^\circ$ and -23.5° , $D = [23.5 \sin (360 d/365)]^\circ$, or the angle between the Sun's rays and the zenith direction (directly overhead) at noon on the Earth's Equator; d is the time of year in days from the vernal equinox; L is the latitude; and H is the solar hour angle. The solar hour angle is defined as $H = (t/24)360^\circ = 15t^\circ$, where t is the time from solar noon or local solar time in hours.

Atmospheric transmittance, $T_{atm} = (I_b/I_o)$, is a ratio of extraterrestrial solar radiation and solar radiation that has passed through the atmosphere, and it is given by:

$$T_{atm} = 0.5(e^{-0.65m(z,A)} + e^{-0.095m(z,A)}) \quad , \quad (31)$$

where $m(z,A)$ is the air mass at an altitude z above sea level given by:

$$m(z,A) = m(0,A)[p(z)/p(0)] \quad , \quad (32)$$

where $p(z)$ is the atmospheric pressure at altitude z . The sea level air mass is:

$$m(0,A) = [1,229+(614 \sin A)^2]^{0.5} - 614 \sin A . \quad (33)$$

Therefore, the surface beam radiation, I_b , for the clear sky conditions is:

$$I_b = I_o T_{\text{atm}} . \quad (34)$$

Equations (31) and (33) represent an accuracy improvement over equation (29) since they include curvature effects. Equation (31) can be modified to account for particulates and water vapor in the air by:

$$T_{\text{atm}} = a_o + a_1 e^{-k \text{csc } A} , \quad (35)$$

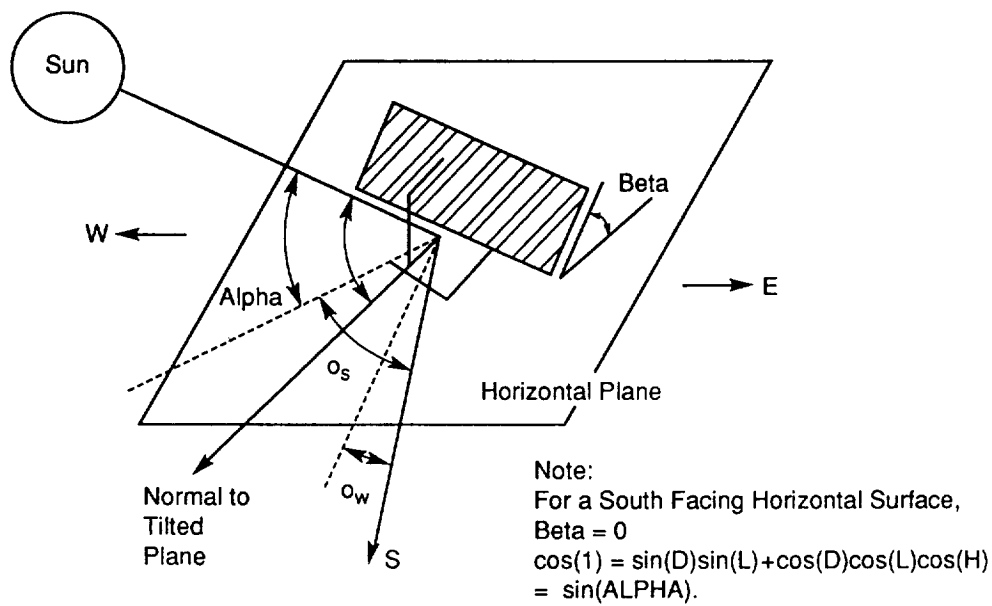
where a_o , a_1 , and k are only functions of altitude and visibility as shown in table 4. The coefficients in the table were calculated for the 1962 Standard Atmosphere. The operating altitude of the airplane in this design renders the use of equation (35) unimportant.

Table 4. Coefficients a_o , a_1 , and k calculated for the 1962 Standard Atmosphere for use in determining solar transmittance t .

		Altitude above sea level (km)					
		0	0.5	1	1.5	2	(2.5)
		23 km haze model					
a_0		0.1283	0.1742	0.2195	0.2582	0.2195	(0.320)
a_1		0.7559	0.7214	0.6848	0.6532	0.6265	(0.602)
k		0.3878	0.3436	0.3139	0.2910	0.2745	(0.268)
		5 km haze model					
a_0		0.0270	(0.063)	0.0964	(0.126)	(0.153)	(0.177)
a_1		0.8101	(0.804)	0.7978	(0.793)	(0.788)	(0.784)
k		0.7552	(0.573)	0.4313	(0.330)	(0.269)	(0.249)
a.		Adapted from Hottel by permission.					
b.		Values in parentheses indicate interpolated or extrapolated values.					

Assuming for discussion purposes that the HASPP is a fixed surface in the atmosphere, the incidence angle is dependent on the basic solar angles, D , H , and L , and on the two angles that characterize the surface orientation, B and a_w . The wall-azimuth angle, a_w , is defined in the same manner as the solar azimuth angle and is shown in figure 5. The solar-azimuth angle can be computed from:

$$\sin a_s = (\cos D \sin H) / \cos A . \quad (36)$$



Definition of Incidence Angle i , Surface Tilt Angle B , Solar-Altitude Angle A , Wall-Azimuth Angle a_w , and Solar-Azimuth Angle o_s
For a Non-South-Facing, Tilted Surface

Figure 5. Definition of incidence angle, etc.

Collector tilt angle, B , is defined as positive for surfaces facing south. For a south facing horizontal surface, $B = 0$. If a tilted surface faces a direction other than due south, the incidence angle, i , may be calculated by:

$$\cos i = \cos (a_s - a_w) \cos A \sin B + \sin A \cos B = \sin A \quad (37)$$

In general, the incidence angle on a planar, fixed surface is

$$\begin{aligned} \cos i = & \sin D (\sin L \cos B - \cos L \sin B \cos a_w) \\ & + \cos D \cos H (\cos L \cos B + \sin L \sin B \cos a_w) \\ & + \cos D \sin B \sin a_w \sin H \quad (38) \end{aligned}$$

Sunrise and sunset are said to occur on a surface when either the surface-incidence angle is 90° or when the altitude angle is zero, whichever occurs closer to solar noon. It is not possible to derive a closed-form equation for sunset or sunrise hour angles because of the complexity of the incidence angle equations. To determine when the Sun sets below the horizon, when $A = 0$, equation (30) is used in the form:

$$\sin A = 0 = \sin L \sin D + \cos L \cos D \cos H_{ss} \quad (39)$$

where H_{ss} is the sunset hour angle for zero altitude. Simplifying equation (39) yields:

$$|H_{ss}| = |H_{sr}| = \cos^{-1} (-\tan L \tan D) \quad (40)$$

where H_{sr} is the sunrise hour angle.

Total beam radiation for given periods of time on a surface is given by:

$$I_{\text{tot}} \int_{t_0+(\delta t)}^{t_0} I_b(t) \cos i(t) dt \quad , \quad (41)$$

where (δt) is the time interval. The function $I_b(t)$ depends on local weather and microclimate. Further, the form of $I_b(t)$ is generally not known. Therefore, equation (41) is not useful. However, it is possible to calculate I_{tot} outside the Earth's atmosphere since $I_b(t)$ is the solar constant multiplied by the orbital eccentricity factor $e(t)$. This is similar to equation (29) and is

$$I_b(t) = e(t) I_o \quad . \quad (42)$$

The orbital eccentricity factor, $e(t)$, may be taken from table 3 or:

$$e(t) \cong 1+0.034 \cos [2\pi n(t)/365] \quad , \quad (43)$$

where n is the number of days from January 1. Combining equations (41) and (42) yields:

$$I_{\text{tot}} \int_{t_0+(\delta t)}^{t_0} I_o e(t) \sin A(t) dt \quad . \quad (44)$$

Thus, equations (30) and (43) combine to give a daily total:

$$I_{\text{day}} = 24/\pi \int_{H_{sr}}^0 I_o [1+0.034 \cos (2\pi n/365)] \sin A dt \quad , \quad (45)$$

where H_{sr} must be in units of radians.

Chapter V. SOLAR CELLS

The choice of solar cells is one of the most important decisions in the design of a HASPP. There are single crystal cells, concentrator cells, tandem and thin film cells, and a variety of cell materials in each of these categories. The chosen cell must have the best combination of efficiency, durability under the mission conditions, bandgap, weight, and life expectancy.

The French physicist, Edmund Becquerel, initially observed the photovoltaic effect in a weak conducting solution in 1839. However, the first solar cell was not produced until 1954 when Bell Laboratory produced a silicon cell with an efficiency of 4 percent. Since then, efficiencies have improved significantly with a number of different semiconductor materials being used to make solar cells. The most common materials are gallium arsenide, cadmium telluride, copper indium diselenide, and crystalline and amorphous silicon. Each of these materials have properties that make them desirable for a particular purpose.

All solar cells have a common configuration, with two or more layers of semiconductor material. The atoms of the semiconducting layers absorb photons of light which free electrons

producing holes to conduct current. The interface of the two different semiconductor materials in the cell creates a voltage potential that propels electrons through a circuit. Some of the limiting factors common to all cells are: the quality of material, shading of the cell by the grid, carrier recombination, light absorption, reflection of light from the cell surface, series and contact resistances, and the fraction of wavelengths of available light that can be absorbed. There are also losses common to most cells that include: band-to-band Auger recombination, emitter recombination, and resistive voltage drops. Many advances have recently been made in photovoltaic cells including transparent conducting oxides, flexible substrates, laserscribed connections, microgrooved surfaces, point contacts, multijunctions, and light-capturing techniques. In addition, improvements such as internal reflection, backsurface reflectors, and antireflection coatings have been made to allow the cells to collect and hold the maximum radiation possible.

A. Solar Array Configuration

Solar cells on a HASPP must be made into an array and placed on or in the wings and horizontal tail. In an array, the cells in series should be matched for current and the cells in parallel should be matched for voltage. Typically, the performance of an array is diminished as the area is increased. However, this may not be true of the gallium arsenide thin films. The 5- to 10-percent power loss found in most thin film modules can be attributed to interconnect area loss and series resistance losses. This is indicative of early stage thin film development and should improve with further research.³⁰ Thirty to fifty cells may be wired together in series to form a module of 0.09 to 0.37 m² (1 to 4 ft²) of area. An arm is composed of several modules and an array is made from several arms. Modules are typically wired in parallel to permit the current to bypass a broken or shaded cell without overloading adjacent cells or shutting off the current from the remaining good cells in that series. *Solar Challenger* used 144×3 cell strings connected through a diode to a panel bus, permitting testing of individual strings. Each panel was protected by a 10-A fuse. The power supply was split into five parts to limit the inrush current.

B. Solar Cell Characteristics

Solar cells are characterized by their efficiency, bandgap, and performance features. Each of these factors is determined by the semiconductor material and the device configuration chosen. The solar array efficiency is used in the calculation of power per unit area produced. This in turn is used as input to the energy balance algorithm, which determines the feasibility of the aircraft. The efficiency of photovoltaic devices is dependent on several parameters. Solar cell efficiency is defined as the ratio of the electrical energy output from a cell to the sunlight energy incident on the cell. The current from a cell increases linearly (approximately) with increasing sunlight intensity. The voltage produced by a cell is approximately proportional to the log of the intensity. Increased current density results in increased resistive losses.

The air mass at which a cell operates is also a factor which affects cell efficiency. A cell will produce more power at higher altitudes and in space than at the surface of the Earth; there are fewer atmospheric particles to block the sunlight. However, the efficiency of the cell is actually lower due to the wider range of wavelengths of light incident on the cell. The semiconductor material in a solar cell has a relatively limited bandgap, or threshold energy at which solar photons are usable. The bandgap is expressed as a range of frequencies or wavelengths to which cells are sensitive. A photovoltaic material will absorb light whose energy is greater than their bandgap. Light with less energy passes through the cell. Essentially, at the surface of the Earth, the solar energy available is concentrated in a comparatively narrow frequency band. For most cells the bandgap of the semiconductor falls within

the band of the available solar energy at the surface of the Earth. As the elevation of the cell increases, the energy available increases inside and outside the bandgap of the cell. The result is that while more total energy is available, the amount of the energy outside the bandgap of the cell increases faster, thus the efficiency of the cell decreases with altitude.

It has been estimated that the efficiency of a silicon cell at AM0 (air mass 0 or space conditions) will be 2 to 3 percent of that at AM1.5, (when the incidence angle of the Sun's rays is 45°). The efficiency of a copper indium diselenide (CIS) cell at AM0 has been evaluated to be 90 percent of the AM1.5 efficiency.

The ambient temperature at which a cell operates affects the efficiency of the cell. As the temperature decreases, the voltage available increases and the current produced decreases. As an example, the efficiency of a CIS cell will increase from 12.4 percent at 25 °C (77 °F) to 19.4 percent at -107 °C (-161 °F).

C. Semiconductors

The most commonly used semiconductor materials are either crystalline or polycrystalline. Gallium arsenide and silicon are used to make single-crystal cells, while amorphous silicon, cadmium telluride, and copper indium diselenide are used to make thin film photovoltaic devices. Gallium arsenide is unique in that it can be used to make single-crystal thin films. Companies that manufacture these photovoltaic devices measure their efficiencies using a solar simulator rather than the solar spectrum. They all publish their results as measured at 25 °C (77 °F) and AM1.5.

1. Gallium Arsenide

The photovoltaic device with the highest efficiency, to date, is the gallium arsenide, Ga-As, single-crystal cell. Ga-As has a bandgap of 1.43 eV at room temperature and the bandgap goes up as the temperature decreases. The efficiency of a 0.5- by 0.5- by 0.051-cm (0.2- by 0.2- by 0.02-in) cell has been recorded at 24 percent. A thin-film, single-crystal Ga-As cell that measures 1 cm² (0.16 in²) by 5 to 6 micrometers (1.97 to 2.36 by 10⁻⁴ in) thick is as flexible as any other thin film device, but since it is a crystal it has a much higher efficiency than polycrystalline semiconductors. A 2-cm² (0.31-in²) Ga-As cell can be manufactured which is over 22-percent efficient. Cells can be made which are as large as 16 cm² (2.48 in²).

KOPIN Corporation manufactures Ga-As cells and claims that their modules are as efficient as the individual cells since they suffer no fill factor losses. Placed on a 51- to 76-micrometer (2- to 3-mil) thick glass substrate, the cell can flex according to the limitations of the glass. It is estimated that a 2-mil thick glass substrate would have a radius of curvature of 2 in. Normally, a cell needs a cover glass to protect the cell and the adhesive. An alternative to using a cover glass is encapsulation of the cell. This process is also called direct glassing and would eliminate the problem of the inflexibility of the cover glass.

Although the cells have not previously been mounted to a plastic, KOPIN believes there would be no problem in mounting the thin films to Mylar. Furthermore, Ronald Gale of KOPIN states that their cells are certified for space use so the thermal cycling of cells at altitude should not be a problem. KOPIN has measured a single-crystal thin film Ga-As cell at 22.4-percent efficiency at

AM1.5. At AM0, the efficiency would be about 21 percent. The cell would consist of a 2- to 4-mil thick glass substrate, 1 to 2 mils of adhesive, $\frac{1}{4}$ mil of Ga-As, and 1 to 2 mils of encapsulation dependent on the radiation present.

Ga-As does not degrade with exposure to sunlight and is more radiation resistant than crystalline silicon. However, it does suffer the drawbacks of being more expensive to manufacture and weighing more per unit area than silicon solar cells. The density of Ga-As is approximately 5.32 g/cm^3 (0.19 lb/in^3).

2. Single-Crystal Silicon

Single-crystal silicon cells are currently the least expensive photovoltaic device to make and at the same time offer relatively high efficiencies. Silicon cells are more widely used than their alternative. They have been in use for a longer period of time, thus, have the advantages of experience with the manufacturing process and larger production capacity. These factors cause the cells to be less expensive than their counterparts.

The University of New South Wales has developed a single-crystal silicon cell with measured efficiencies of 19.6 percent and 20.6 percent under AM1.5 conditions. Some of the 4-cm^2 (0.62-in^2) cells produced have been tested at close to 20-percent AM0 efficiency. The voltage and maximum power output degrades with increasing temperature, from standard temperature (25°C , 77°F), at about $2.3 \text{ mV}/^\circ\text{C}$ and $0.1 \text{ mW}/^\circ\text{C}$, respectively. Crystalline silicon has a bandgap of 0.8 micrometers, it is insensitive to light below 0.25 micrometers and above 1.2 micrometers.¹⁴

3. Amorphous Silicon

Amorphous silicon (a-Si) is a thin-film photovoltaic device. It differs from crystalline silicon in that there is no lattice structure. Amorphous silicon absorbs light above approximately 1.75 eV. When germanium or tin is added to the cell, light as low as 1.5 eV is usable. When a-Si is bonded with hydrogen or fluorine for improved electrical properties, it is 2 orders of magnitude more light-absorbing than crystalline silicon. The a-Si cells can be 0.5 micrometers thick with stable electrical properties.

A module can be produced by depositing a layer of transparent conductive metallic oxide on glass, etching grooves in the oxide, depositing and patterning the a-Si layers, and then depositing a back contact made of metal or conductive oxide. The back contact of one cell can be made to touch the front contact of another cell, causing current to flow between them.

An a-Si cell produced by ARCO Solar has an area of 3.9 cm^2 (0.6 in^2). It has been tested at an efficiency of 10.8 percent and a power density of 108 W/m^2 (0.01 hp/ft^2). This cell is 4.0 micrometers ($1.6 \times 10^{-4} \text{ in}$) thick and has an area density of 21.6 g/m^2 ($4.4 \times 10^{-3} \text{ lb/ft}^2$). Amorphous silicon will degrade with exposure to sunlight, dependent on the intensity of sunlight, the operating temperature, the electrical load, and the device configuration. A worst case situation will result in an immediate 20-to 25-percent drop in power output. This would be an undesirable trait for solar cells in this particular application.

4. Cadmium Telluride

Cadmium telluride (Cd-Te) is a polycrystalline material used to make thin-film solar cells by several low-cost methods. One fabrication method is called close-spaced sublimation. The greatest disadvantage of Cd-Te is the difficulty in electrically contacting the semiconductor material. Another hindrance is an associated instability in cell performance. The material is resistive rather than highly conductive. Cd-Te is not hindered by degradation when exposed to light, similar to a-Si.

5. Copper Indium Diselenide

Copper indium diselenide (CIS) is another thin-film photovoltaic device. CIS absorbs light above 1.0 eV. If gallium or sulfur is combined with CIS to form an alloy, the bandgap is raised and the voltage output enhanced. Copper indium diselenide does not degrade with sunlight exposure to the same degree as other commonly used semiconductors. A CIS cell has been exposed to sunlight for 9,000 h without degradation of performance.

A 3.5-cm² (0.5-in²) CIS cell has been shown to have a 14.4-percent efficiency with a power density of 141 W/m² (13.1 W/ft²), while a CIS module of 938 cm² (369.3 in²) has an efficiency and a power density of 11.2 percent and 112 W/m² (10.4 W/ft²), respectively. These cells are 5.75 micrometers (2.26×10⁻⁴ in) thick and have an area density of 36 g/m².

6. Concentrator Solar Cells

Single-crystal and thin-film cells can be used in different configurations to attain higher efficiencies. The concentrator cell is a single crystal cell with a unique configuration. Concentrator cells require reflectors or lenses mounted on top of the cell to concentrate the sunlight producing a higher efficiency than can be attained under normal sunlight. The reflectors add considerable weight to the cell assembly in addition to increased inflexibility. Under conditions where this is not a problem, the use of low-cost lenses reduces the need for relatively expensive solar cells. Provided the cells are kept reasonably cool, these lenses could increase efficiency by 5 percent. However, there are several disadvantages to concentrator cells, such as the absorption or reflection of 5 to 10 percent of the incident light by the focusing lens. Concentrators cannot focus diffuse sunlight. This light makes up about 20 percent of the available solar energy. The most common concentrator cells are made from single-crystal silicon or gallium arsenide cells. These devices have efficiencies in the range of 20 to 26 percent, however, the increased weight makes them impractical for some applications.

7. Tandem Solar Cells

Another photovoltaic device is the tandem cell, which is merely two cells stacked one on top of the other. The advantage here is in the two different bandgaps of two semiconductors. The lower cell will absorb some of the light that passes through the upper cell. As an example, CIS is placed underneath Ga-As. The tandem cell would have an AM0 efficiency of 23 percent, but twice the weight of the single Ga-As cell. The tandem cell represents a 2- to 3-percent increase in efficiency. Where weight is not a major consideration, a tandem cell would be an excellent choice.

8. Comparisons Between Cells

Some significant lessons were learned with the construction and flight of the *Gossamer Penguin*. Although the *Gossamer Penguin* was designed to fly close to the ground and is potentially

much smaller than a HASPP, these lessons may be applied to the design of a HASPP. Two lessons to be discussed here relate directly to the selection of the solar cells to be used in the design. Single-crystal solar cells were used on the *Gossamer Penguin*. In this application the cells experienced buckling and breakage during flight due to heating over a high range of ambient temperatures as well as the bending and twisting of the wings. Single-crystal cells are very fragile, even a slight deflection of the wings where the cells are mounted can cause the cells to break. Since a HASPP must have a very long wingspan and low wing loading, bending and twisting of the wings is expected.

The second lesson relates to the removal of the solar cells during maintenance. The cells, attached to the wings with an acrylic-based adhesive transfer tape, may be released by heating them with a heat gun. This proved to be a difficult process which frequently led to breaking the fragile single-crystal cells. Thin-film photovoltaic devices are much less fragile and more flexible than the single-crystal cells. The thin-film cells can have a radius of curvature up to 0.79 cm (2 in). Although the polycrystalline devices have lower efficiencies than single crystals, their use will reduce the difficulties associated with breakage caused by wing flexure.

Another advantage associated with the use of thin-film cells is related to their area density. Thin-film cells would result in a lower structural weight over crystalline cells. The single-crystal cells must be mounted to a firm, inflexible surface to minimize breakage. Past solutions to this problem have been to install stiff foam between the ribs in the wings, then apply the cells to a Mylar film covering the wings. Thin-film cells would not need the foam, thus further reducing the weight of the aircraft.

Finally, another advantage of the thin films over single crystals is related to the airfoil shape. Use of single-crystal cells causes the airfoil shape to be comprised of many flat surfaces. A disjoint or rough surface will produce less lift and more drag than a continuous or smooth surface of the same geometry. By their very nature, an array of thin film cells can be attached to the prescribed airfoil shape without producing any discontinuities or shape variations.

The Ga-As solar cell was chosen for use on the HASPP. The combination of flexibility due to thickness and the high efficiency of this cell make this the best choice for a HASPP application. Although the Ga-As cells are more expensive (on the order of \$250 per 2- by 4-in cell or about \$200 per watt) and weigh more than some of the other alternatives, a high efficiency is the most important characteristic in the choice of solar cells for a HASPP. The Ga-As efficiency coupled with the ability of the solar cells to conform to the airfoil shape make this the obvious choice.

Chapter VI. CONSTRUCTION

In years past, HASPP's have been declared to be infeasible. The principle reasons for these declarations have been the inability to create sufficient power with solar cells, the high weights of the energy storage and generation systems, and the associated high weight of the airframe structure. A lightweight structural material, with sufficient strength to carry flight loads was deemed necessary before solar-powered flight could be possible. *Solar Challenger* represents such a breakthrough in aircraft construction, using composite materials to minimize weight. The Boeing *Condor* also uses graphite/Kevlar, epoxy sandwich, and Nomex honeycomb construction.

Wing loadings of the successful solar-powered airplanes: *Project Sunrise*, *Gossamer Penguin*, and *Solar Challenger* are 1.22 kg/m² (0.25 lb/ft²), 2.34 to 2.58 kg/m² (0.48 to 0.53 lb/ft²), and 5.32 to 6.32 kg/m² (1.09 to 1.30 lb/ft²), respectively. These low wing loadings are made possible by using such advanced materials as Nomex honeycomb and Kevlar 49 fabric.

The structural design of the HASPP presented here is patterned after *Solar Challenger*. *Solar Challenger* used filamentary composites where strength was required and easily formable plastics where strength was not a consideration. The principal structural material is a graphite fiber/epoxy composite. This material has a high strength-to-weight ratio and a high stiffness-to-weight ratio. Kevlar aramid fiber strands, braid, and cloth were used in tension elements and as tube reinforcement. Kevlar also has high strength-to-weight and stiffness-to-weight ratios, though not as high as graphite epoxy, however, Kevlar is much tougher and more damage resistant than graphite. Kevlar fabric will retain its tensile strength even after failure of the laminate. This decreases the likelihood of catastrophic failures. Nomex honeycomb was used as a core in sandwich construction since it offers the least weight for the necessary shear and compressive strength and stiffness. Polystyrene foam plastic was used as the shear web in low stress areas. It was also used as an aerodynamic filler because of its low density, strength, and ease of fabrication. A 12.7-micrometer (5.0×10^{-4} -in) thick Mylar plastic film was used as an outer covering because it is lightweight, strong, damage-resistant, and has directionally dependent heat-shrink characteristics.⁸ The *Condor* also uses graphite/Kevlar and epoxy sandwich and Nomex honeycomb construction.

Mylar, made by DuPont, ranges in thickness from 92 gauge to 700 gauge (0.92 mil to 7 mil). Transparent Mylar is not resistant to ultraviolet light so it will take on a yellow cast with exposure to sunlight. Transparent Mylar or type D has been tested for three ranges of light. All three ranges, ultraviolet at 0.3 micrometers, visible at 0.6 micrometers, and infrared at 0.8 to 2.4 micrometers, pass through the Mylar at 86 to 87 percent. The light tests hold true for all thicknesses of Mylar. The yellow cast of the transparent Mylar would also inhibit sunlight from reaching the cells. For this reason, the solar cells must be mounted on top of the wing instead of inside the wing. Mylar that is heat-shrinkable has a 9-percent haze and only comes in 12.7-micrometers (0.5-mil) and 38.1-micrometers (1.5-mil) thicknesses. The density of all types of Mylar is 1.39 g/cm³ (0.05 lb/in³).

A. Detailed Construction of *Solar Challenger*

The lightweight wing spar of *Solar Challenger* was made from unidirectional graphite/epoxy preimpregnated tape, Nomex honeycomb, and Kevlar 49 fabric laid up wet with epoxy resin. The structural tube of the circular cross-section spar is composed of graphite tape wrapped at 45° to carry the torsional and bending shear forces. Multiple layers of graphite caps on the fore, aft, top, and bottom sides of the spars were added to carry the bending, tensile, and compressive loads. Nomex honeycomb, manufactured by Hexcel, with graphite epoxy, and an overwrapping of two layers of Kevlar fabric/epoxy resin stabilized the tube wall. The completed wing spar of *Solar Challenger* weighed 8.2 kg (18.1 lb) for a wing span of 14.3 m (46.9 ft).

The stabilizer spar was a smaller version of the wing spar. Instead of the Nomex honeycomb, polystyrene foam plugs were placed at intervals for stability. Two stabilizer spars were needed. Polystyrene foam sections were placed between the ribs to form the wings leading edges, while the trailing edges were made from fiberglass and foam sandwich. A polystyrene foam sheeting was placed in the upper portion of the wings between the ribs to steady the Mylar film, creating a firm surface for the fragile single crystal silicon solar cells used.⁸

The fuselage composite tubing was made from graphite filaments, Kevlar fabric, and epoxy resin. The Kevlar fabric was used to control damage by containing the graphite splinters to prevent failure. This also augmented the allowable crippling stress of the graphite fiber.⁸

The propeller blades of *Solar Challenger* were made of graphite fabric/epoxy laid up wet over a high density polystyrene foam core. Unidirectional graphite spar caps ran the length of the blades to carry the bending loads and improve the bending stiffness of the propeller.⁸

Control lines run to bell cranks attached to graphite torque tubes were used to operate the control surface. These tubes also served a secondary purpose by acting as spars for the control surfaces. The control lines needed to be flexible, durable, and resistant to ultraviolet degradation, abrasion, and weathering. It was necessary that they have a high stiffness/strength-to-weight ratio. A material made by Synthetic Textiles, Inc., of Ventura, CA, met these requirements. Since braided Kevlar loses much of its modulus due to the geometry of the fiber orientation, unidirectional strands of Kevlar 29 yarn were interlocked and then Dacron cord was used to overbraid the core to protect the Kevlar from snagging or abrading and to protect against ultraviolet degradation.⁸

Although *Solar Challenger* was built with a much different mission in mind than a HASPP, it is reasonable to assume that the same type of construction techniques could be incorporated into a long-duration, high-altitude aircraft. In previous designs of HASPP's, the aircraft has consisted of the airframe, propulsion drive system, solar cells, fuel cells, avionics, and payload subsystems. The solar-powered planes that have flown for relatively short durations are similar to HASPP designs only they are smaller, and the payload might be a pilot rather than sensors and avionics.

Chapter VII. AERODYNAMICS

The HASPP, while unusual with respect to most airplanes, must conform to the same aerodynamic rules as conventional piloted aircraft. The airplane's requirements for equilibrium flight must be analyzed, as well as the climb performance, lift, drag, and pitching moment. These quantities are used in the iterative design procedure in the design methodology.

Several terms must be defined at the outset of the aerodynamic analysis. Table 5 lists the symbols used in the aerodynamic analysis. Figure 6 illustrates the forces and moments on an airplane in a steady climb. The force resultants in the figure are shown acting through the center of mass. In figure 6, the velocity vector is represented by V . The velocity vector of the airplane's center of mass is at an angle θ_c from the horizontal, representing the angle of climb. The angle between the line of thrust and the horizontal is denoted as θ . The thrust line is taken as a reference line for the airplane. The angle of attack of the airplane is represented by $(\theta - \theta_c)$ or α , the angle between the reference line and the velocity vector if the wing has no angle of incidence relative to the aircraft.

The weight of the aircraft, W , is in the direction of gravity and the lift, L , is created by the wing and is in opposition to the weight. The wing produces drag in addition to lift. In the case of a large horizontal tail surface, it too would produce lift and drag. The fuselage also creates a drag called parasite drag. The combination of these is the total drag, D_{tot} , and acts in the direction opposite to the direction of flight. In steady flight, climbing, level, or diving, the component of thrust, T' , balances the component of lift, drag, and weight along the velocity vector. Further, the component of lift must balance the component of drag, thrust, and weight perpendicular to the velocity vector. Finally, for

Table 5. Symbols used in aerodynamic analysis.

M	pitching moment
V	velocity
L	lift
D_{tot}	total drag
θ	angle between line of thrust and horizontal
θ_c	angle of climb
$(\theta - \theta_c); \alpha$	angle of attack
a'	angle of incidence
δ	ratio of static pressure at altitude to pressure at SL
T	absolute temperature ratio
σ	ratio of density at altitude to density at SL
T'	thrust
W	gross weight
S	distance propeller travels
t	time
P	power
V_c	vertical rate of climb = $V\theta_c$
p	pressure
ρ	mass density
R	gas constant
T	temperature
h	altitude (agl)
dp	differential pressure
dh	differential altitude
dT	differential temperature
g	gravitational force
l	characteristic length of body in fluid
S'	area
$V^2/2$	dynamic pressure
ν	kinematic viscosity
M'	Mach number
μ	coefficient of viscosity
a	velocity of sound
C_L	coefficient of lift
C_D	coefficient of drag
C_{Dp}	coefficient of parasite drag
C_{Di}	coefficient of induced drag
C_f	coefficient of friction
S_p	equivalent parasite drag area
e	airplane efficiency factor
AR	aspect ratio
k	lift factor
b	wing span
S_w	wing area
para	parasite
i	induced

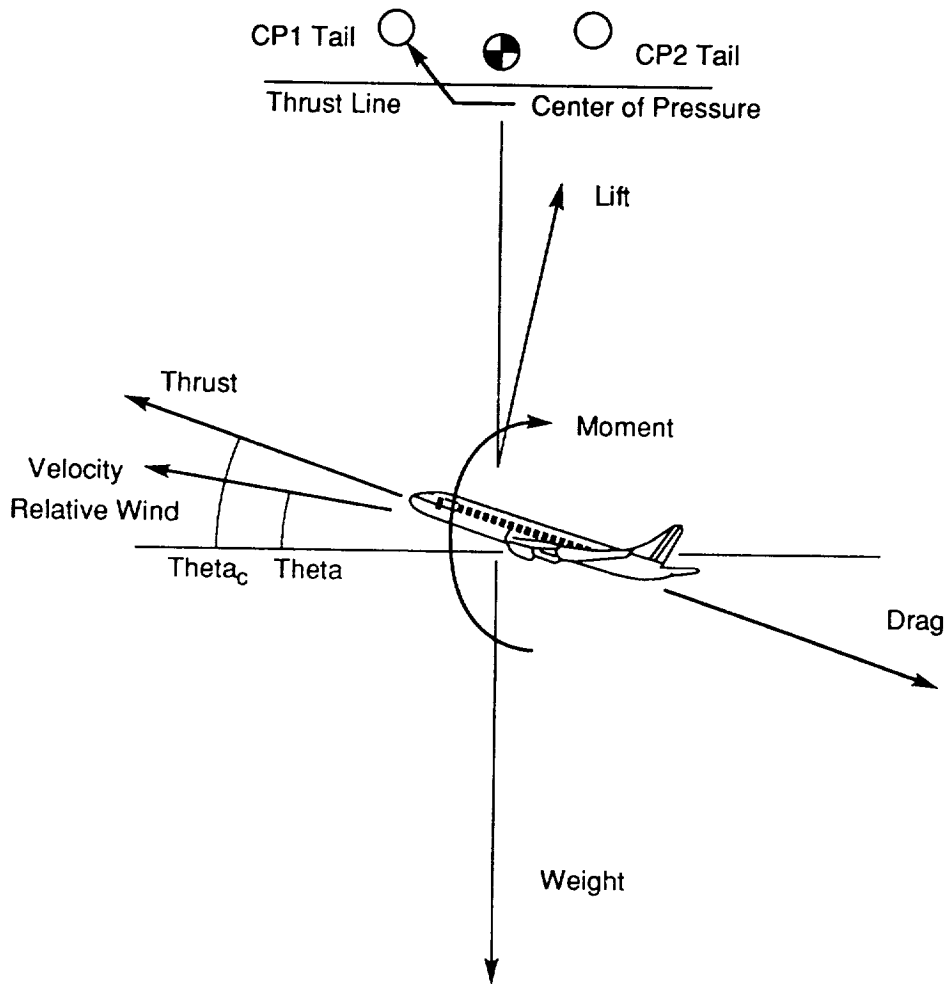


Figure 6. Forces and moments on an airplane in a steady climb.

steady flight the pitching moment, M , must be zero. This moment arises due to the fact that the aerodynamic forces act at the center of pressure of the wing and tail surfaces and the thrust vector does not necessarily pass through the center of mass. The moment is dependent on the angle of attack at a given airspeed. In order for the airplane to exhibit the most stable response, an increment in M , caused by a change in the angle of attack, should be negative. Otherwise, an unstable situation is created where the airplane tends to move even farther from a steady-state condition when disturbed.

A. Equilibrium Flight and Airspeed

The vector sum of all the forces represented in figure 6 must equal zero for the airplane to be in equilibrium. Therefore, the sum of forces in the direction of flight is:

$$T' \cos (\theta - \theta_c) - D_{\text{tot}} - W \sin (\theta_c) = 0 \quad , \quad (46a)$$

or for level flight:

$$W = L \quad \text{and} \quad D_{\text{tot}} = T' \quad . \quad (46b)$$

The vector sum normal to the direction of flight is

$$W \cos (\theta_c) - L - T' \sin (\theta - \theta_c) = 0 \quad . \quad (47)$$

Equations (46a) and (47) can be solved for the angle of climb by:

$$\theta_c = \text{Tan}^{-1} \{ [T' \cos (\theta - \theta_c) - D_{\text{tot}}] / [L + T' \sin (\theta - \theta_c)] \} \quad . \quad (48)$$

The assumptions are made that θ_c and $(\theta - \theta_c)$ are small angles, and that the thrust for the airplane will be only a fraction of the weight. Equation (48) now becomes:

$$\theta_c \cong (T' - D_{\text{tot}}) / W \quad . \quad (49)$$

For airplanes propelled by turbojets or rockets, equation (49) is useful in its present form. However, the equation must be modified to deal with propeller-driven airplanes as is the case for a HASPP. The work the propeller is capable of performing will determine the angle of climb and, in turn, the rate of climb.

In order to calculate the work the propeller performs, S is defined as the distance the propeller travels in time t at a constant velocity V . The resultant propeller work is:

$$\text{Work} = T' S \quad . \quad (50)$$

Power is the rate work is performed, hence:

$$\text{Power}_{\text{propeller}} = T'(S/t) \quad . \quad (51)$$

Since (S/t) is equal to velocity, the available power from the propeller is:

$$P_{\text{avail}} = T' V \quad . \quad (52)$$

By comparison, the power required by a body traveling through the air at a velocity V with a drag D is:

$$P_{\text{req'd}} = D_{\text{tot}} V \quad . \quad (53)$$

Combining equations (49), (52), and (53) results in,

$$P_{\text{avail}} - P_{\text{re}} = W(V\theta_c) \quad . \quad (54)$$

The vertical rate of climb is given by $(V\theta_c)$ or $V \sin \theta_c = dh/dt$ and is referred to as V_c .

It can be seen by equation (54) that the vertical rate of climb is obtained by equating the power required to lift the weight of the airplane at a speed V_c to the excess power. To achieve the maximum airspeed in straight and level flight, the maximum available power must equal the power required or:

$$\text{Airspeed}_{\max}: P_{\text{avail}} = P_{\text{req'd}} \quad (55)$$

B. Fluid Statics

An airplane's performance is related to the height at which it is flown in the standard atmosphere corresponding to the pressure or density; in other words, the pressure altitude or density altitude. The altimeter in an airplane is an absolute pressure gauge calibrated according to the standard atmosphere. Table 6 lists standard sea level values for the atmosphere. Table 7 gives values of the standard atmosphere at 20 km (65,600 ft).

Table 6. Standard sea level values of atmosphere.

Mass density, ρ	0.002378 slugs/ft ³	1.223 kg/m ³
Pressure, p_o	2,116.2 lb/ft ²	101.33 kN/m ²
Temperature, T_o	518.69 °R	288.16 K
Kinematic viscosity, ν_o	1.5723×10^{-4} ft ² /s	1.446×10^{-5} m ² /s
Speed of sound at sea level, a_o	1,120 ft/s	341.4 m/s

Table 7. Standard atmosphere values

Altitude	65,600 ft	20 km
Temperature	389.99 °R	216.66 K
Pressure	118.92 lb/ft ²	580.58 kg/m ²
Mass density	5.72×10^{-3} lb/ft ³	0.092 kg/m ³
Density at 60,000 ft and Latitude 40	2.25×10^{-4} slugs/ft ³	116 g/m ³
Density at 70,000 ft and Latitude 40	1.36×10^{-4} slugs/ft ³	70 g/m ³
Speed of Sound	968.08 ft/s	295.07 m/s
Kinematic Viscosity	1.67×10^{-3} ft ² /s	0.155×10^{-3} m ² /s

Note: The temperatures at 60,000 ft and 30° N. vary approximately 1 °C from January to July, and the temperatures at 70,000 ft and 30 ° N. vary approximately 4 °C from January to July.

A review of the relevant fluid statics relating these atmospheric values is important to an aerodynamic analysis. Pressure, density, and temperature are examined in order to evaluate the environment in which a HASPP will operate. The performance of a HASPP and its payload are dependent on these conditions. The equation of state relates the pressure, density, and temperature of a fluid by:

$$p = \rho RT \quad (56)$$

where T is the temperature in degrees K and R is the gas constant given by 287.3 m²/Ks² (1,545 ft-lbf/lbmol°R) for air at normal temperatures. The variation of static pressure through the atmosphere must be considered in order to evaluate the operating environment of the HASPP. To do this, a differential mass of the atmosphere is examined. Summary forces on a differential mass of gas results in:

$$dp/dh = -\rho g , \quad (57)$$

(ignoring other factors such as thermal distribution, etc.) where h is the altitude above ground and ρ is not a constant. The negative sign appears since the gravitational attraction is opposite to the direction of increasing altitude. Solving equation (56) for ρ and substituting into equation (57) yields:

$$dp/p = - (g dh)/RT . \quad (58)$$

The temperature in equation (58) varies with altitude as shown in figure 7. Up to 11 km (36,097 ft), the temperature decreases linearly with altitude at a lapse rate of 6.51 K/km, causing equation (58) to become:

$$dp/p = - (dT/T) \{1/[R(dT/dh)]\} . \quad (59)$$

The ratio of static pressure at altitude to pressure at sea level is denoted by δ where:

$$\delta = T^{5.2561} , \quad (60)$$

and T is the absolute temperature ratio. Equations (56), (59), and (60) are combined to give:

$$\sigma = \delta T , \quad \sigma = T^{4.2561} , \quad (61)$$

where σ is the ratio of the density at altitude to the density at sea level. Using the standard lapse rate and a sea level temperature of 288.15 K (518.69 °R) T becomes

$$T = 1 - 0.02256 h , \quad (62)$$

where T is a function of altitude and h is the altitude in kilometers. Equations (59) to (62) hold true for the region of the atmosphere known as the troposphere, from the surface to approximately 8 km (2,423 ft).

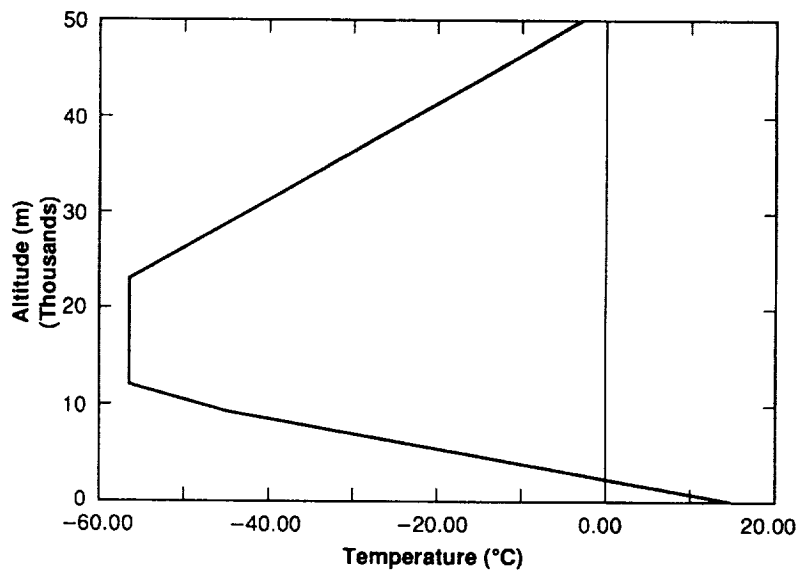


Figure 7. Standard atmosphere.

At altitudes between 11 km (36,097 ft) and 23 km (75,475 ft), the temperature is approximately a constant. This region of the atmosphere is known as the lower part of the stratosphere. Through the remainder of the stratosphere up to about 50 km (164,076 ft), the temperature increases to approximately 270 K (486.27 °R).

C. Fluid Dynamics

A review of the relevant dynamics must now be considered for a thorough aerodynamic analysis. If the static pressure distribution normal to the surface of a body moving in a fluid is known, then the forces on the body can be determined by integrating this pressure over the surface. These quantities are assumed to be related in the following manner:

$$F \sim \rho^a V^b I^c \quad (63)$$

This equation becomes:

$$F \sim \rho V^2 I^2 \quad (64)$$

and:

$$\text{Lift} = L = (1/2) \rho V^2 S' C_L \quad (65a)$$

$$\text{Drag} = D = (1/2) \rho V^2 S' C_D \quad (65b)$$

$$\text{Moment} = M = (1/2) \rho V^2 S C_m \quad (65c)$$

where I^2 is replaced by a reference area, S' . The quantity $(\rho V^2/2)$ in equations (65) is defined as the dynamic pressure.

Some other quantities that need to be defined are the Reynolds number, Re , the kinematic viscosity, ν , and the Mach number, M' . Equations (66) define these quantities:

$$Re = Vl\rho/\mu = Vl/\nu \quad (66a)$$

$$\nu = \mu/\rho \quad (66b)$$

$$M' = V/a \quad (66c)$$

where μ is the coefficient of viscosity and a is the velocity of sound. The Mach number determines to what extent fluid compressibility can be neglected. It is interesting to note that the parasite drag coefficient is slightly decreasing with Reynolds number. Typically it has been seen that C_{Dp} decreases proportional to $(Re)^{-n}$ with $n = 0.1$ to 0.15 such that C_{Dp} will decrease 20 to 30 percent with an order of magnitude decrease in Reynolds number.³⁸

D. Lift and Drag

The equations for lift and drag of an airplane are shown in equations (65), with C_L and C_D as functions of α , the angle of attack. As stated earlier, the total drag on the plane is given as the sum of the parasite drag and the induced drag:

$$D_{\text{tot}} = D_i + D_{\text{para}} \quad (67)$$

The parasite drag, or a combination of profile drag and skin friction, is:

$$D_{\text{para}} = C_{\text{para}} \rho / 2 V^2 S' \quad (68)$$

or:

$$D_{\text{para}} = \rho / 2 V^2 S'_{\text{para}} \quad (69)$$

Where $S'_{\text{para}} = C_{\text{para}} S'$. S'_{para} is the parasite area of the airplane and refers to the complete airplane except the wing, while S' is the frontal area of the body. The induced drag is:

$$D_i = \rho / 2 V^2 C_{Di} S' \quad (70)$$

Therefore, the total drag on a body is:

$$D_{\text{tot}} = \rho / 2 V^2 [S'_w C_D(\alpha) + S'_p] \quad (71)$$

The coefficient of drag from Youngblood's work:⁶

$$C_{D_{\text{tot}}} = (C_{Do})_{\text{wing}} + (C_{Do})_{\text{tail}} + (C_{Do})_{\text{pod}} + (C_{Do})_{\text{boom}} + [(1 + \delta) / (\pi * AR)] C_L^2 \quad (27)$$

is a compilation of coefficients of drag for the various components of the airplane. It can be seen that the coefficient of parasite drag for the pod, equation (25), is similar to that obtained experimentally for an ellipsoid.³⁸ This report will use equations (25) and (26) for parasite drag coefficients of the boom and pod. The wing and tail drag coefficients will be taken from drag polar charts for those airfoils. The drag coefficient from these charts is both the parasite and induced drag for the airfoil. This report will differ from previous designs⁶ in that the tail will be considered as a lifting device as well as the wing.

Experimental results show that the value of C_p for a rectangular plate with sides a (longer side) and b in length varied from about 1.2 at $b/a = 1.0$ to 2.0 at $b/a = 0$. The latter point would represent a very slender rectangle. The associated Reynolds number for the experiment was about 50,000 to 150,000. Similarly, circular disks at right angles to the stream were found to have an average C_{para} of 1.11. A closed hemisphere with the plane side opposed to the stream has a coefficient of parasite drag similar to that of a circular disk, $C_{\text{para}} = 1.2$. A circular cylinder with the stream parallel to its axis has a drag coefficient that is dependent on the ratio of length to diameter, l/d . The condition of $l/d = 0$ is the circular disk and as l/d increased, C_{para} decreases to 0.82 at $l/d = 2.5$ and then C_{para} increases. For l/d from 5 to 30, $C_{\text{para}} = 0.8$ to 1.2 for Reynolds numbers below 500,000. Round bodies (cylinders, spheres, ellipsoids, etc.) have two regions of Reynolds numbers with almost constant values of C_{para} . There is a region of transition separating moderate Reynolds and high Reynolds numbers. Spheres, with the reference length the diameter, have a $C_{\text{para}} = \sim 0.5$ for Reynolds numbers 20,000 to 200,000 and $C_{\text{para}} = 0.2$ at Reynolds numbers above 300,000. An ellipsoid with a diameter ratio of 1:1.8 (minor diameter vertical) at Reynolds numbers from 200,000 to 600,000 has values of C_{para} from ~ 0.05 to 0.1.

E. Airfoils

A HASPP will operate at an altitude of low density, and it will fly at speeds considered to be slow (on the order of 90 ft/s), relative to conventional airplanes. Therefore, the HASPP will operate in a low Reynolds number regime. Based on Youngblood's 1982 design, the HASPP will operate at a Reynolds number of approximately 3,000,000 at 20 km (65,600 ft). The HASPP presented in this paper operates at a Reynolds number of 350,000.

Most airfoils are designed for conventional aircraft operating at higher speeds and hence for optimal performance at higher Reynolds number range. Therefore, care must be exercised to choose an airfoil designed specifically for high performance, slow flight, and low Reynolds numbers. It is necessary that the airfoil used on the wings, tail, and propeller of the HASPP generate the maximum lift and minimum drag capable of an airfoil. The maximum lift is primarily a function of the interaction of the upper surface pressure distribution and at low Reynolds numbers, the boundary layer. The NACA four- and five-digit airfoils were designed without consideration of the influence of the boundary layer. The boundary layer effects were taken into consideration in design of the NACA six-digit airfoil series. In this series, the boundary layer was considered to the extent that a boundary layer was desired to exist over a certain laminar portion of the leading portion of the airfoil for a specified range of lift coefficients.

The Lissaman 7769 airfoil was used on the *Gossamer Condor* and *Gossamer Albatross*. The airfoil performed well in these applications, however, in wind tunnel tests performed after these flights a significant degradation in performance for chord Reynolds numbers below 150,000 was indicated.⁶⁰ The airfoils used on *Solar Challenger* were the Lissaman-Hibbs 8025 and 8230 for the wing and stabilizer respectively. The 8025 has an exactly linear last 85 percent of the upper surface, while the 8230 also has a flat upper surface with some laminar flow on the lower surface. The Boeing *Condor* uses a Liebeck airfoil with a high aft camber resulting in laminar flow over 50 percent of the upper and lower surfaces. The airfoil has a lift-to-drag ratio of 40, similar to some high performance sailplanes, and it continuously operates at lift coefficients up to 1.35. The airfoil is designed to operate to these specifications at Reynolds numbers near 1 million. The propeller for the *Condor* was also designed with a high aspect ratio.

Wortmann has designed a series of airfoils capable of performing in a low Reynolds number range. An upper bound on the low Reynolds number regime is assumed to be 4×10^6 .⁴⁰ Wortmann designed airfoils with the boundary layer consideration extended to the turbulent flow regime. Wortmann has shown that considerable reductions in the drag coefficients can be obtained by the use of concave pressure distributions for the pressure recovery region. Wortmann's airfoils; FX-74-CL6-140, FX-74-CL5-140, FX-72-MS-150A, and FX-72-MS-150B; all show the unusual behavior of increasing maximum lift with decreasing Reynolds number. These airfoils have a more or less flat forepart followed by an increased camber creating an abrupt pressure rise.³² The first two of these airfoils are shown in figure 8. Wortmann believes that it is possible to obtain lift coefficients between 2.0 and 2.4 even at low Reynolds numbers of about 1 million. Figures 9 and 10 show the drag polar for the FX 72-MS-150B, FX-74-CL5-140, and FX 74-CL6-140 airfoils. The low-drag airfoils of Wortmann's design are notably well suited to sailplane applications. The success of Wortmann's work is revealed by a study of modern high performance sailplanes. Most of these sailplanes employ a Wortmann airfoil.³⁹ The Wortmann FX 63-137 airfoil was proposed for use by Youngblood in his 1982 and 1984 papers on solar HAPP's and is illustrated in figure 11. It was chosen for the expected Reynolds number range of 10^5 to 10^6 . Figure 12 shows the drag polar of the FX 63-137 airfoil.

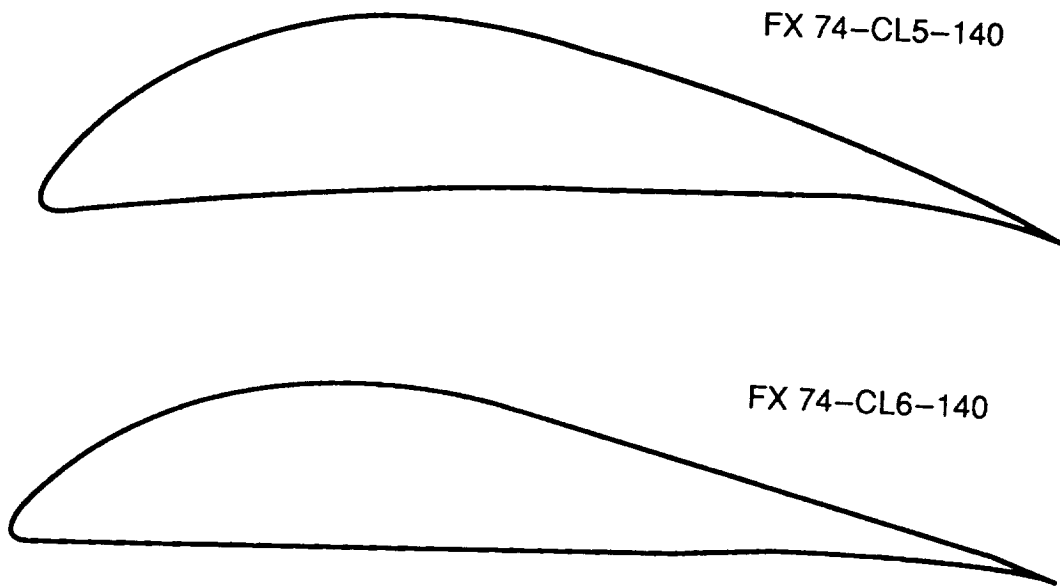


Figure 8. Wortmann FX 74-CL5-140; FX 74-CL6-140.

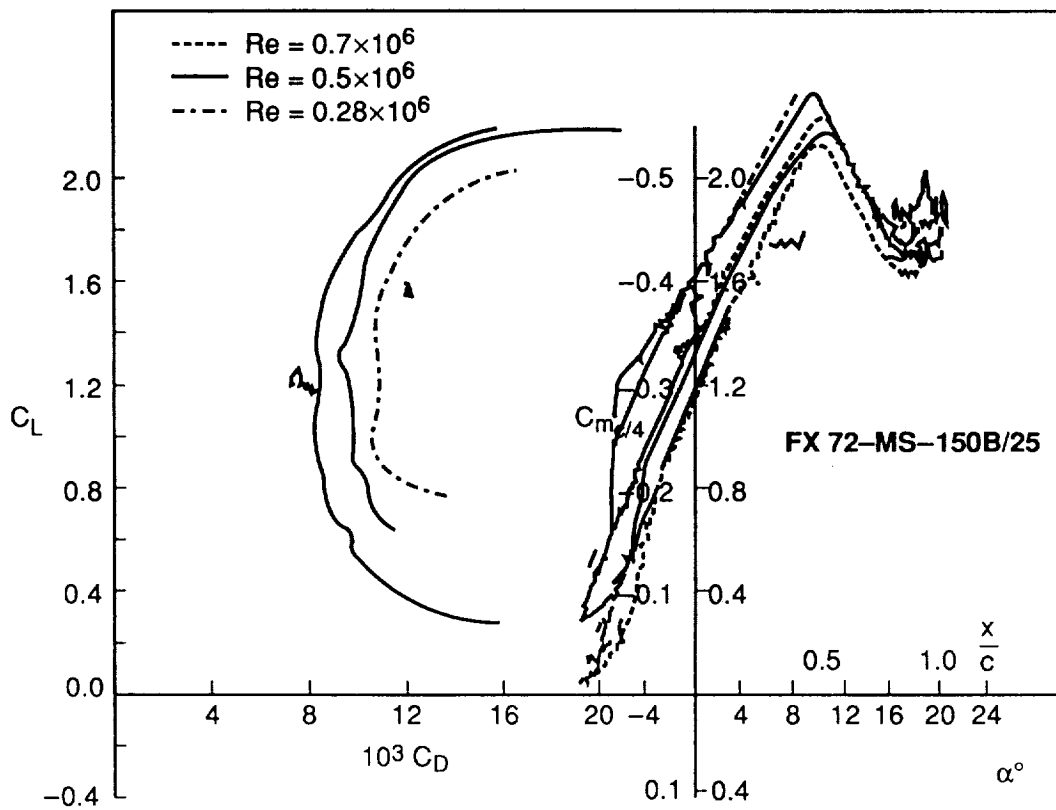
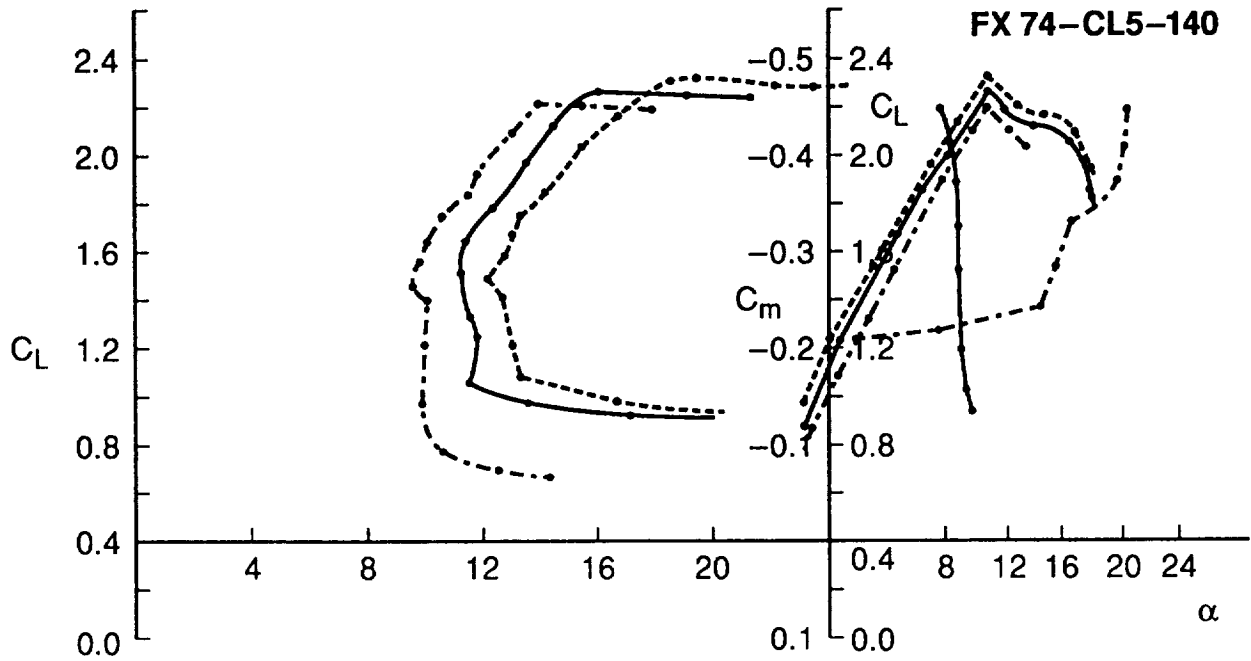
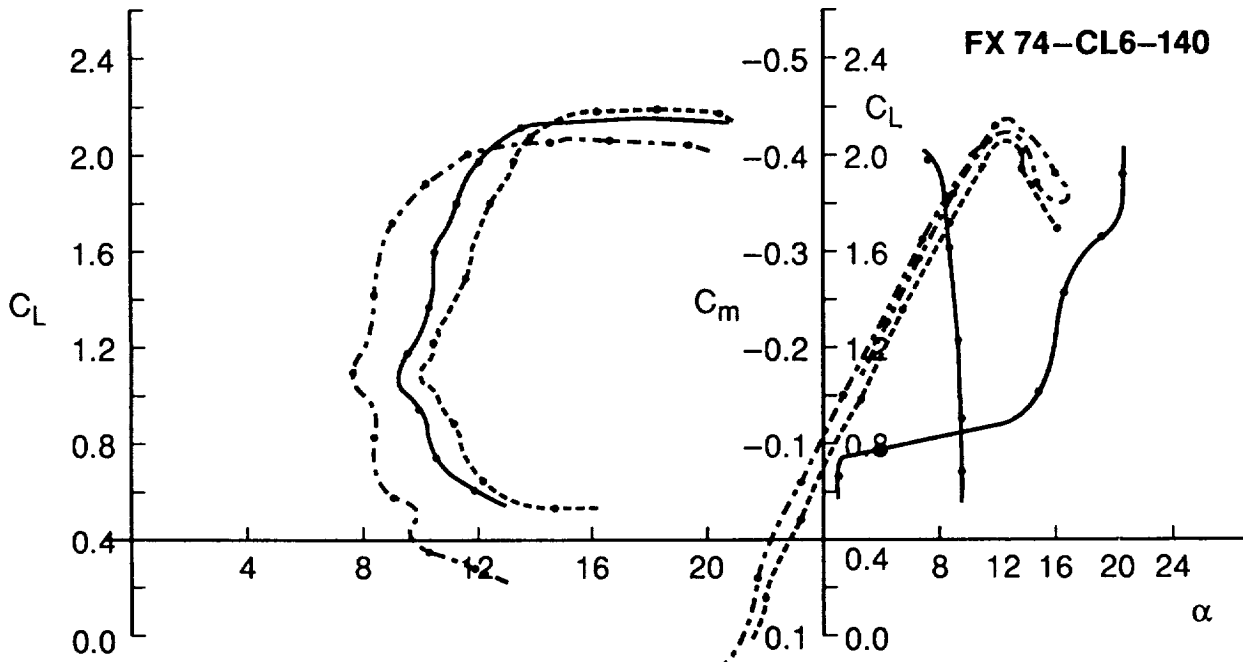


Figure 9. Drag polar, $C_L(\alpha)$ of the FX 74-MS-150B at Reynolds numbers of 1.5 and 3.0×10^6 .



Drag polar, $C_L(\alpha)$, and transition position of the FX 74-CL5-140 at Reynolds numbers of $1.0, 1.5$ and 3.0×10^5 .



Drag polar, $C_L(\alpha)$ and transition position of the FX 74-CL5-140 at Reynolds numbers of $1.0, 1.5$ and 3.0×10^6 .

Figure 10. Wortmann FX 74-CL5-140, FX CL6-140.

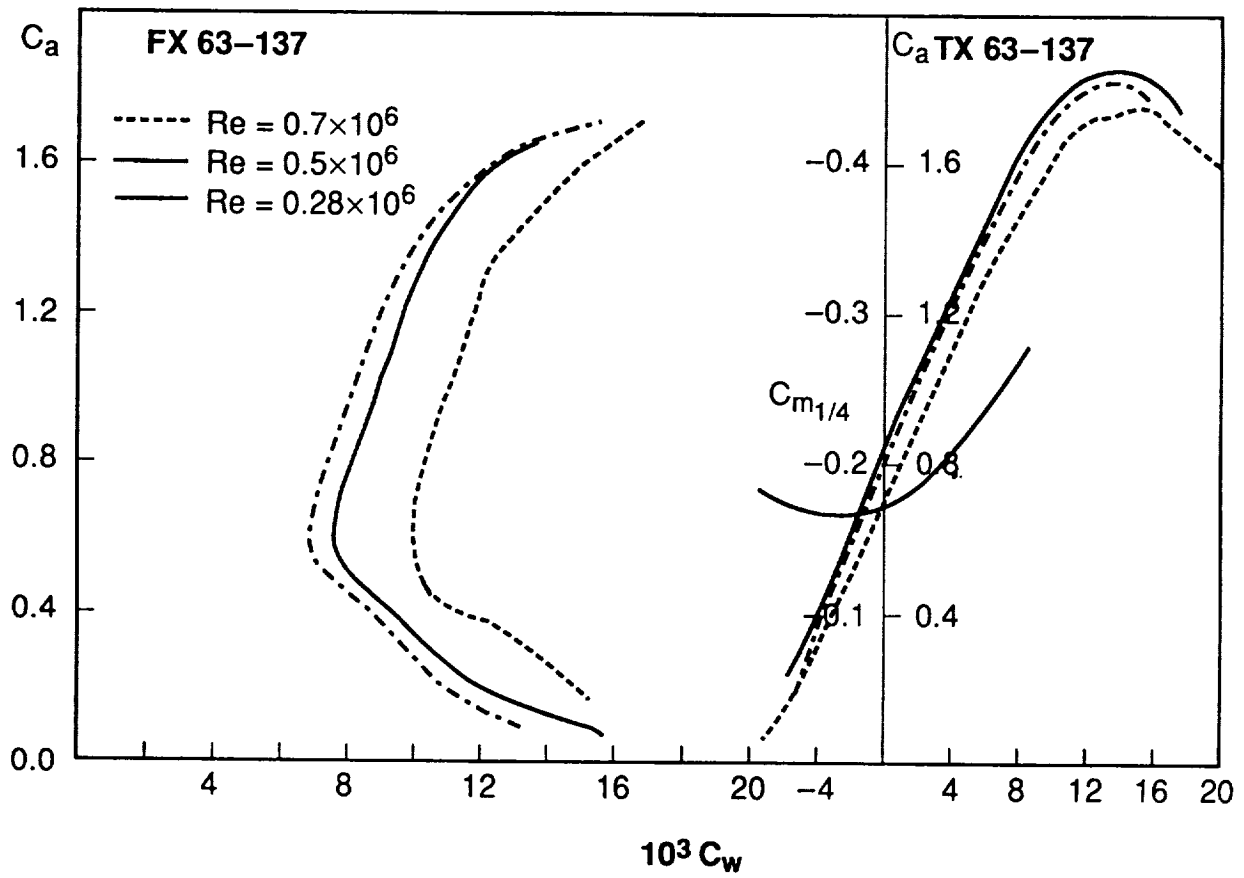


Figure 11. Wortmann FX 63-137.

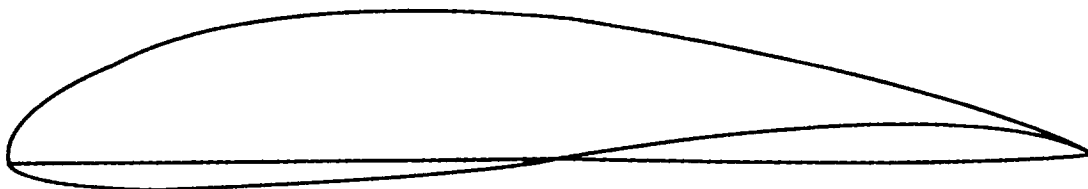


Figure 12. Wortmann FX 63-137.

Chapter VIII. ENERGY STORAGE

Excess energy produced by the solar cells during peak hours of sunlight must be stored for use at night as discussed previously. For HASPP's this energy is typically stored in either a potential or chemical form. The flight profile using potential energy storage would consist of climbing during the day and gliding at night. This method would fall short during the winter months when there would not be enough daylight to enable the HASPP to climb back to its operating altitude. Chemical storage is a better method of retaining excess energy, providing a more stable and reliable flight profile. There are several rechargeable fuel cells available. However, energy storage continues to be a major drawback to the feasibility of HASPP's due to their relatively great weight.

A study of fuel cells requires an understanding of some specific terminology. Table 8 comprises some of the terms and definitions common to all fuel cells.

Table 8. Fuel cell terminology.⁴⁴

- (1) A *cell* is the electrochemical unit used to store energy.
- (2) A *battery* is defined as two or more electrochemical cells electrically connected in a series/parallel arrangement to yield the necessary operating voltage and current levels.
- (3) The *capacity* of a battery is the total number of ampere-hours (Ah) that can be withdrawn from a fully charged cell or battery.
- (4) The *charge rate* is the current that is applied to a cell or battery to restore its available capacity. Usually it is normalized with respect to the rated capacity resulting in units of amperes rather than hours.
- (5) *Depth of Discharge* (DOD) is defined as the percentage of Ah's withdrawn or discharged from a fully charged battery or cell.
- (6) A *cycle* is defined as one discharge-charge series to a specific depth of discharge.
- (7) A battery has a *cycle life*, after which it fails to perform as originally specified. A cycle life is the number of cycles taken to a certain DOD.
- (8) When a battery has 50 percent or more of its capacity withdrawn, the withdrawal is referred to as *deep discharge*.
- (9) The *efficiency* of a battery is the ratio of the useful output to the input. There are Ah, voltage, and energy (watt-hour) efficiencies.
- (10) The *energy density* of a battery or cell is the ratio of rated energy available normalized to its weight or volume.

The DOD is a direct measure of the amount of stored energy that can be discharged from a regenerative battery without decreasing the overall efficiency. A battery's lifetime, given in terms of the number of charge-discharge cycles, tends to be inversely proportional to the DOD.

There are several types of batteries that should be given consideration for the HASPP application, keeping in mind that a high energy density is necessary to accomplish low-wing loading. The leading batteries are lead-acid, silver-zinc, silver-cadmium, nickel-hydrogen, and nickel-cadmium. The last four are listed in order of decreasing energy density. All of the batteries mentioned are capable of being rechargeable, necessary due to the long duration of the flight.

Roy Lanier of MSFC estimates that deep discharge batteries will be necessary for the lightest weight possible.⁴⁹ The depth of discharge will need to be on the order of 75 to 80 percent. Also it is believed that silver-zinc batteries will not last long at high DOD's. This indicates that silver-zinc might not be useful in this application or that larger than normal silver-zinc batteries would need to be made for HASPP's.⁴⁹

A. Lead-Acid Batteries

Lead-acid storage batteries have been in use for over 100 years and much research has gone into their development. This is a lead/sulfuric acid/lead dioxide system that goes through a reaction characterized by the double-sulfate theory. In general, the performance of lead-acid batteries decreases with decreasing temperature and improves with increasing temperatures.

Outgassing occurs during charging of lead-acid batteries. Both hydrogen and oxygen are emitted, particularly at high levels of charge. Sulfation, defined as the growth of lead-sulfate crystals on the battery plates, is possible when the battery is in operation for several days continuously without obtaining a 100 percent state of charge. The lead-sulfate crystals increase the internal resistance of a cell resulting in lower discharge and higher charge voltages.

Lead-acid photovoltaic batteries have rated capacities ranging from 26 to 3,000 Ah. The capacity can vary during the lifetime of a battery depending on the discharge rate, the cutoff voltage, the operating temperature, the age of the battery, and the sulfation that occurs. Table 9 lists some of the characteristics of photovoltaic lead-acid batteries.

Table 9. Lead-acid battery (1982).

<u>Cell Type</u>	<u>Low Rate</u>	<u>Low Rate</u>	<u>Medium Rate</u>	<u>Medium Rate</u>
Capacity (Ah)	200	3,000	45	935
Rate (h)	500	500	8	8
Dimensions L×W×H (in)	4×7×11	13×14×23	6×3×17	13×7×23
Weight (lb) (kg)	35 (15.89)	315 (143.01)	170 (77.18)	1,020 (463.08)

B. Nickel-Cadmium Batteries

Nickel-cadmium (Ni-Cd) batteries came into use around the year 1900. Rechargeable Ni-Cd batteries have been used for two decades in spacecraft. These batteries have the advantage of a relatively long life, however, their low capacity rating could hinder their use in photovoltaic applications. Nickel-cadmium batteries have high rate capabilities and the ability to withstand an overcharge. They are also more tolerant of low operating temperatures and operation at partial states of charge than lead-acid cells. The rated capacities of Ni-Cd batteries range from 0.1 to about 23 Ah at a 5-h discharge rate. Sealed pocket plate types have about a 70 Ah capacity. The batteries typically provide about 1,000 Wh/ft³ (watt-hours per unit volume).

C. Nickel-Hydrogen Batteries

Nickel-hydrogen (Ni-H₂) batteries have been under development by the U.S. Air Force for 10 years. In 1977 the U.S. Navy launched the Navigation Technology Satellite-2 that employs rechargeable Ni-H₂ batteries. In 1982 Ni-H₂ required 1.5 to 2.0 times the volume of an equivalent Ni-Cd battery. Ford Aerospace Corporation has tested an 81 Ah Ni-H₂ battery. The battery assembly has a mass of 110 kg (242 lb) with each cell limited to 2.15 kg (4.76 lb) in weight and 34.3 cm (13.5 in) in length. The cell diameter is 8.92 cm (3.51 in). The battery has a nominal DOD of 35 percent. The average discharge voltage is 37.5 V minimum, and the battery has a design life of 38,000 cycles.

The space station photovoltaic electric power system will rely on power generated by planar solar arrays with energy storage provided by Ni-H₂ batteries. The proposed system contains 20 batteries of 90 cells packaged as 30-cell assemblies. The basic space station power requirement at load is 75 kW (100 hp), therefore nearly 90 kW (120 hp) of dc power production capability is required of the battery system. This requirement allows for inverter and distribution efficiencies, margins, and fixed loads such as control microprocessors. A total peak power of 130 kW (174 hp) capability is required.

A typical method used for designing battery systems for space applications was provided by Jeff Brewer⁴⁶ of MSFC. This method can be adapted for use in designing the energy storage system in the HASPP. Following is an example of a battery system design to be used as a model for the actual HASPP requirements. The model utilizes current Ni-H₂ technology as applied to the Hubble space telescope (HST).

The system requirements call for a 1-year life in a geosynchronous orbit, a battery load of 8.3 kW during a 13.2-h eclipse, and a 105-Vdc battery system. An operating voltage of 1.3 V/cell is used to provide a conservative estimate of battery requirements. The voltage per cell is dependent on the rate of discharge. For this application close to 1.5 V/cell is possible. This operating voltage is used to determine the number of cells needed to produce 105 V by:

$$(105 \text{ V}) / (1.3 \text{ V/cell}) = 81 \text{ cells.} \quad (72)$$

The 81 cells will be connected in series in three 27-cell batteries. Typically a battery contains 24 to 32 V. The three batteries will make one module. The capacity of each cell is 90 Ah, and, since a module consists of a series of cells, each module is capable of 90 Ah. A DOD of 80 percent per orbit is assumed, yielding 72 Ah from each module. A constant current load of 79 A is obtained by:

$$(8,300 \text{ W}) / (105 \text{ V}) = 79 \text{ A.} \quad (73)$$

The capacity requirement per orbit is calculated from:

$$(79 \text{ A})(13.2 \text{ h}) = 1,043 \text{ Ah.} \quad (74)$$

To determine the modules required to supply this capacity requirement:

$$(1,043 \text{ Ah})/(72 \text{ Ah}) = 15 \text{ modules.} \quad (75)$$

A very conservative design would include two additional modules to protect against failure. Each of the 17 modules will weigh approximately 515 lb for a total system weight of 8,755 lb. Each module is approximately 45 in long, 32 in wide, and 15 in high. This is obviously too much weight for the HASPP to carry.

D. Silver-Zinc Batteries

Silver-zinc (Ag-Zn) batteries are being tested for use in orbiting spacecraft. The Ag-Zn combination is still in the experimental stage and the batteries are primarily nonrechargeable; however, some rechargeable cells are being produced. Ag-Zn batteries have a higher voltage even at lower temperatures and three times the energy density of the nickel couples. Table 10 lists the energy densities of the most efficient rechargeable fuel cells.

The Ag-Zn cells are not capable of deep DOD's for many cycles. For this reason, it is mainly considered a good primary battery and generally not a rechargeable battery. There is a Ag-Zn battery system proposed for use in an 18-month life application. However, it will have only 15 deep discharges of 70 percent. The batteries will be cycled between these deep discharges at just a 1-percent DOD. It is not recommended that a Ag-Zn system be used in this application. It has not been done, but it is assumed possible to design a mixed system where Ag-Zn modules would be used during the summer season, when the DOD would be least.

Table 10. Rechargeable batteries.

<u>System</u>	<u>Discharge Voltage</u>	<u>Cell Energy Density (Wh/lb)</u>	<u>Efficiency</u>	<u>DOD</u>
Ni-Cd	1.21	18-23	0.8	0.60
Ni-Cd		11.0 (storage 1982) 6.6 (usable)		
Ni-H ₂	1.25 at 10 °C	24-26	0.8	0.80
Ni-H ₂		13.0 (storage (1982) 10.4 (usable)		
Ag-Zn	1.50	60		
Ag-Zn	1.44/1.51	77		

E. Fuel Cells

A fuel cell is similar to conventional storage batteries in that it is a simple device that continuously converts energy from chemicals directly into electrical energy. This electrochemical reaction directly produces a flow of electric current upon demand. Fuel cells have higher energy densities and higher efficiencies than batteries. Furthermore fuel cells do not wear out as batteries do. A regenerative fuel cell system weighs 25 to 50 percent less than batteries and a deep discharge apparently has no ill effect on its performance. Realistic operating efficiencies lie between 45 and 85 percent. Tom Maloney of Sverdrup⁴³ indicates that an efficiency of 65 percent is commonly used in current design practice.

A fuel cell was used as the primary source of electrical power on the Gemini and Apollo manned space programs and has been used on the space shuttle orbiter. The fuel cells proposed for use on the future Martian mission are designed for an energy density of 500 Wh/kg (226.9 Wh/lb). The fuel cells will cycle at 14 h of daylight and 14 h of dark. These cells are scheduled to be in use in about 4 to 5 years. The state of the art in fuel cells has an energy density of about 300 Wh/kg (136.2 Wh/lb) for the Martian duty cycle.

Two chemicals are used in a fuel cell; one is a fuel and the other is an oxidant. The electrolyte cell of a fuel cell is supplied continuously with chemicals that are stored outside the cell. A common combination used in fuel cells is hydrogen-oxygen (H₂-O₂). The H₂ and O₂ react electrochemically producing electrical power and water. There are several types of fuel cells available. Instead of using hydrogen as the fuel; propane, butane, carbon monoxide, or zinc could be used. The oxygen could be taken from the atmosphere instead of stored in a tank. There are also a variety of electrodes available. Youngblood's solar HAPP design called for regenerative alkaline fuel cells with a nominal time of discharge of 13.2 h. The H₂-O₂ thermochemical reaction (combustion) is highly exothermic. The combination has a free energy of reaction (more energy produced than taken) of 50,900 Btu/lb of H₂. Catalysts are used to reduce the energy needed to start the reaction. The catalysts are then regenerated back to their original form. A fuel electrode catalyst can be very helpful for operations in low temperatures. The catalyst splits the fuel molecule allowing the smaller particles to travel to the cathode. The combination of H₂ and O₂ can also be thermochemical (releasing heat and explosive work) rather than electrochemical (releasing electrical energy). In an electrochemical reaction, ionization occurs, and an atom or molecule gains or loses electrons.

An example of a typical system is an H₂-O₂ fuel cell using an acid electrolyte. H₂ gas ionizes at the fuel electrode (anode) creating H₂ ions and electrons. These electrons flow away from the anode by means of the external circuit through the electrolyte. O₂ gas reacts with these H₂ ions and electrons from the circuit at the oxidant electrode (cathode). Water is produced by this reaction.

The space shuttle uses H₂-O₂ fuel cells of 0.9 V/cell at 150 A/ft² with 0.7 to 1 ft² of planar area. A 12.5-kW power plant weighs 210 lb without the reactants. It is 35 by 33 by 31 cm (13.8 by 13.0 by 12.2 in) which consists of 2 stacks of 32 cells connected in parallel.

In order to calculate the weight of the reactants, the energy being stored in the fuel cells must be known. That energy would be the propulsion power plus the avionics power in watts. The number of electrons, or moles, of H₂ and O₂ are calculated from:

$$n_{\text{H}_2} = (It)/(2F), \quad (76a)$$

$$n_{O_2} = (It)/(4F), \quad (76b)$$

where I is the current in amps, t is the time of discharge or operation of the fuel cell in seconds, F is Faraday's constant, 96,500 coulombs/eq, and 2 and 4 have units of eq/mole. The current is derived from:

$$I = P/E \text{ (for dc)}, \quad (77)$$

where P is the storage power in watts and E is the chosen system voltage. It will be assumed that an extra 10 percent of each gas will be stored so the tanks will not be completely depleted. Difficulties could arise in exhausting a tank entirely.

From the number of moles, the weight of the stored gases can be calculated from:

$$W_{H_2} = (n_{H_2})(2 \text{ g/mole}), \quad (78a)$$

$$W_{O_2} = (n_{O_2})(32 \text{ g/mole}). \quad (78b)$$

Some things must be known about the storage conditions to continue. The storage temperature, T , will be the temperature at altitude. The storage pressure, p , is assumed to be 2,000 psig.⁴³ A safety factor, SF , on the reactant tanks should be between 1.5 and 4. The yield strength, Str , and the density, ρ , of the Kevlar 49/epoxy tank (with 10 mm of titanium shell) are needed and assumed to be 800,000 psi and 3 to 6 g/cm³, respectively. The perfect gas relationship:

$$pV = nRT, \quad (79)$$

is used to determine the volumes of the stored gases. Assuming a spherical tank the radius is:

$$r_{\text{tank}} = [3/(4\pi)V_{\text{tank}}]^{1/3} . \quad (80)$$

The thickness of the tank wall is:⁴³

$$t_{\text{wall}} = (SF)(p)(r_{\text{tank}})/[2(Str)-0.2(p)(SF)] . \quad (81)$$

The weight of the tank is:

$$W_{\text{tank}} = (\text{Surface Area})(t_{\text{wall}})(\rho_{\text{tank}}) , \quad (82)$$

or:

$$W_{\text{tank}} = (4\pi r_{\text{tank}}^2)(t_{\text{wall}})(\rho_{\text{tank}}) . \quad (83)$$

The weight of the entire fuel cell system consists of the tank weight, stored gas weight, electrolyzer weight, and fuel cell weight.

Fuel cells will be used in this application because of their low weight. Coupled with the reasonable weight of a fuel cell system that is capable of supplying the needs of the HASPP is the reasonable volume of the fuel cell system. The Ag-Zn batteries have higher efficiencies, but lower

energy densities, hence higher weight, and they will not function on this application. Practical rechargeable battery systems would weigh far more than the entire HASPP would weigh with a fuel cell system.

Chapter IX. PROPULSION SYSTEM

The HASPP propulsion system converts power generated by the solar cells into thrust to propel the airplane. Earlier it was stated that the propulsion system includes the motor, controller, inverter, reduction gearing, power conditioning, and propeller. This chapter contains information on the motor and its associated components. The propeller is discussed elsewhere. A dc electric motor is used to match the power output of the solar cells and fuel cells. A motor controller is required to route the power from the solar cells and/or the fuel cells to the propeller. Because of the high rotational speed of the motors, gear reduction to the propeller is necessary.

A. Motor

The performance of an electric motor is typically given in units of horsepower (hp) representing the power or rate at which work is performed. The hp unit is equivalent to:

$$\text{hp} = (T\omega)/6,600, \quad (84)$$

where T is the torque in ft-lb and ω is the number of radians turned per second.

At present, the most efficient method of converting electric energy produced by the solar cells into propulsive work for a HASPP is through an electric motor. Motors using rare-Earth magnets employ electronic, rather than mechanical, commutation. This eliminates the associated electromagnetic interference present in conventional electric motors. In comparison to conventional motors, the rare-Earth magnet motors have better response times, are more efficient, and are characterized by a greater reliability. High shaft speeds provide the optimum operating environment for these motors, with greatest efficiency and least weight under those conditions. Rare-Earth magnet motors appear to be the optimum choice for use in this application.

The successful solar airplanes examined in this research have all used air-cooled high speed permanent magnet dc electric motors. *Project Sunrise* used a 447.6 W (0.6 hp) permanent magnet motor with a specific weight of 2.13×10^{-3} kg/W (3.5 lb/hp). *Gossamer Penguin* used a dc double-brush motor, while *Solar Challenger* used a 3.5 kg (7.71 lb) barium ferrite dc motor. The solar HAPP proposed by Youngblood calls for a samarium cobalt permanent magnet motor.

The samarium cobalt magnet has a higher magnetic density than comparable magnets although it is 10 times more expensive than the others. The samarium cobalt motors are being used on board aircraft in alternators, accelerometers, and electric motors. A samarium cobalt dc motor has also been designed for the electromechanical actuator on the space shuttle orbiter elevon. The motor develops about 12,900 W (17.1 hp) at 9,000 r/min, weighs 7.79 kg (17.16 lb), and has an operating efficiency of about 0.95. Tests have been performed on both samarium cobalt and strontium ferrite motors at speeds up to 26,000 r/min. Both consistently performed at efficiencies greater than 0.93 and produced up to 26 kW (35 hp) of power. During some tests, the rpm was greater than 22,000 for

maximum power. A typical samarium cobalt dc brushless motor has a specific power of 2.2 hp/kg (746 W/lb) with an efficiency of 0.95.

A samarium cobalt motor/controller was developed by Sundstrand Corporation for the Air Force XBQM-106 RPV. This particular motor was capable of generating power output of a maximum of 7,800 W (10.5 hp) and a continuous power output of 3,700 to 4,500 W (5 to 6 hp). It was a variable speed motor with a maximum speed of 6,700 r/min. The input voltage was rated at 105 Vdc at no load and the maximum torque was 124.5 cm·kg (108 in·lb). The packaged motor/controller unit weighed 12.1 kg (26.7 lb). The specifications for this motor were suited to the Air Force RPV mission, which does not necessarily meet the design requirements for the HASPP.

The Air Force RPV motor was a brushless dc design using samarium cobalt permanent magnets in the rotor and three windings in the stator. The magnet polarities were radial and were bonded to the eight flat surfaces of the high permeability rotor hub. This configuration created an eight-pole magnetic rotor structure. The stator contained 39 slots with the coil windings connected in a 3-phase wye form with 13 slots allocated to each phase.⁵⁰ Sundstrand Corporation has since been involved in high altitude long endurance flight programs. They have designed a samarium cobalt motor capable of performing at an altitude range of 18 to 23 km (60,000 to 75,000 ft) for 3 to 9 months.

The motor/controller unit is air cooled with a maximum ambient temperature of 35 °C (120 °F) for the Air Force RPV. Ram air flows through the controller first and then to the motor through channels between the stator and the housing. The air flow passages allow heat to be effectively removed from the motor since most of the motor heat is generated by losses in the stator. Because of the high efficiency of the samarium cobalt rotor, losses in the rotor assembly are minimal. The power electronics are mounted on heat sinks to promote heat transfer. When the motor/controller designed for the RPV was run at idle for 8 min without benefit of ram air cooling, the unit temperature increased only 14 °C (57.2 °F) above ambient temperature.⁵⁰

The Air Force RPV was flown in an operating envelope of 0 to 460 m (1,500 ft) of altitude. During flight it was seen that there was a slight lag between airspeed reaction and a change in motor speed command. This can be explained by the inherent characteristics of the electric motor. The propeller will windmill after a reduction in rotational speed (r/min) is called for until the speed of the vehicle is reduced correctly. This differs from gasoline engines because in their case the propeller causes drag on the vehicle as the compression from the engine maintains a given propeller r/min. The windmilling phenomenon associated with the electric motor removes this drag. However, including power regeneration into the controller could have eliminated the windmilling effect.⁵⁰

B. Controller

An electric controller will accompany the permanent magnet motor to enable the motor to perform properly. A controller consists of an inverter and motor control electronics. The output from both the solar cells and the fuel cells is direct current. The controller converts the direct current into a three-phase output to activate the motor. A closed loop speed control keeps output speed and input speed in close relation.

C. Inverter

Sundstrand Corporation opted for a voltage source inverter system over the current source system for a number of reasons, one being the limitation of voltage transients (spikes) which could cause transistors to fail. With a voltage source system, control is furnished by pulse width modulation of the inverter switches resulting in fewer power switches for the system. Because a voltage source system does not have as many elements, the system will have a higher calculated efficiency than the current source method.⁵⁰

D. Reduction Gearing

A reduction gear from the motor will be needed for the propeller to operate at the necessary speeds. The propellers of the Boeing *Condor* are driven through two-speed gear boxes in order to have efficient operation at all altitudes. At about 43,000 ft. of altitude the *Condor* shifts gears. The engine to propeller r/min ratio is shifted from 4.5:1 to 3:1. The *Condor* is capable of cruise speeds in excess of 200 knots at altitude. A well-designed gear can have an operating efficiency of at least 0.98 and reduction gear efficiencies in excess of 0.99 are not uncommon.

A crude estimation of the gear weight has been proven acceptable and is necessary due to the lack of a detailed analysis for gear weight. The gear weight in pounds is assumed to be 0.3 times the maximum motor horsepower. Robert Boucher designed the 27:1 reduction gear for *Solar Challenger* which weighed 0.68 kg (1.5 lb) for a maximum motor power of 4.1 kW (5.5 hp). The crude weight estimation presented above is within 0.14 kg (0.3 lb) of Boucher's design. A typical gear design for a samarium-cobalt motor has a specific power of 7.27 hp/kg (2,461 W/lb) with a gear efficiency of 0.99. A typical dc motor and gear system has a specific power of 573 W/lb with an efficiency of 0.94.

E. Power Conditioning

The general electronics needed to support and integrate the flight systems should also be considered in the propulsion system weight estimation. A variety of terms are used to signify these fuses, switches, circuit breakers, inverters, and transformers such as: power conditioning, controlling, and processing. Typically the weight of the power conditioning required is based on the total amount of power to be managed. In 1978, the power conditioning technology was at a rate of about 23 W/lb. In 1980, the power processing technology at about 49 W/lb and the power control technology at about 0.90. A schematic of the HASPP power system is shown in figure 13.

F. System Efficiency

In order to derive a propulsion system efficiency, the efficiencies of the various components are multiplied together. These components are illustrated by figure 13 and their efficiencies are listed in this chapter (with the propeller efficiency of the Boeing *Condor*) as: motor, 95 percent; reduction gear, 99 percent; power conditioning, 90 percent; and propeller, 90 percent. Thus, the propulsion system efficiency is 76.18 percent.

There is really no alternative to the rare-Earth magnet motors on a HASPP. Likewise, the samarium-cobalt motor is the choice of the rare-Earth magnet motors because of its efficiency, reliability, and the research that has gone into these motors for RPV's.

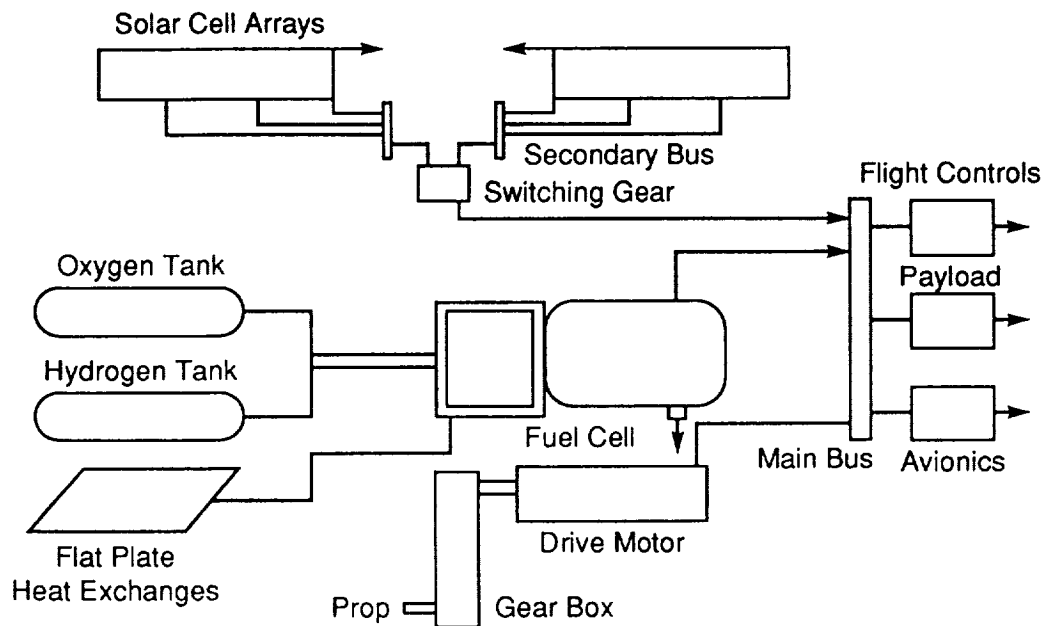


Figure 13. HASPP power system.

Chapter X. PAYLOAD

The payload for the proposed mission will be the agricultural sensors, data collection and processing devices, and the means to transfer the data to a ground station for further processing. As described in part II the weight and power requirements of the payload are necessary in order to size the airplane. An additional consideration will be the volume of the payload.

An added benefit of the HASPP would be the breakthroughs in remote sensing technology necessary to develop the payload for the given mission. The HASPP will be a practical laboratory for furthering the progress in the field of temporal data gathering. Given the length of time the HASPP will be in service, the effects of diurnal and other temporal changes can be examined in detail. This research could, in turn, result in greater improvements in phenomenological monitoring. As of 1984, only very basic remote sensing techniques were available. There were no remote sensing systems for satellites capable of providing near real-time information or high spatial resolution. The remote sensing systems that are in use and being developed are primarily designed for satellite imagery. Therefore, data processing systems to convert the information obtained into usable crop statistics will be needed.

The sensors will provide information on crop growth, water conditions, insect infestation, and disease present in the crops. These images are obtained using a variety of frequency bands. Plants and soils either give off or reflect radiation in several parts of the electromagnetic spectrum. Different levels of radiation are reflected from a healthy plant than from a stressed plant. These differences can be measured from recorded images of the crops. Each category of crop difficulty will give off a unique radiation pattern. In addition, different aspects of crop growth require monitoring at different times in order to be certain the most accurate data is received. Thus, the frequency of coverage is an important aspect in remote sensing of crops. For example, canopy architecture, leaf area index, dry matter, and other aspects are seen most clearly in the morning. Similarly, stress-related properties of plants are best seen within an hour after solar noon.

Occasionally, farmers will currently use color infrared photography to analyze their crops. Ordinary vision and film are sensitive to just a small frequency band within the electromagnetic spectrum; however, color infrared photography captures another band. Each wavelength gives certain data on crops and soils. The wavelengths that can be sensed passively (photography) can be recorded on magnetic tape. The wavelengths that are sensed actively (radar beam) have the reflected images recorded. In the 1960's, images in the visible, near infrared, and thermal infrared radiation wavelength bands were available from airborne sensors. Multispectral scanners flown over agricultural areas proved that the water content of the soil can be determined through the emission of thermal infrared radiation. Some of the visible and near-infrared bands were able to distinguish vegetation. The portable radiometer, used to gather ground data is an aid to satellite imagery. By the mid-1970's, radiometers were hand held or boom mounted. These radiometers measured emitted radiation, with an 8- to 14-micrometer band leading to plant and soil temperatures. There are also radiometers that measure visible, near-infrared, infrared, and thermal bands. The spectrometer is another device used in agricultural monitoring. Ten years ago a backpack spectrometer weighed about 65 lb, today it is hand held and weights 5 lb.

An agricultural sensor on a HASPP should operate similarly to the thematic mapper on Landsat-4. The sensor should operate in five wavelength bands comparable to bands 2, 3, 4, 5, and 6 on Landsat. These bands correspond to the frequencies: 0.52 to 0.60 micrometers, 0.63 to 0.69 micrometers, 0.76 to 0.90 micrometers, 1.55 to 1.75 micrometers, and 0.40 to 12.5 micrometers. A farm with a minimum field size of about 40 acres (161,880 m²) and uniform soils can use a sensor resolution of 30 by 30 m (98.4 by 98.4 ft) corresponding to the thematic mapper. However, most fields are not this large and soils are not usually very consistent throughout a field. For a typical field, the best resolution would be 5 by 5 m (16.4 by 16.4 ft) up to a maximum acceptable resolution of 20 by 20 m.

The first scanning bands, red and near infrared, corresponding to bands 3 and 4 of the thematic mapper show the amount of green vegetation present. Through these, the crop growth can be monitored and the crop yield projected. The sensor bands providing thermal images give data on the water condition of crops. The 1.55 to 1.75 micrometer band is sensitive to plant canopy as well as the water content of the plants. If this band is combined with other bands, then the net radiation absorbed by the crops can possibly be estimated. From this, the amount of water transpired can be estimated, thus the amount of water used by the crops. The visible wavelengths show mineral deficiencies by an increase in the reflectance of radiation.

A possible remote sensing method for the future is laser-induced fluorescence (LIF). Nutrient deficiencies can be detected in crops with the pulsed nitrogen laser. Deficiencies in phosphorous, nitrogen, and iron can be detected through a decrease in fluorescence at 0.69 and 0.74 micrometer. An increase in fluorescence indicates a lack of potassium. Past and current methods of remote sensing of plants typically can not identify the particular nutrient that is deficient. The LIF could be a solution to this problem.

A sensor package that has flown on the C-130 and on the U-2 is the advanced solid-state array spectroradiometer (ASAS). The ASAS is designed for a variety of missions, but it has flown agricultural monitoring missions over Kansas and for the forest ecosystem over Maine. For design purposes, the ASAS will be the assumed payload in the HASPP.

The ASAS has 32 spectral channels, corresponding to wavelengths in the visible and near-infrared range. The array of detectors is 512 by 32 or 16,384 detectors. Each spectral channel sees 14 nanometers, therefore, it ranges from 440 to 855 nanometers. The ASAS has a field of view of 25°

$\pm 12.5^\circ$, with a spatial resolution of 0.85 milliradians (mr). The spatial resolution is also called the footprint and is calculated according to the altitude as:

$$0.85 \text{ mr} \times 20 \text{ km} = 17 \text{ m.} \quad (85)$$

ASAS has a corresponding scan width of 8.7 km at 20 km.

This sensor package is 60.9 by 45.72 by 38.1 cm (24 in high by 18 in wide by 15 in deep) and weighs 90.79 kg (200 lb). This includes an internal cooling unit, but does not include the data recording units. These will not be necessary since a down link to the farmers is planned. The ASAS uses 200 W of 28 V power and requires no consumables.

The ASAS was chosen for the payload primarily because it is the only choice. As stated, the development of a HASPP for an agricultural mission would necessitate the continued development of remote sensing technology. In the absence of a sensor package tailored to the proposed mission, the ASAS will serve the purpose.

Chapter XI. AVIONICS

The weight and power requirements of the avionics aboard the HASPP are needed to complete the aircraft sizing as well as the energy storage system and energy production system sizing. The avionics power is first seen in the calculation for the total power required for flight, equation (1). In addition, the avionics weight is needed to determine the wing loading and in turn the aspect ratio as seen in equation (22).

Cary Spitzer of NASA's LaRC estimates the weight of the avionics in an RPV of at least 1,000 lb as 3 percent of the takeoff gross weight. The power requirement is estimated at 6 W/lb. These estimates are for modular avionics rather than black boxes. Black boxes are 10 to 30 cm (4 to 12 in) by 460 mm (18 in) by 20 cm (8 in), whereas modular avionics are about the size of a breadbox with modules of 13 mm (0.5 in) by 50 mm (2 in) wide.

The Boeing *Condor* has two Delco Magic 3 flight control computers. The second computer is a redundant feature included for dependability. The entire flight profile for the *Condor* is programmed into the computers before takeoff to ensure autonomous behavior. Navigation on the test model is through a strap-down inertial navigator. Boeing has plans for future UAV's to use the Global Positioning System for navigation worldwide. The flight profile can be altered during flight through a communications link with the airplane.

Chapter XII. WIND AND ATMOSPHERE STUDY

As stated in the design procedure, there is a requirement imposed on the HASPP that it be able to station keep against 90-percentile winds. Therefore, it is necessary to have an estimate of the winds aloft during the time of flight. These winds will be a determining factor in the design speed of the HASPP and ultimate feasibility. A wind study has been performed at locations around the world to examine the operating environment a HASPP would experience. NASA/Wallops Flight

Center established the guidelines for the study while researching the feasibility of a HASPP. The National Climatic Center of the National Oceanic and Atmospheric Administration compiled data on winds for a variety of locations and altitudes.

The data⁵⁴ were taken at several sites in each of three areas: the United States, Europe, and the Pacific. Altitudes from 1,000 millibars (mb) to 10 mb (corresponding to 111 m (364 ft) to 31,055 m (101,855 ft)) were examined. Several years were taken to complete this study resulting in 2,000 to 3,000 samples per location, providing an accurate representation of the average winds aloft.

It was concluded in the study that high altitude winds are at a minimum between the altitudes 18 and 22 km (59,000 and 72,000 ft) in the United States, depending on the time of year. At a 95-percent occurrence, the annual wind speeds in the United States are less than 50 knots (kt) with the exception of the winter season. During winter, the wind speeds are less than 50 kt at an 86-percent occurrence. This means that 86 percent of the time the wind speed is at or below 50 kt. Also, it was concluded that for the United States the low latitudes offer minimum winds in the winter and the high latitudes provide minimum winds in the summer. Table 11 is an excerpt from reference 54 describing the percent of time a HASPP could operate at different design speeds. The percentages allow for complete United States coverage.

Table 11. Wind speeds.

<u>Design Speed</u>	<u>Season</u>	<u>Percent of Time, U.S.</u>
30 kt	Winter	60
30 kt	Spring	90
30 kt	Summer	98
30 kt	Fall	90
40 kt	Winter	75
40 kt	Spring	95
40 kt	Summer	99.6
40 kt	Fall	95
50 kt	Winter	85
50 kt	Spring	98
50 kt	Summer	99.6
50 kt	Fall	98
75 kt	Winter	95
75 kt	Spring	99.5
75 kt	Summer	99.7
75 kt	Fall	99.5

The parameters used in the study are based on the assumption that the data is normally distributed.⁵⁴

Wind information supplied from a synthetic wind profile indicates that wind speeds increase with altitude up to 10 to 14 km (33,000 to 46,000 ft). In the 10 to 14 km altitude range, wind speeds can reach 50 m/s (160 ft/s) in the jet stream. Wind speed decreases above 14 km for an altitude

range and then increases again. Another source on winds indicated that mean winds in January at 120° W. longitude and 40° N. latitude are 46 kt at 60,000 ft and 28 kt at 70,000 ft. In July at 60,000 ft, the mean winds are 3 kt and at 70,000 ft 14 kt.

The data presented in figures 14 through 21 are taken from figures presented in reference 54. Only selected sites around the San Joaquin Valley are examined, just as the only altitudes of interest are 50 and 60 mb, corresponding to 64,000 and 68,000 feet, surrounding the design altitude of 20 km (65,600 ft). From figures 14 to 21, it is estimated that at least 90 percent of the time the wind speed in the vicinity of the San Joaquin Valley at approximately 20 km (65,600 ft) will be 30 kt (50.6 ft/s) or less.

Wind gustiness, or the wind variability over time intervals as short as a few seconds, exists at all altitudes in the atmosphere. The amplitude of the gusts decrease with increases in altitude and gusts at the HASPP operating altitude can be neglected with reasonable accuracy.⁵⁶

A study of the atmosphere is necessary to determine the environment in which the HASPP will operate. The solar radiation has been discussed in chapter IV, while the atmosphere content will be examined here.

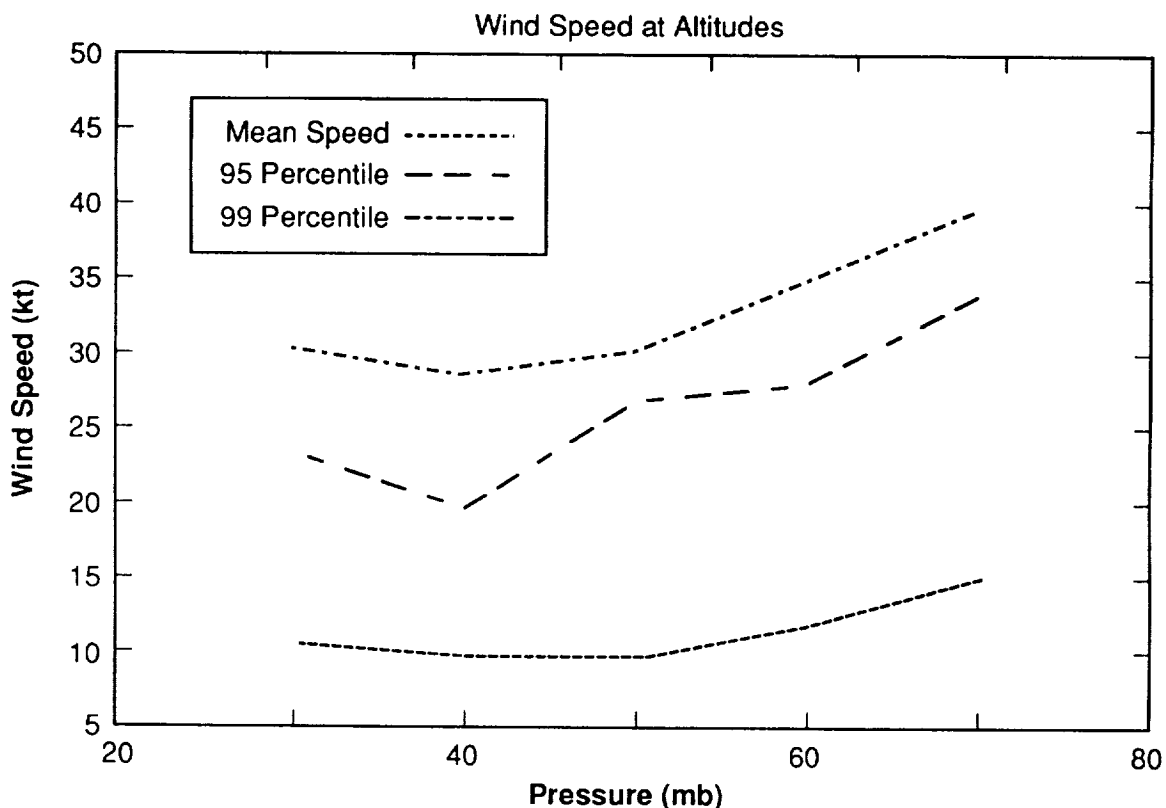


Figure 14. Wind speeds, Oakland, CA, spring.

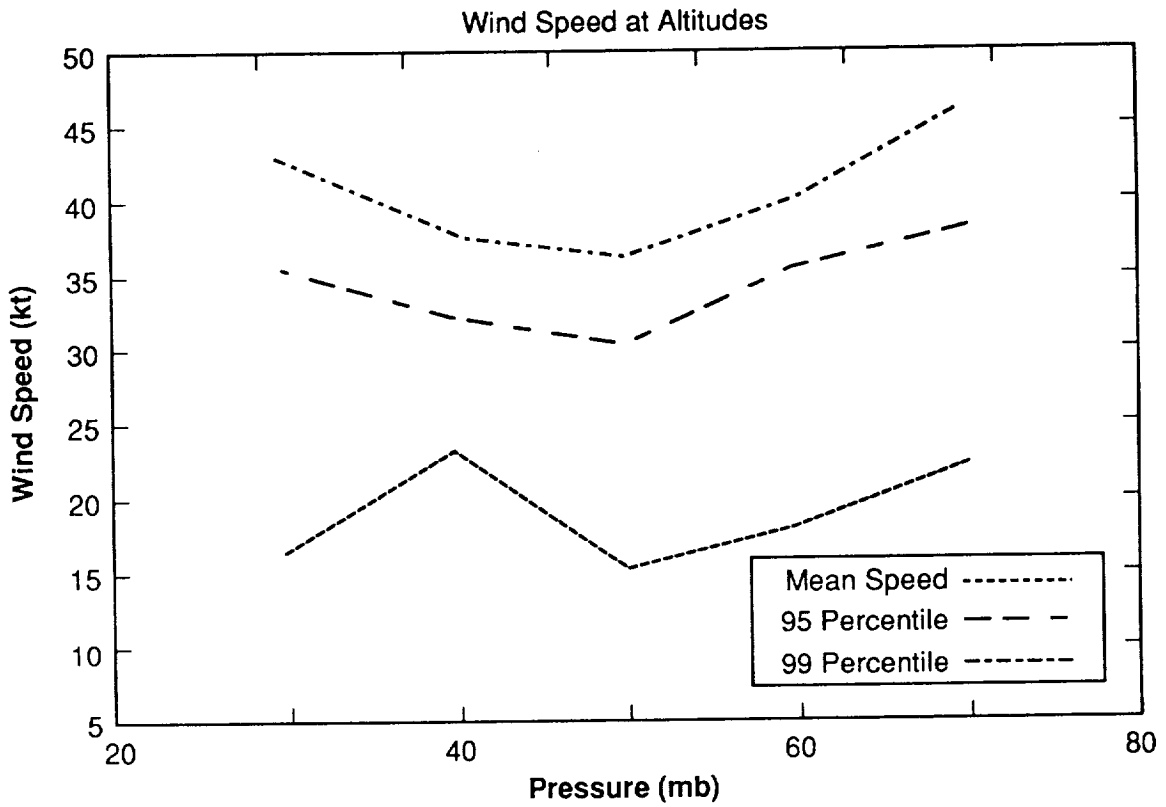


Figure 15. Wind speeds, Oakland, CA, winter.

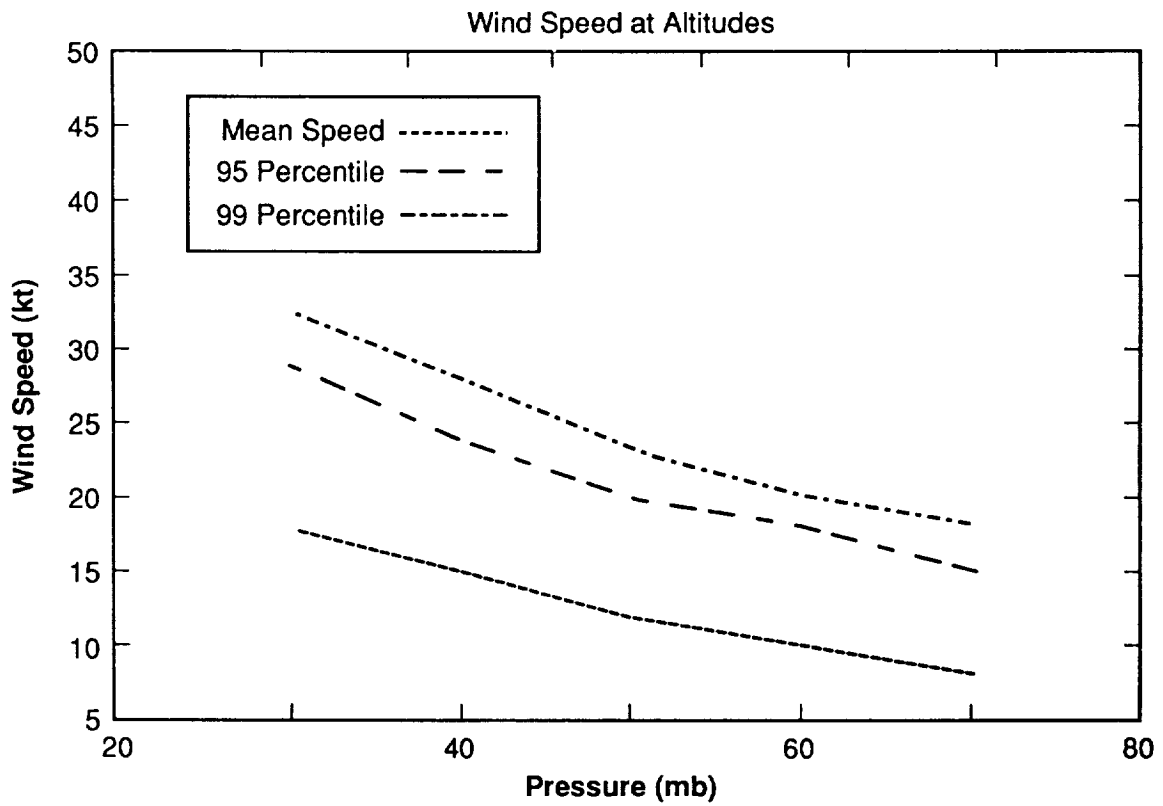


Figure 16. Wind speeds, Oakland, CA, summer.

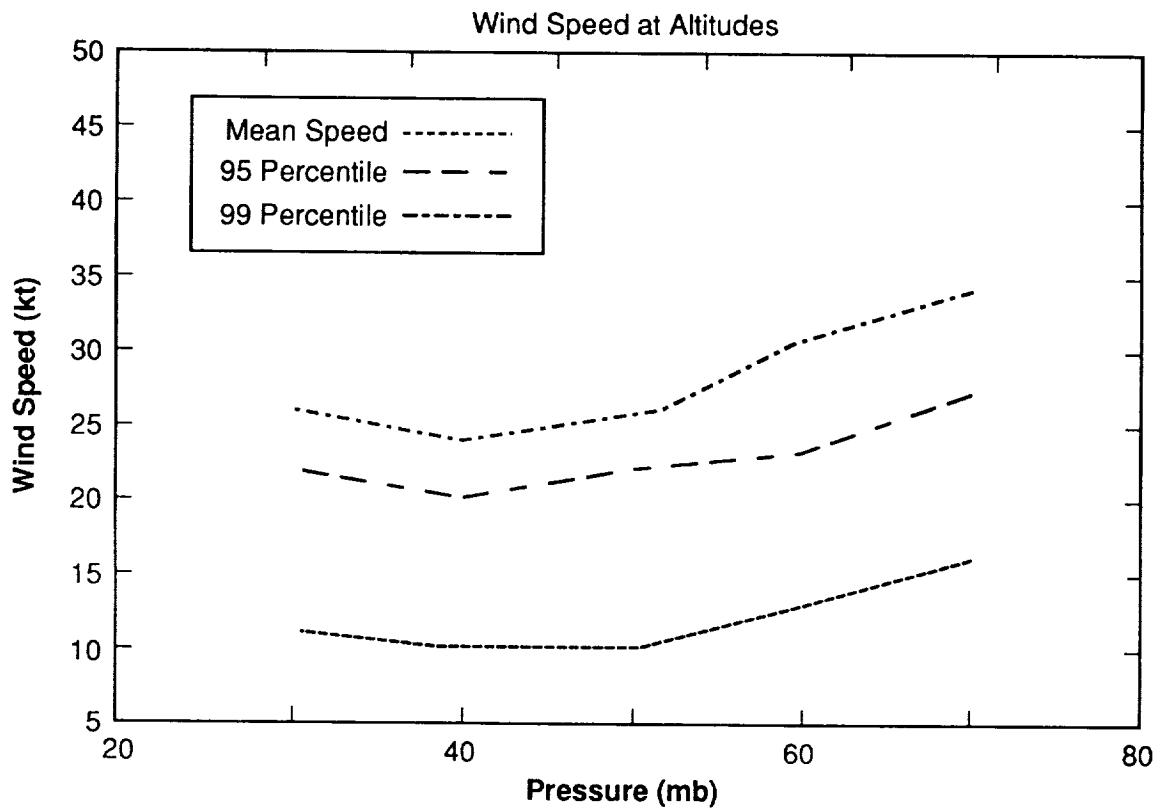


Figure 17. Wind speeds, Oakland, CA, fall.

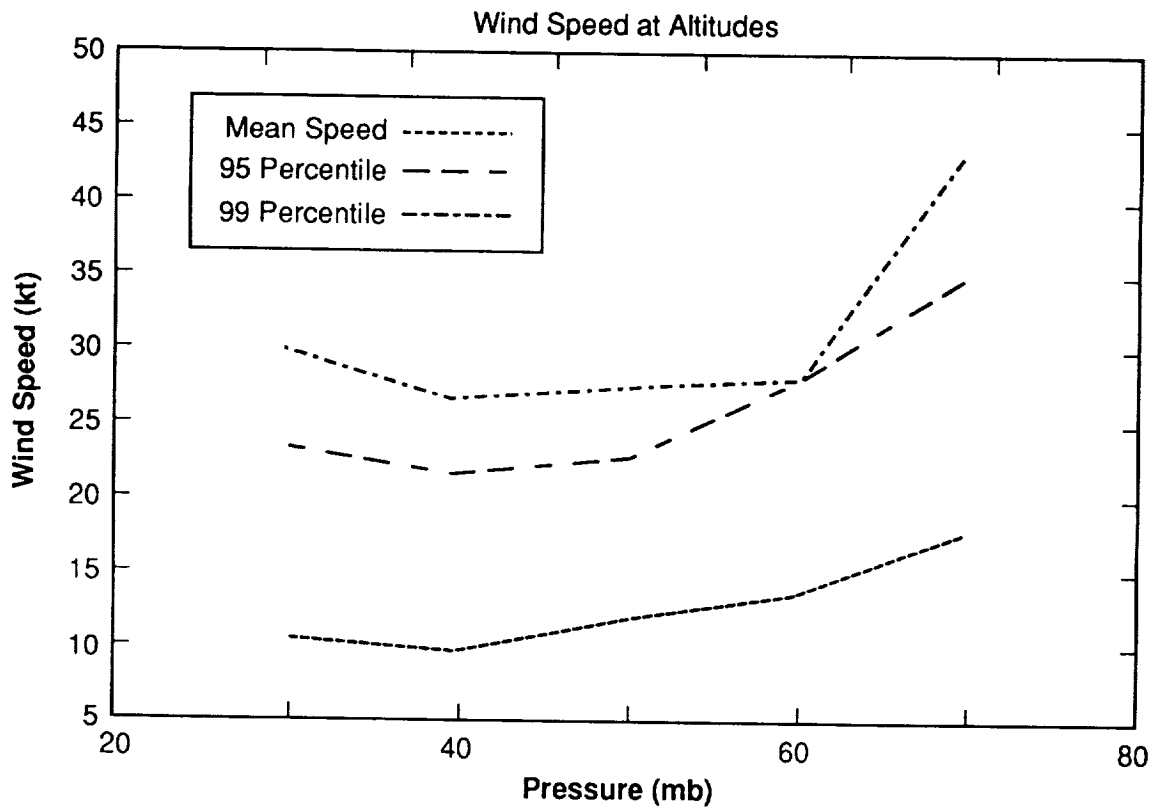


Figure 18. Wind speeds, Vandenberg, CA, spring.

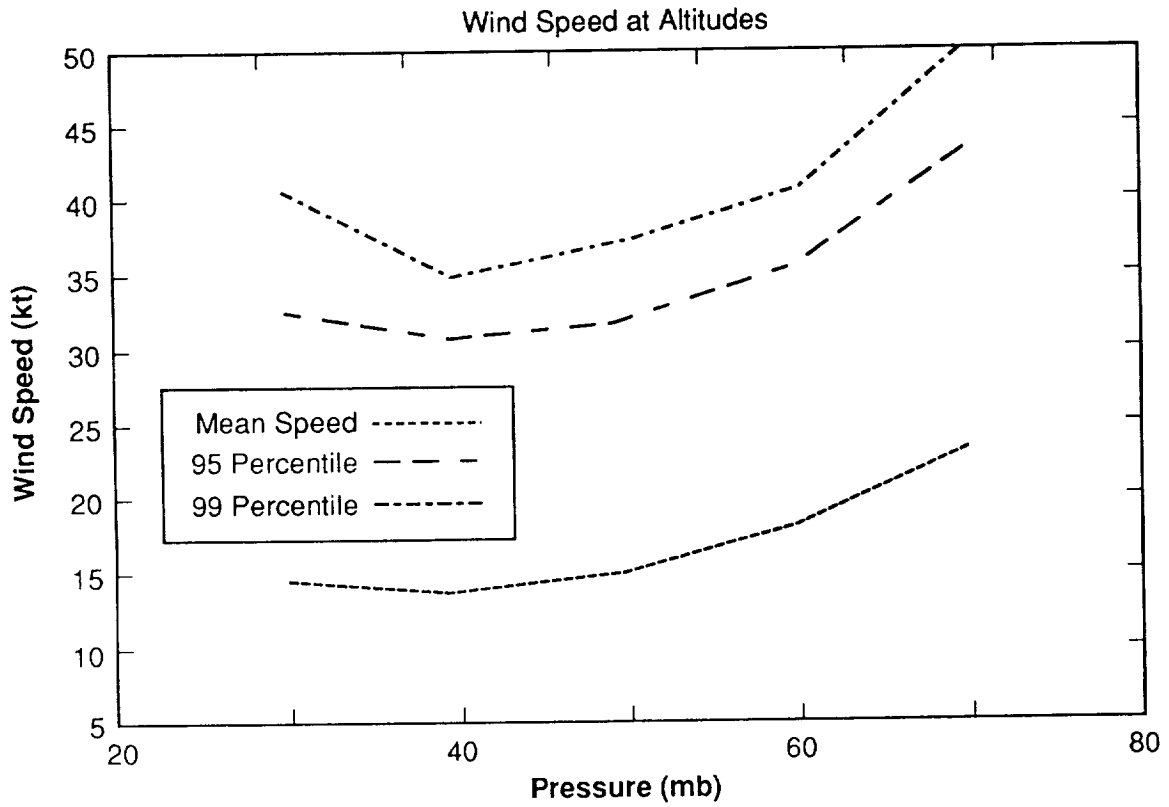


Figure 19. Wind speeds, Vandenberg, CA, winter.

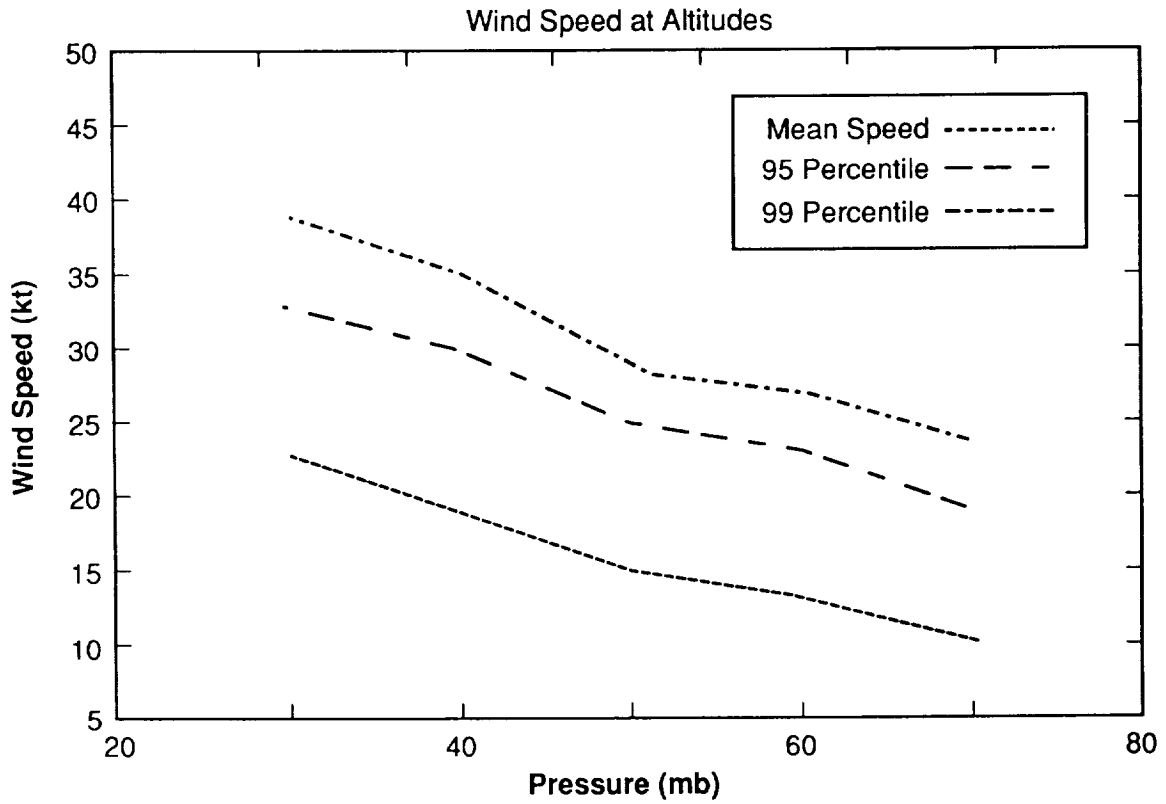


Figure 20. Wind speeds, Vandenberg, CA, summer.

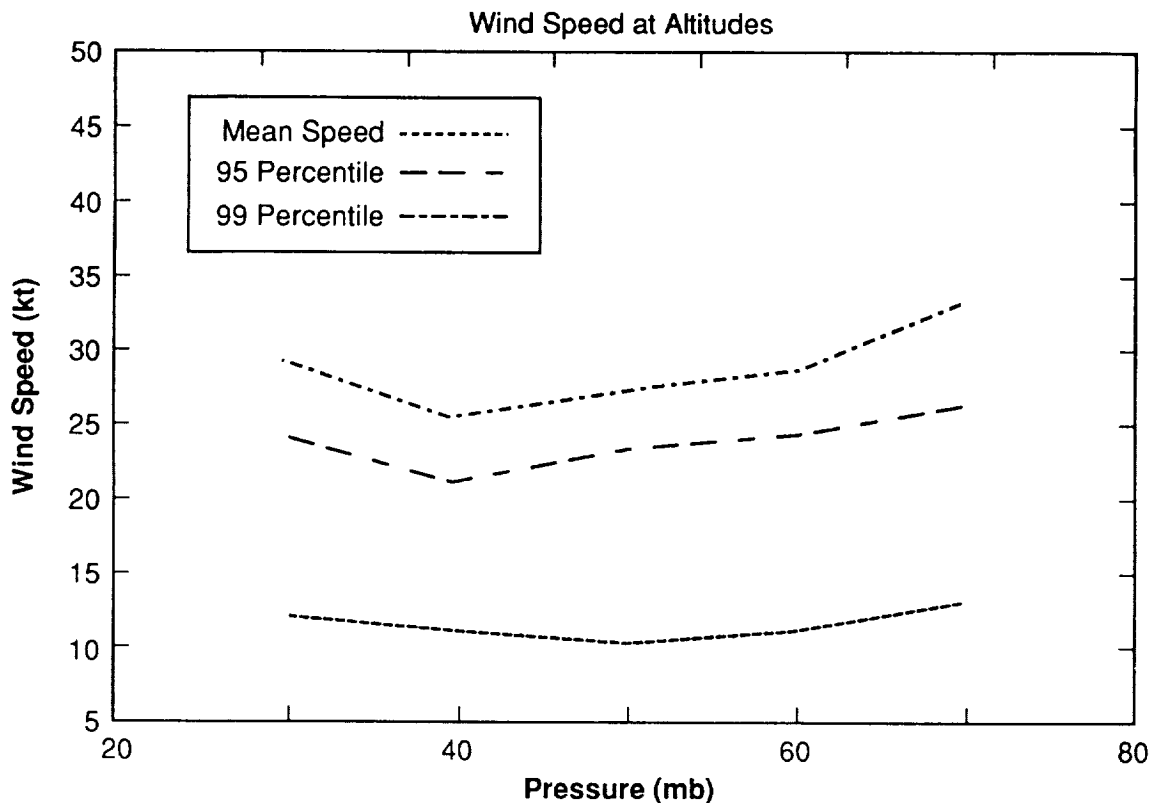


Figure 21. Wind speeds, Vandenberg, CA, fall.

Atmosphere shells are regions of the atmosphere that denote specific altitudes. The troposphere extends from sea level to approximately 8 km (5 mi). All weather occurs in this region which is subject to convection from the Earth. The lower troposphere (15,500 to 45,000 ft) contains cirriform clouds usually composed entirely of ice crystals. Here, the temperature lapse rate is mostly uniform at 6.5 K/km. The Earth's surface extends well into the troposphere with the higher mountain ranges; Mt. Everest peaks just before the transition into the stratosphere. The tropopause is the region within the troposphere of high winds and highest cirrus clouds, which occurs between 6 and 8 km.

The stratosphere begins at approximately 8 km (5 mi) msl (mean sea level) and ends at around 25 km (15 mi), at the middle latitudes, however, it is thicker over the poles and thinner or nonexistent over the equator. The stratopause is a region of the upper stratosphere where atmospheric ozone is a maximum. Also found near this region are the rare nacreous clouds. Temperatures in this region are for the most part constant at about arctic winter temperatures. As stated earlier, winds are at a minimum in this region, from 18 to 22 km and this is the region of proposed HASPP operation. Ozone, formed by the photochemical dissociation of diatomic oxygen by ultraviolet radiation from the Sun, in the stratosphere increases with altitude to about 30 km and then decreases. Maximum atmospheric ozone is about 7 to 10 parts per million by volume. A HASPP at 20 km would be subject to the effects of ozone, O_3 , but not at the maximum concentration possible. Ozone does, however, absorb ultraviolet radiation that would be harmful to the Mylar covering of a HASPP.

Oxidizing agents such as: O_3 , O_2 , and NO_2 cause rubber and plastics to become brittle and/or crack. Ozone is particularly deleterious to rubber under tension. The detriment to plastics is dependent on several factors including the composition of the polymer and the amount of exposure to

the oxidizing agent as well as heat and light. The duration of a HASPP mission at approximately 36° latitude would be dependent on the degradation of the Mylar covering. This degradation may be slowed by using antioxidants which display a synergistic effect.

The amount of water vapor present in the atmosphere is a function of the air temperature, as temperature decreases so does water vapor content. A negligible amount of water vapor exists at temperatures of -40 to -50 °C. As seen in table 8, the HASPP will operate at approximately -56 °C (-70 °F), so water vapor, and hence icing and blocking of solar radiation, will not be a concern.

PART III. METHOD OF ANALYSIS

In this report, a HASPP has been designed to meet the reference mission requirements. The design methodology as stated in part II and shown in figure 1 is followed using information from chapters II through VIII. The solar cell data (chapter V), the motor/controller characteristics (chapter IX), and the theory behind the available energy storage mediums was explored prior to beginning the iterative design procedure. A particular type of solar cell has been chosen for use on the HASPP, with its associated efficiency and weight input to the reference mission parameters. A samarium-cobalt motor/controller has been chosen for the HASPP application, with the weight, efficiency, size, and voltage of the system effecting the overall HASPP design. Similarly, the characteristics of weight, efficiency, size, and voltage of the chosen energy storage medium are input parameters to the design. The choice of an optimum solar cell, motor, and fuel cell has been made based on a study of the available options presented in each section and is also dependent on information stemming from a study of the atmospheric environment, chapters IV and XII.

The daily energy balance algorithm, illustrated by figure 2, requires a study of the solar radiation environment (chapter IV). A computer program has been written to describe the radiation available for the reference mission. Radiation, air mass, atmospheric transmittance, and solar cell power are computed for each hour of each day of the mission. These data have been used to determine the feasibility of flight during the day of least solar radiation.

The design procedure is then completed as described in part II followed by an aerodynamic analysis of the resulting airplane. The construction details (chapter VI) are provided as an estimate for the structural weight and to serve as a baseline for the possible development of a HASPP.

Below is a table representing the decision matrix for the HASPP subsystems. Each of these decisions have been discussed in detail in their respective chapters. The choices listed below occur in the design in the following chapter.

	Comparably Small Size	Lowest Weight	Most Expensive Choice	Highest Efficiency	Reliability/ Durability
GaAs Solar Cells	N/A	No	Yes	Yes	Good
H ₂ -O ₂ Fuel Cells	Yes	Yes	No Data	No	Good
Samarium- Cobalt Motor	Yes	Yes	Yes	Yes	Good
ASAS Payload	Yes	Yes	No Data	N/A	Good
Modular Avionics	Yes	Yes	No Data	N/A	Good

Chapter XIII. DESIGN SOLUTION

A. Solar Radiation

The design solution begins with the solution to the daily energy balance algorithm as illustrated in figure 2. Two computer programs were written to produce figure 22 for the proposed mission. The input parameters to the programs for the previously described mission are as follows:

Table 12. Design input parameters.

Latitude	36
Altitude	20 km
Available solar radiation	1,353 W/m ²
ρ	1.805×10 ⁻⁴ slugs/ft ³
Mission duration	1 year
Payload power	200 W
Payload weight	200 lb
Avionics power	(6) (W_{av}) (watts)
Avionics weight	0.03 (W_{tot}) lb
Gallium arsenide solar cell efficiency	0.21
Fuel cell efficiency	0.65
Propulsion system efficiency	0.7618

The first program, written in BASIC and named SOLAR-1, calculated solar radiation data for any given day. The day, in days from vernal equinox, and the time increment are entered. Solar data may be calculated for each minute of a given day. The data calculated at the given time increment includes the declination angle, the solar hour angle, the sine of the solar elevation angle, the air mass at sea level and at altitude, the atmospheric transmittance, the surface beam radiation, and the power. The power for December 22 is written to a file called SOLAR. The second part of SOLAR-1 determines the total power produced for any given day by a Simpson's integration. Figure 22 illustrates the results of SOLAR-1 and is an illustration of the daily energy balance for the mission described here.

The second program written in BASIC and titled SOLAR-2 calculated the total power available for the HASPP to maintain flight on December 22 based on the solar power produced for that day. The power data for December 22 is input from SOLAR. The number of values of power as well as the time increment in minutes used to produce this number of values has to be input to SOLAR-2. At this point the fuel cell efficiency is entered. A Simpson's Rule integration was used to determine the value at which there is a balance on figure 22 between the area under the upper and lower portions of the curve, with the upper part being multiplied by the fuel cell efficiency since it represents the excess energy stored in the fuel cell. It is assumed that a successful balance occurs if the two areas are equal to within ± 5 W-min/m². The next section of SOLAR-2 produces the available power versus the needed power, the avionics power, the payload power, and the resulting propulsion power from equation (1).

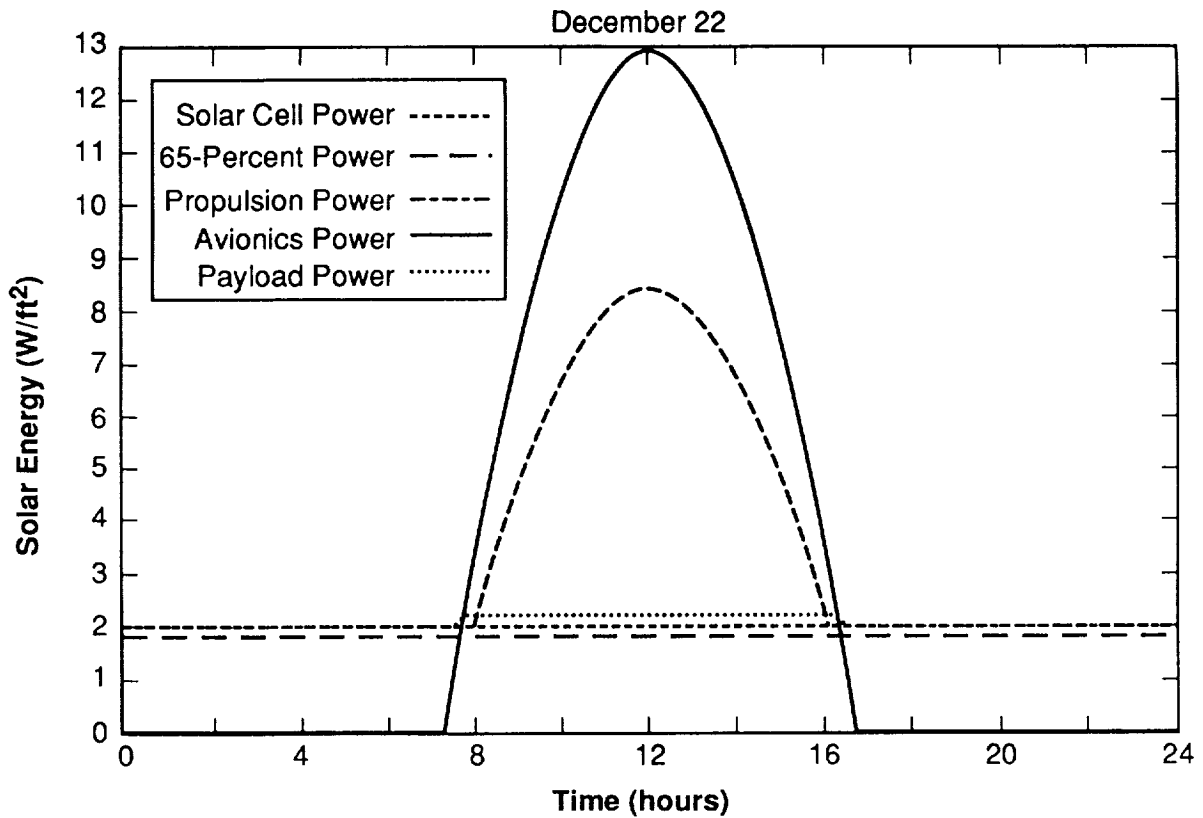


Figure 22. Daily energy balance algorithm.

B. Endurance Parameter

As shown earlier, the avionics power is a function of the avionics weight which is a function of the takeoff weight of the aircraft. In addition, the solar cell power, and, as a result, the total power available has been calculated in W/m² up to this point with the payload power and avionics power given in watts. The design at this point becomes dependent on factors to be determined during successive iterations of the design process. However, a range of wing areas and total weights can be used here and adjusted in following iterations of the design procedure. Estimates can be taken from Youngblood's⁶ 1982 design which resulted in a total aircraft weight of 2,472.6 lb and a wing area of 294.81 m² (3,170 ft²). Recalling that equation (7) is:

$$W_{tot}/S_w = [(P_{tot}/S_w - P_{av}/S_w - P_{pl}/S_w)(\rho/2)^{1/2}(C_L^{3/2}/C_D)(\eta_{prop}/1.356)]^{2/3}, \quad (7)$$

and using a density of 1.805×10^{-4} slugs/ft³ from table 7 along with information from table 12, the wing loading can be expressed as a function of the endurance parameter. Equation (7), for English units, becomes:

$$W_{tot}/S_w = [(P_{tot}/S_w - 6(0.03)(W_{tot})/S_w - 200/S_w)(1.805 \times 10^{-4}/2)^{1/2}(C_L^{3/2}/C_D)(0.7618/1.356)]^{2/3}, \quad (86)$$

or:

$$W_{tot}/S_w = [(P_{tot}/S_w - 0.18(W_{tot})/S_w - 200/S_w)(5.345 \times 10^{-3})(C_L^{3/2}/C_D)]^{2/3}, \quad (87)$$

The total power available to maintain flight for December 22, from SOLAR-2, is:

$$P_{\text{tot}}/S_w = 23.285 \text{ W/m}^2 = 2.165 \text{ W/ft}^2 . \quad (88)$$

Equations (87) and (88) produce the endurance parameter as a function of wing loading. A curve of endurance parameter versus wing loading has been generated for estimated wing loadings from equation (89):

$$C_L^{3/2}/C_D = (W_{\text{tot}}/S_w)^{3/2}/[(5.34 \times 10^{-3})(2.165 - 0.18W_{\text{tot}}/S_w - 200/S_w)] . \quad (89)$$

This curve is shown in figure 23. It is possible that the airplane could have sufficient energy to maintain flight on days of low local solar radiation, but not have enough power to operate the payload. This situation is represented by figure 24, noting from equation (89) that when the payload power is removed the equation is only a function of wing loading.

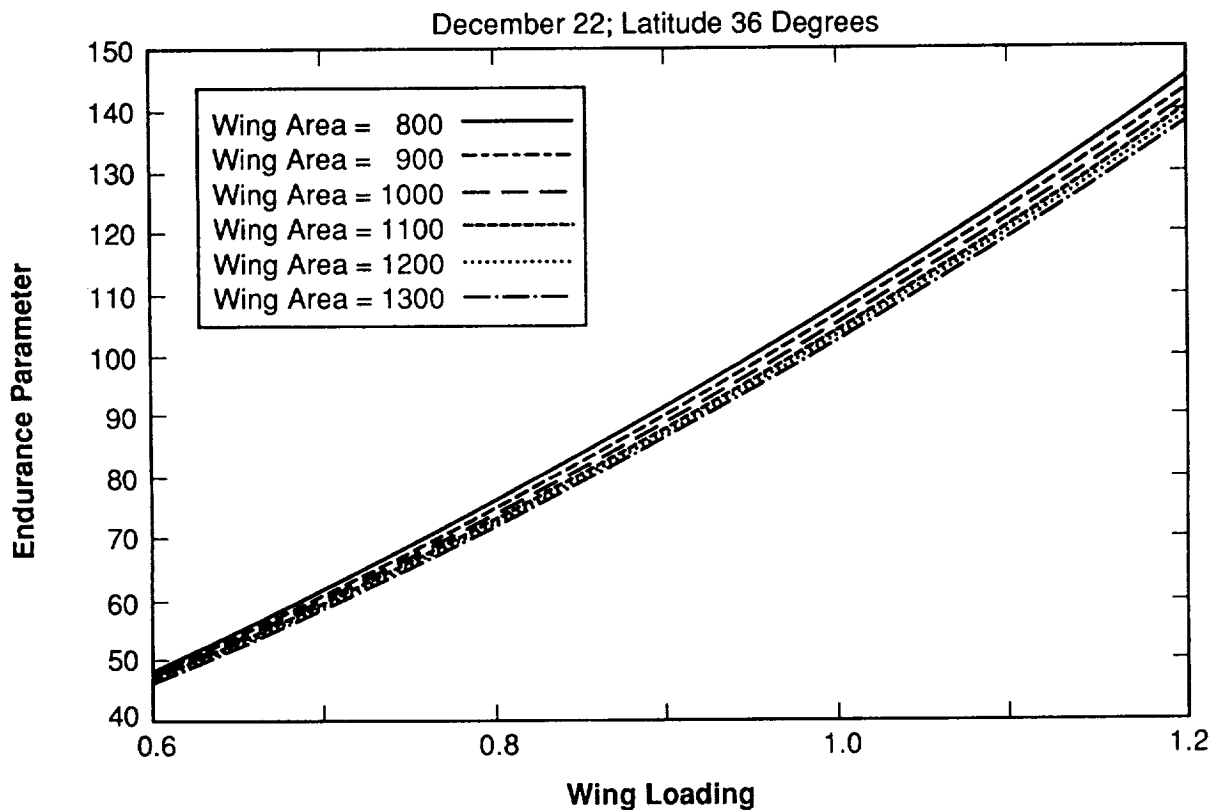


Figure 23. Wing loading versus endurance parameter.

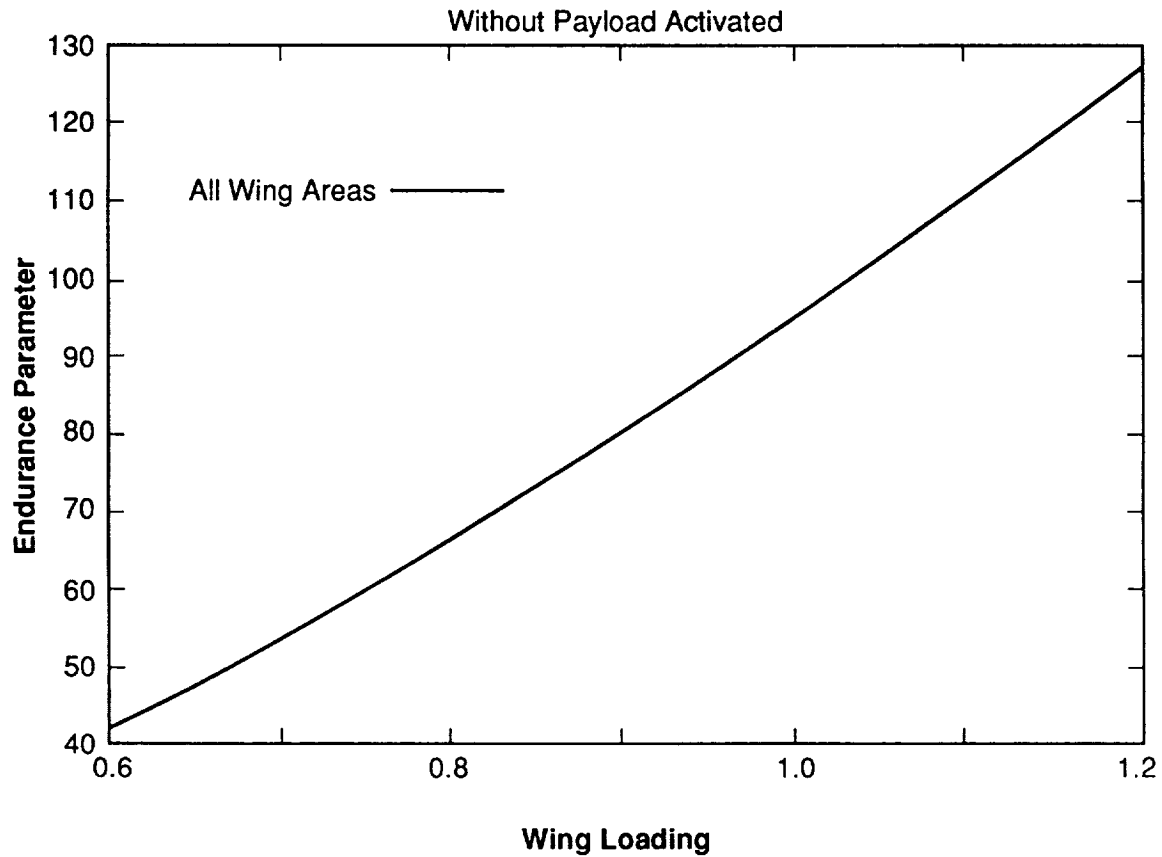


Figure 24. Wing loading versus endurance parameter without payload.

C. Weights

The airplane sizing algorithm, as outlined in chapter III, should be performed now. This algorithm yields the aspect ratio of the wing, the wing span, and the wing area. The airframe loading of the HASPP is expressed by equation (22):

$$W_{af}/S_w = W_{tot}/S_w - W_{prop}/S_w - W_{sc}/S_w - W_{fc}/S_w - W_{pl}/S_w - W_{av}/S_w . \quad (22)$$

The HASPP airframe weight can be estimated by the method intended for sailplanes and modified by Youngblood and Talay^{6 12} as shown in equation (17), and the remaining components of equation (22) can be estimated by equations (18) through (21) and the avionics weight from chapter XI as shown at the beginning of this section. The payload weight from equation (21)⁶ differs from the weight given in chapter X. A payload weight of 200 lb from chapter X is used in this analysis. Thus, equation (21) becomes:

$$W_{pl}/S_w = 200/S_w \text{ lb/ft}^2 . \quad (90)$$

The avionics weight as discussed earlier is given as 3 percent of the takeoff weight of the aircraft or:

$$W_{av}/S_w = 0.03 W_{tot}/S_w . \quad (91)$$

The airframe weight estimation of equation (17) is rewritten as an aspect ratio as shown in equation (23). When equation (22) is substituted into equation (23), the aspect ratio is expressed as:

$$AR = [(W_{tot}/S_w - W_{prop}/S_w - W_{sc}/S_w - W_{fc}/S_w - W_{pl}/S_w - W_{av}/S_w) S_w^{0.222} / (0.310 n^{0.311})]^{2.141} , \quad (92)$$

where n , the ultimate load factor, is 4. Substituting equations (18), (19), (20), (90), (91), and $T_D = 13.2$ h into equation (92) results in:

$$AR = [(W_{tot}/S_w - 0.012 P_{prop}/S_w - 0.150 S_{sc}/S_w - (13.2 P_{tot})/(F * S_w) - 200/S_w - 0.03 W_{tot}/S_w) S_w^{0.222} / (0.310 * (4)^{0.311})]^{2.141} ,$$

or

$$AR = [(0.97 W_{tot} - 0.012 P_{prop} - 0.150 S_{sc} - (13.2/F) P_{tot}) - 200] / (0.477 * S_w^{0.778})^{2.141} . \quad (93)$$

By substituting the estimated specific energy of the fuel cell as given in chapter VIII, $F = 300$ Wh/kg (136.2 Wh/lb), equation (93) becomes:

$$AR = [(0.97 W_{tot} - 0.012 P_{prop} - 0.15 S_{sc} - 0.097 P_{tot} - 200) / (0.477 S_w^{0.778})]^{2.141} \quad (94)$$

(in English units) .

This equation can be further reduced by using the relationship between solar cell area and wing area, $S_{sc}/S_w = 1.00$, as given in chapter III. The result is:

$$AR = [(0.97 W_{tot} - 0.012 P_{prop} - 0.15 S_{sw} - 0.097 P_{tot} - 200) / (0.477 S_w^{0.778})]^{2.141} . \quad (95)$$

The propulsion power can be written as:

$$P_{prop} = P_{tot} - P_{pl} - P_{av} = 2.165 S - 200 - 0.18 W , \quad (96)$$

by combining equation (1) and information on the avionics weight and power requirements. Equation (95) can be further simplified by incorporating equation (96), the given payload power requirement of 200 W, and the calculated P_{tot}/S_w of 23.285 W/m² (2.165 W/ft² or $P_{tot} = 2.165 S_w$ W) from SOLAR-2 as:

$$AR = [(0.972 W_{tot} - 0.386 S_w - 197.6) / (0.477 S_w^{0.778})]^{2.141} . \quad (97)$$

D. Aerodynamics

A curve of aspect ratio versus wing area was generated and is shown in figure 25, keeping in mind that the aspect ratio is a function of the square of the wing span and the wing area as well as being a function of wing span and wing chord. In order to reduce the wide variety of possible wing loadings and wing areas, the aspect ratio limit of 30 is overlaid on the curves of aspect ratio versus wing area. As mentioned earlier, it might be necessary to fly during critical days without the payload operating. This situation would alter equation (96) as well as equation (97).

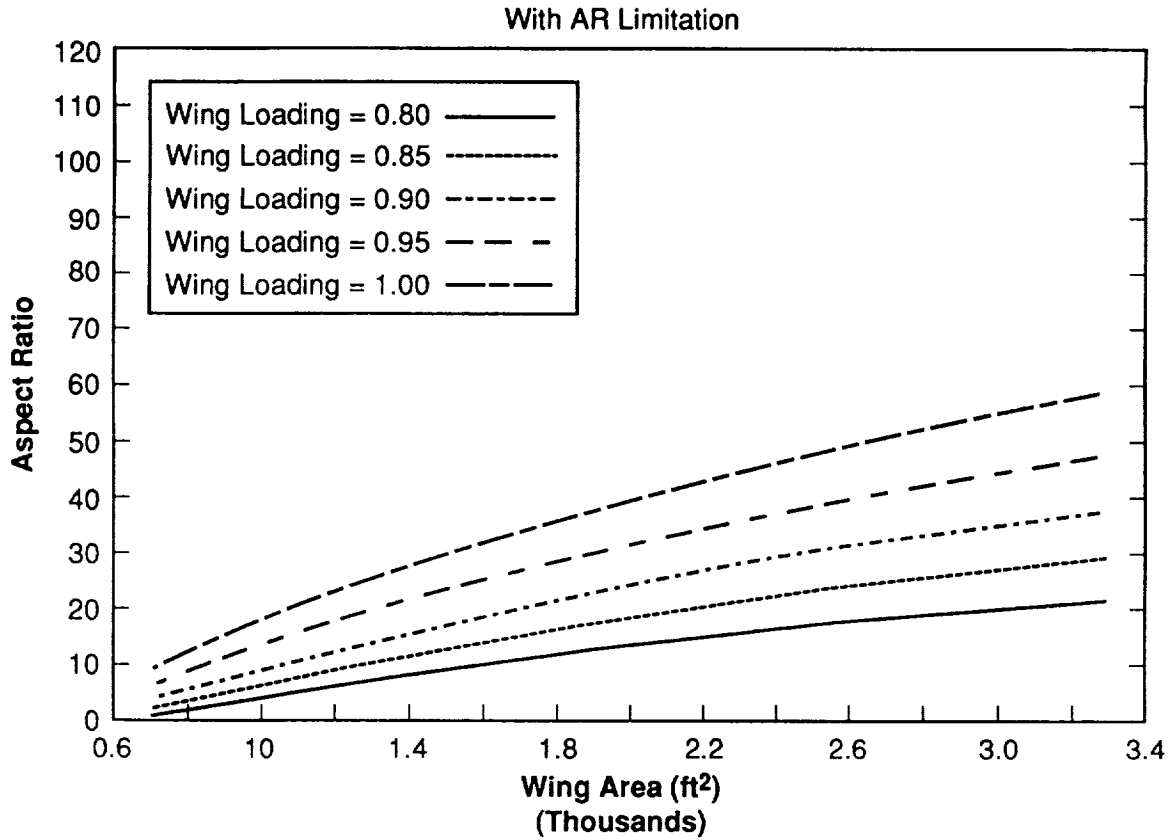


Figure 25. Wing area versus aspect ratio.

The aerodynamics algorithm was invoked to calculate an endurance parameter based on vehicle aerodynamics. Here the drag coefficients are obtained. It was discussed in chapter VII that the drag coefficients from a previous design⁶ are used here. These are seen in equations (25) and (26) and are incorporated into equation (71). Equation (71) for this design is:

$$D_{tot} = \rho/2 V^2 S_w [C_{Dw} + C_{Di} S_l / S_w + C_{Dp} S_p / S_w + C_{Db} S_b / S_w] , \quad (98)$$

or:

$$D_{tot} = \rho/2 V^2 S_w C_{Dtot} . \quad (99)$$

Therefore, the total drag coefficient is:

$$C_{Dtot} = C_{Dw} + C_{Di} S_l / S_w + C_{Dp} S_p / S_w + C_{Db} S_b / S_w , \quad (100)$$

where

$$C_{Dw} = (C_{Dpara})_w + (C_{Di})_w \text{ and } C_{Di} = (C_{Dpara})_l + (C_{Di})_l .$$

Using the values from equations (25) and (26), the total drag becomes:

$$C_{Dtot} = C_{Dw} + 0.36 C_{Di} + 0.06 S_p / S_w + 0.0003 . \quad (101)$$

Coefficients of drag for the wing and tail are taken from drag polars (figs. 21, 22, and 27) for given Reynolds numbers:

<u>Airfoil</u>	<u>Re</u>	<u>C_L</u>	<u>C_D</u>	<u>α (°)</u>
FX-63-137	2.8×10 ⁵	1.20	0.0115	4
FX-63-137	5.0×10 ⁵	1.35	0.01	4
FX-63-137	2.8×10 ⁵	1.68	0.016	10
FX-63-137	2.8×10 ⁵	1.55	0.0145	8
FX-74-CL5-140	1.5×10 ⁶	1.64	0.011	4
FX-74-CL5-140	1.5×10 ⁶	2.02	0.014	8
FX-74-CL5-140	1.5×10 ⁶	2.10	0.014	9
FX-74-CL6-140		1.31	0.0098	4
FX-74-CL6-140		1.45	0.0104	6
FX-74-CL6-140		1.65	0.011	8
FX-74-CL6-140		1.9	0.012	10
FX-74-CL6-140		2.15	0.0142	12
FX-72-MS150B		1.85	0.0115	4
FX-72-MS150B	1.0×10 ⁶	1.70	0.0095	4
FX-72-MS150B		2.15	0.016	8
FX-72-MS150B	1.0×10 ⁶	2.00	0.012	8
FX-72-MS150B	1.0×10 ⁶	2.15	0.014	10

At this point, the endurance parameter based on aerodynamics is calculated. The endurance parameter is:

$$C_L^{3/2}/C_D = C_L^{3/2}/C_{Dw} + 0.36C_{Di} + 0.7536/S_w + 0.0003 , \quad (102)$$

from equation (101) with the pod cross-sectional area determined as twice the necessary payload dimensions from chapter X, as 12.567 ft². The aerodynamic endurance parameter of equation (102), for the variety of airfoils and angles of attack listed above, was calculated and Wortman's FX-74-CL6-140 airfoil was determined to be the best. The minimum wing area for equilibrium flight is found when the endurance parameter calculated from the solar energy balance and aerodynamic requirements are equal. Examining the solar versus aerodynamic endurance parameters of equations (89) and (102), it can be seen that a variety of combinations of wing area and wing loading will result in endurance parameter equalities. The design should be optimized along with consideration being given to structural feasibility. With this in mind, a reasonable aspect ratio is chosen for the HASPP, based on the aspect ratios of a number of sailplanes.⁶¹ The aspect ratio of 15 has been put into equation (97) and this equation:

$$W = 1.738S_w^{0.778} + 0.397S_w + 203.3 , \quad (103)$$

was solved for the total aircraft weight as a function of wing area. Figure 26 is a plot of the solar and aerodynamic endurance parameters for those weights and areas. Recall that some limits were imposed on the design of the HASPP earlier, such as: an upper limit on aspect ratio of 30, a wing

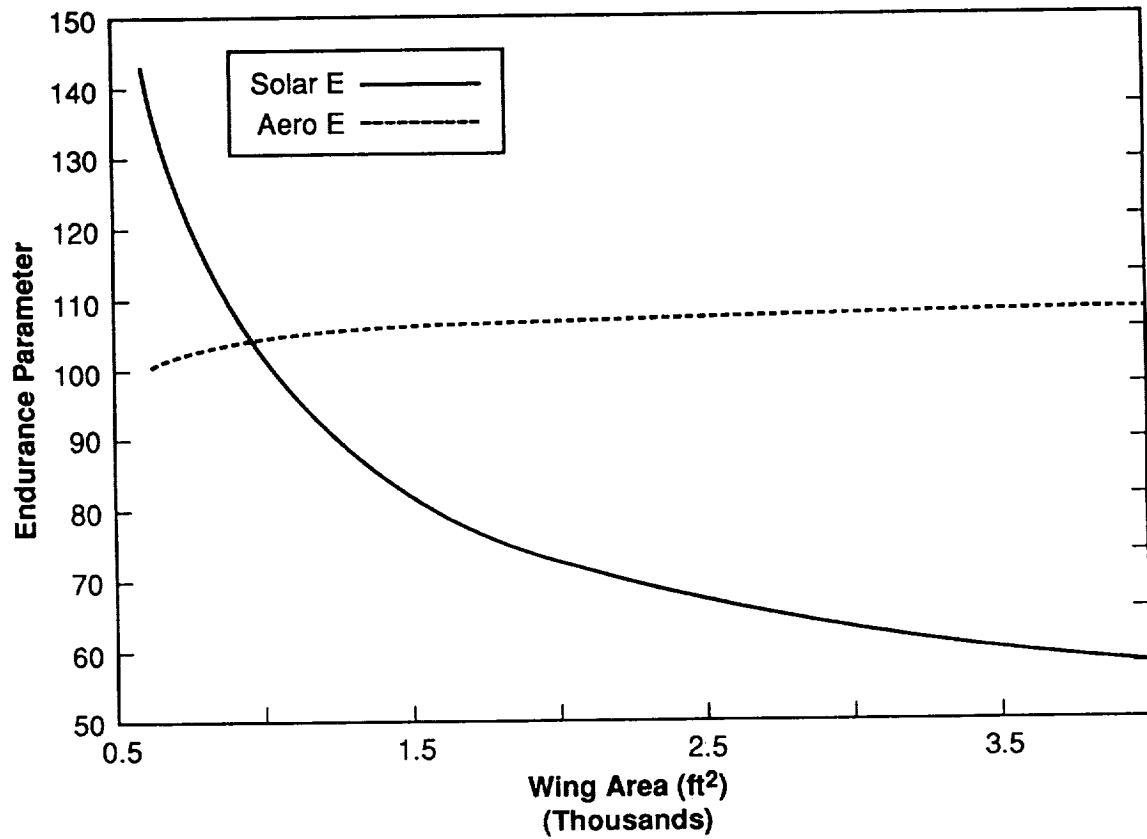


Figure 26. Wing area versus endurance parameter.

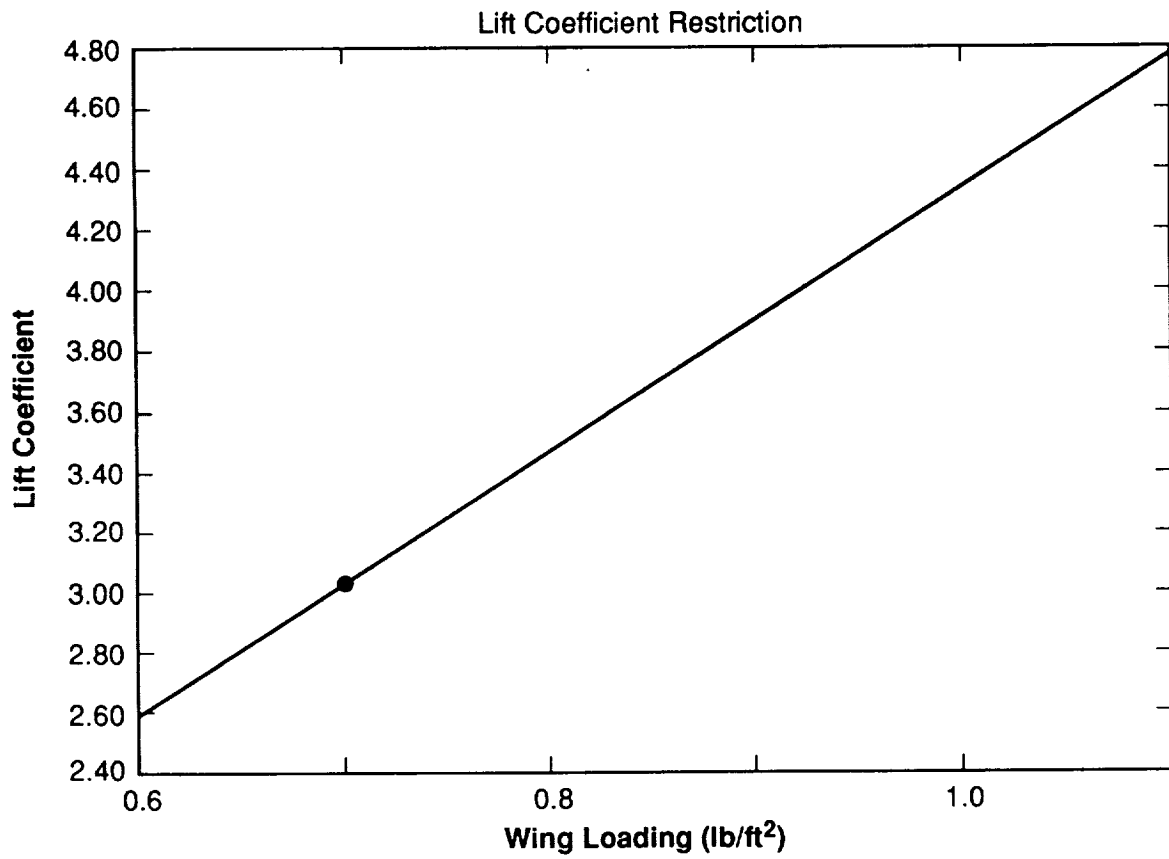


Figure 27. Critical wind speed.

area limitation of 7,000 ft², and a lift coefficient that allows the HASPP to station keep against 90-percentile winds. This critical wind velocity is 30 knots (50.63 ft/s) which makes the critical lift coefficient:

$$C_L \leq C_{L\text{wind}} = 2(W_{\text{tot}}/S_w)/0.463 \quad (104)$$

This restriction is illustrated by figure 27. It can be seen that this restriction is not a concern since the critical coefficients of lift are so high. Nor are the wing area and aspect ratio limitations a concern for this design.

E. Design Specifications

Table 13 is a list of the design specifications found from figure 28, which illustrates a detail from figure 26.

Table 13. Initial design specifications using data from Youngblood.

$P_{\text{tot}}/S_w = 2.165 \text{ W/ft}^2$ $S = 951 \text{ ft}^2$ $S_w = 699.26 \text{ ft}$ $S_t = 251.74 \text{ ft}$ span (tail) = 61.45 ft chord (tail) = 4.10 ft $C_L^{3/2}/C_D = 103.97$ $C_D = 0.0144$ $C_L = 1.31$ $P_{\text{tot}} = 2,058.92 \text{ W}$ $W_{\text{tot}}/S_w = 0.99 \text{ lb/ft}^2$ span, $b = 102.42 \text{ ft}$ $AR = 15$ chord, $c = 6.83 \text{ ft}$ $P_{\text{prop}} = 1,689.86 \text{ W}$, 2.27 hp at Dec. 22, $L = 36^\circ$ $P_{\text{av}} = 169.51 \text{ W}$ $P_{\text{pl}} = 200 \text{ W}$ $W_{\text{av}} = 28.25 \text{ lb}$

Several of the specifications in table 13 come from estimations arrived at in previous designs. With the design specifications of total power, wing loading, and wing area, the weights of the propulsion system, solar cells, and fuel cells can be calculated based on research presented in chapters V, VIII, and IX. Equation (18) estimates the propulsion system weight loading as $0.012 P_{\text{prop}}/S_w$ or 20.28 lb on December 22. The components of the propulsion system, as stated in chapter IX, and their weights become: motor/controller, 26.7 lb; reduction gear, 0.68 lb; power conditioning, 34.49 lb; and propellers, 6.0 lb. The resulting propulsion system weight is 66.87 lb or:

$$W_{\text{prop}}/S_w = 0.04 P_{\text{prop}}/S_w \quad (105)$$

The solar cell weight was given by equation (19) as 142.65 lb. The solar cells are made up of 2 to 4 mil of glass at 0.094 lb/in³, 1 to 2 mil of adhesive, 1/4 mil of Ga-As at 0.192 lb/in³, 1 to 2 mil more of glass, and the necessary wiring which is assumed to be silver at 0.283 lb/in³. The wiring is

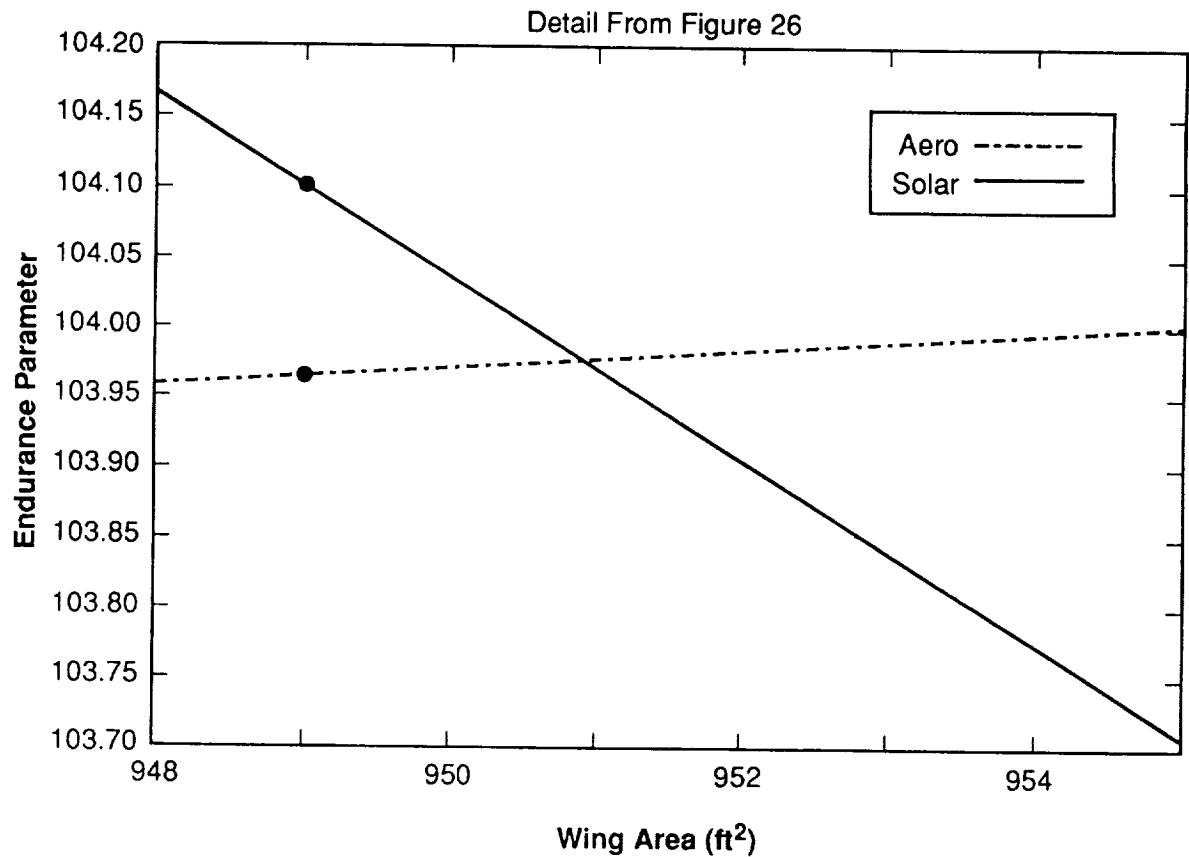


Figure 28. Solar versus aerodynamic endurance parameters.

assumed to cover 9 percent of the solar cell area, which is a negligible weight. The same is assumed to be true for the adhesive weight. With 951 ft² of solar cell area, the resulting weight is 45.19 lb without the wiring or adhesive weight. Equation (19) becomes:

$$W_{sc}/S_w = 0.048 S_{sc}/S_w , \quad (106)$$

with $S_{sc}/S_w = 1.00$.

The fuel cell system weight of equation (20) is 199.54 lb. From information in chapter VIII, a 12.5-kW power plant weighs about 210 lb without the reactants. The weight of the stored H₂, O₂, and their tanks for the P_{prop} and P_{av} of table 13 is 43.61 lb found from information in chapter VIII. With the additional weight of the electrolyzer and fuel cell, it is assumed that equation (20) is still valid for this design.

Substituting equations (105) and (106) along with the previously used equations (90), (91), (20), and (96) into equation (92) yields:

$$AR = [(0.977 W_{tot} - 0.345 S_w - 192.00)/(0.477 S_w^{0.778})]^{2.141} . \quad (107)$$

It can be seen that this compares closely with equation (97) from which the information in table 13 was derived. Figures 29 and 30 illustrate the solar and aerodynamic endurance parameter equality found with this new information by the method described earlier:

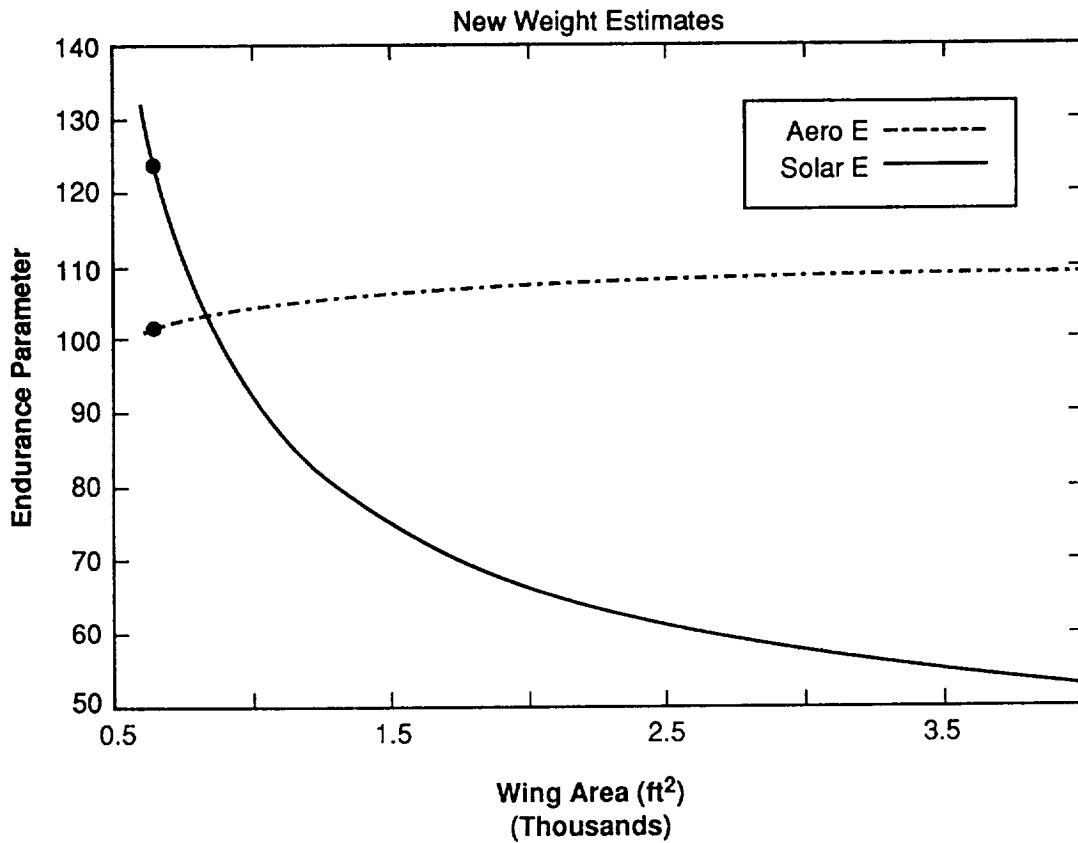


Figure 29. Solar versus aerodynamic endurance parameters.

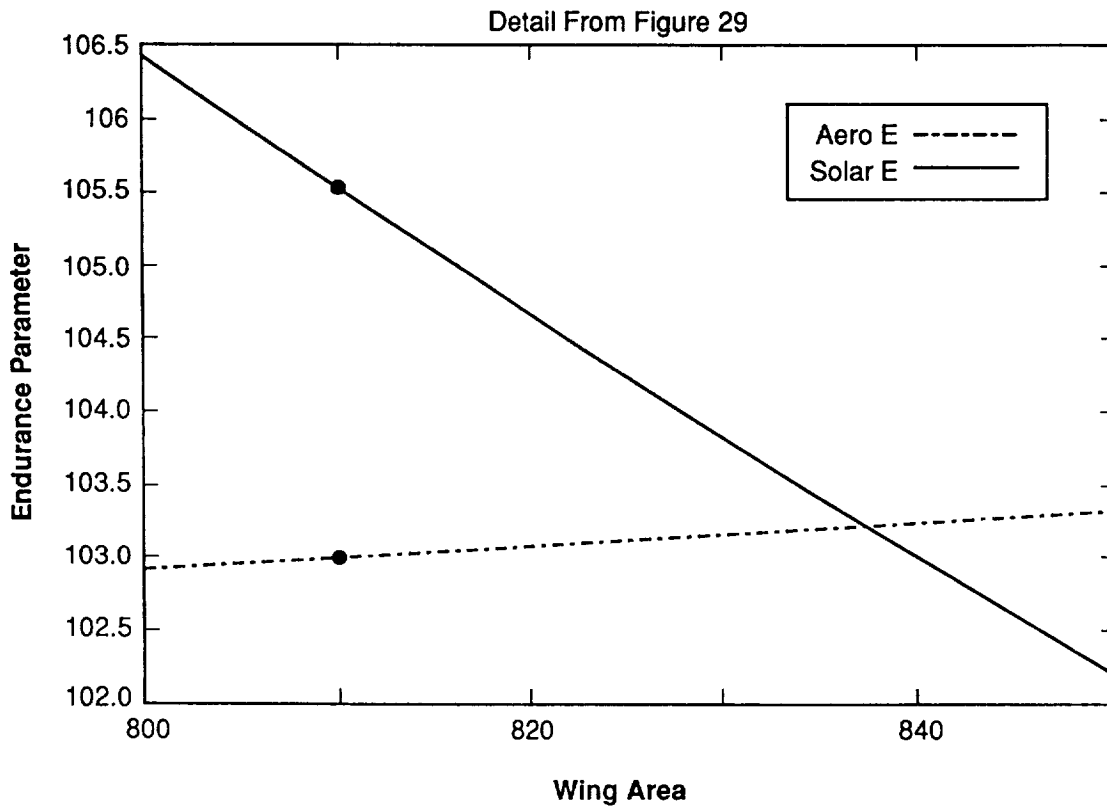


Figure 30. Solar versus aerodynamic endurance parameters.

$$W = 1.729 S_w^{0.778} + 0.353 S_w + 196.52 , \quad (108)$$

with $AR = 15$. Table 14 lists the revised aircraft specifications.

Table 14. Final design specifications.

$P_{tot}/S = 2.165 \text{ W/ft}^2$	$P_{prop} = 1,467.5 \text{ W}$
$W_{tot}/S = 0.976 \text{ lb/ft}^2$	$Re = 351,722$
$W_{tot} = 817.54 \text{ lb}$	$V = 91.70 \text{ ft/s}$
$W_{av} = 24.53 \text{ lb}$	$P_{av} = 147.2 \text{ W}$
$W_{af} \sim 310 \text{ lb}$	
$W_{pl} = 200 \text{ lb}$	$P_{pl} = 200 \text{ W}$
$S = 838 \text{ ft}^2$	$C_L^{3/2}/C_D = 103.2$
$S_w = 616.18 \text{ ft}^2$	$C_L = 1.31$
$S_t = 221.82 \text{ ft}^2$	$C_D = 0.0145$
$b_w = 96.14 \text{ ft}$	$c_w = 6.41 \text{ ft}$
$b_t = 57.68 \text{ ft}$	$c_t = 3.85 \text{ ft}$
$AR = 15$	$L/D = 90.34$

F. Mission and Aircraft Specifications

It should be noted that the ability to fly year-round indicates that flight during the spring, fall, and summer months has more freedom of operation. For instance, on September 20 there is approximately twice the solar power available as on December 22. This extra energy can be used to allow operations at higher latitudes or altitudes, to increase airspeed, or to increase the payload operations. Also, additional energy would be available for corrections in the flight path should relatively high winds blow the HASPP off course. In order to achieve the lift coefficient given in table 14, which allows flight under worse case conditions, the HASPP airfoil has an angle of attack of 4° , which is due to the built-in angle of incidence.

The San Joaquin Valley covers an area from 35° to 40° N. latitude and 119° to 122° W. longitude. During the days of least daylight, the HASPP might need to travel south, to circle at a given latitude, or to raise the nose to maintain flight dependent on the latitude range of the flight path. Figures 31 and 32 are illustrations of the increased freedom of operation the HASPP could experience over a year's time. Figure 31 is a graph of solar and aerodynamic endurance parameters at 36° N. latitude for the mission duration. As before, an endurance parameter equality indicates that flight is feasible at the corresponding conditions. Solar endurance parameters less than aerodynamic endurance parameters imply that there is more than enough energy available to operate at those conditions. Therefore, on figure 31, conditions above the line for a 10° angle of attack are not considered possible since the wing will stall at approximately 12° . Figure 32 offers similar information at 40° N. latitude.

The HASPP configuration is a monoplane with one motor turning two in-line two-bladed propellers. One propeller will be a tractor type and the other a pusher. They are in-line and along the longitudinal axis of the airplane so as not to create any asymmetrical thrust problems should one propeller experience difficulties. The airplane design is a twin-boom tail type, with the oversized horizontal stabilizer and two rudders on either side of the tail.

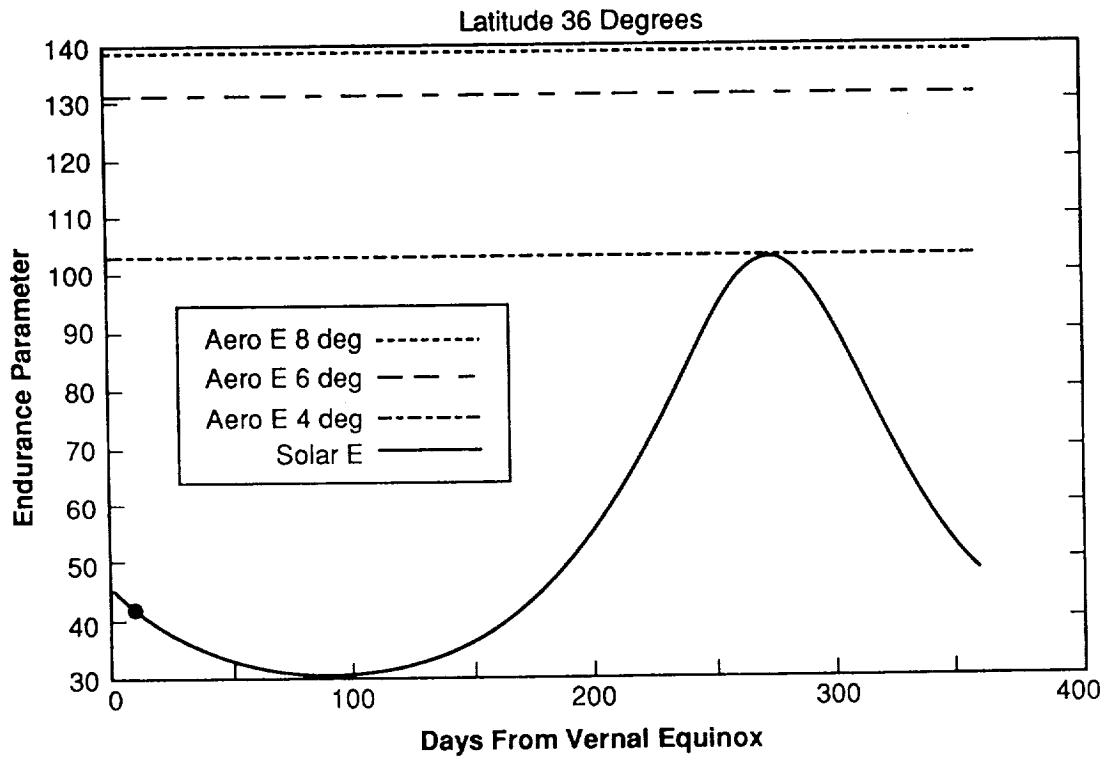


Figure 31. Change in flight conditions with time, latitude 36°.

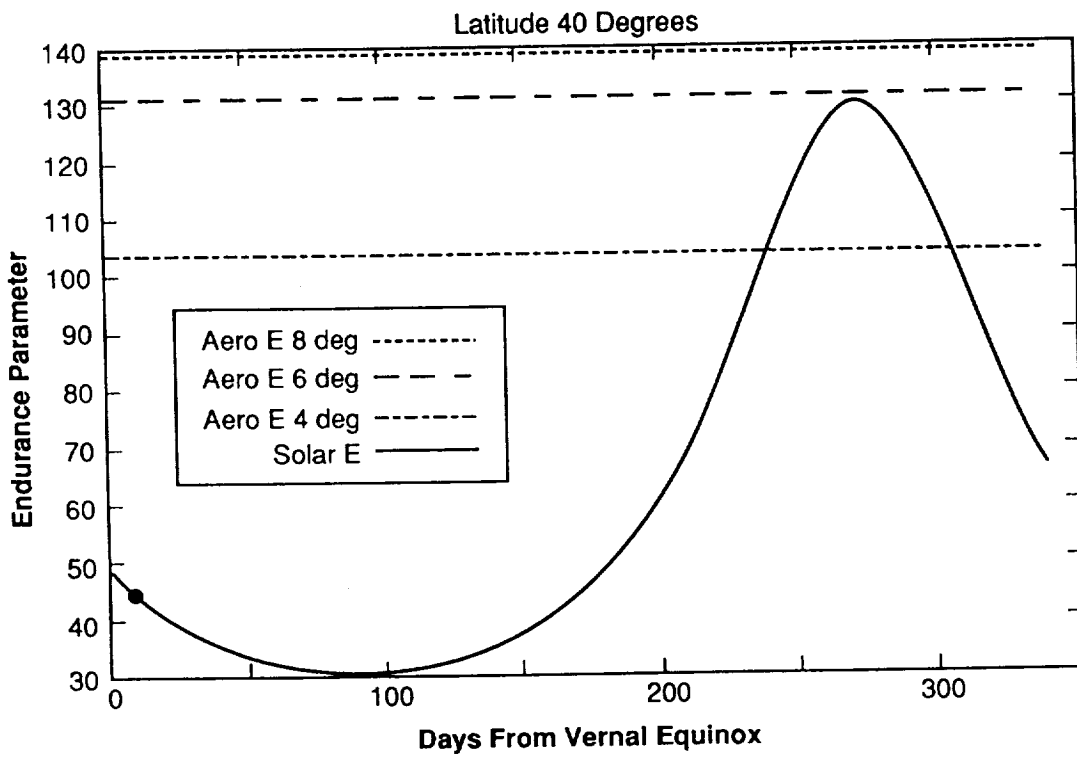


Figure 32. Change in flight conditions with time, latitude 40°.

Creating a power required curve illustrates the velocities corresponding to certain angles of attack as well as the associated power settings necessary to obtain this velocity. This curve is created using equations:

$$L = (\rho/2)V^2S_wC_L , \quad (5b)$$

and:

$$D_{tot} = (\rho/2)V^2[SC_D(\alpha)+S_{para}] . \quad (71)$$

Points on the P_{re} versus V curve are formed in two steps. The first step is to use equation (5e):

$$V = [2W/(\rho S_w C_L)]^{1/2} , \quad (109)$$

with the substitution of $W = L$. An angle of attack is assumed and the associated C_L value is taken from figure 21, resulting in a velocity from equation (109). The next step is to take the C_D value from figure 21 for the same α and equation (5d) for power required. Equation (71) is substituted into equation (5d) yielding:

$$P_{re} = (\rho/2)V^3[S_w C_D(\alpha)+S_{para}] . \quad (110)$$

The velocity in this equation is that derived from equation (109). The parasite area, S_{para} , refers to the coefficients of parasite drag for the various airplane parts except the wing as given in equations (25) and (26). Thus, equation (110) becomes:

$$P_{re} = (\rho/2)V^3S_w[C_{Dw}+0.36C_{Dr}+0.7536/S_w+0.0003]1.356/0.7618 . \quad (111)$$

Figure 33 shows the velocities associated with a range of angles of attack for the data in table 14. At a level flight attitude and at 36° latitude, the HASPP will travel at 27.91 m/s (91.70 ft/s, 54.3 kt, or 62.53 mph). On June 19, the HASPP would have a vertical rate of climb, V_c , of 185.3 ft/min from equation (54). Stalling speed of the aircraft is approximately 70.9 ft/s. Flying a racetrack course of radius 4.35 km (14,300 ft), dictated by the sensor scan width, the airplane will travel 288,000 m (944,000 ft) and begin the 180° turn of radius $r = 4.35$ km (14,000 ft). The angle of bank associated with this turn would be calculated from:³⁸

$$\gamma = \tan^{-1} (V^2/(g r)) . \quad (112)$$

as 1.05° at 1 g.

The flight path described above allows for the same area to be covered approximately twice a day during daylight hours, or four times in a 24-h period. Coverage by sensor scans would be greater and would encompass an area 169.48 nm (1,030,000 ft) by 9.40 nm (57,000 ft) or 1,250,000 acres (5.45×10^{10} ft²) which is 1,900 mi². The HASPP will actually fly through 2.7° of latitude and 0.08° of longitude. The design latitude of 36° is an average chosen for convenience, the airplane might need to fly nose up during the critical days of winter as it passes through the higher latitudes or it could circle at the lower latitudes until more sunlight was available.

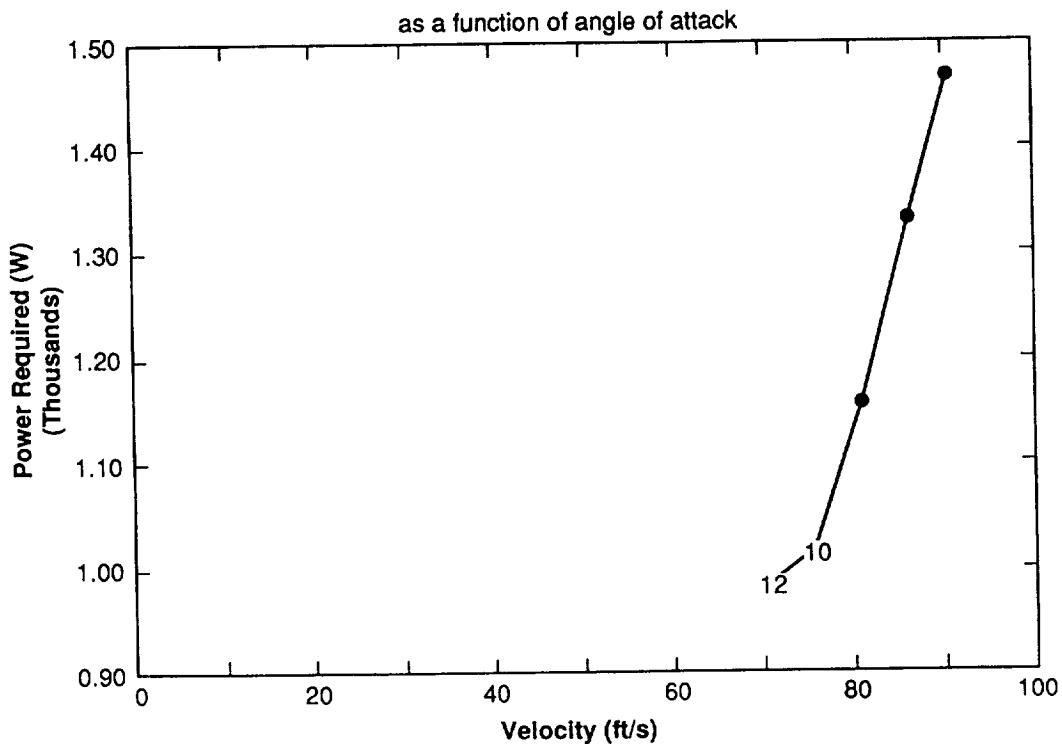


Figure 33. Power required curve.

Chapter XIV. CONCLUSIONS

In conclusion, this design study has demonstrated that with current or near current technology it is possible to build a HASPP capable of flying a mission for twelve continuous months. The future aspects of this design include: refinement of the design, vehicle dynamics analysis, control system design, specification development, definition of launch and recovery procedures, and prototype testing.

An agricultural monitoring mission has been presented for a HASPP because of the recognized need for improved crop management techniques. Also, information on agricultural monitoring needs is readily available. However, as stated previously, a HASPP has the capacity of functioning in a number of roles. In fact, the HASPP designed in this paper is capable of carrying an additional 132 lb and still maintaining flight year round at 36° latitude with a 6° angle of attack during the critical winter days. This would, of course, mean higher angles of attack at higher latitudes, but flight under these conditions is still feasible. The 90-percentile winds at altitude, that the HASPP should be designed to compensate for, are less than the stalling speed of the aircraft at a 12° angle of attack, therefore, the nose up flight attitude would not be a concern. The potential increase in payload capacity would allow for additional monitoring of crops (in addition to the capability of performing nighttime sensing during the months of increased sunlight) or the performance of a dual mission. The HASPP could carry equipment to detect forest fires or perform some communication service while providing farmers with needed data.

The final result is a useful airplane of reasonable proportions. Previously it was discussed that \$10 million annually would be available for HASPP manufacture and operation, were farmers willing to pay the same as they pay consultants now. While actual cost figures on the HASPP are not available, this figure is assumed to be more than sufficient. The initial construction and launch of the craft would be costly, as well as the acquisition of the ground facility. Beyond this initialization, the only continuing costs would be the staff necessary to operate the avionics and the down link of agricultural data. When maintenance on the HASPP is necessary, it would be brought down for recovering, replacement of damaged solar cells, and general refurbishment of other aircraft systems.

In short, the HASPP is a superior means of crop management at a reduced cost. The HASPP, as presented in this report or with another mission, is practical and can be a reality. A complete list of the aircraft specifications and a summary of the design is presented in table 15.

The future aspects of this design include: refinement of the design, vehicle dynamics analysis, control system design, specification development, definition of launch and recovery procedures, and prototype testing. Following a detailed completion of this design, a cost analysis would be necessary.

Table 15. Summary of design.

$P_{tot}/S = 2.17 \text{ W/ft}^2$	$P_{tot} = 1,818.46 \text{ W}$	$P_{av} = 147.2 \text{ W}$
$P_{prop} = 1,467.5 \text{ W}$	$P_{pl} = 200 \text{ W}$	
$W_{tot} = 817.54 \text{ lb}$	$W_{tot}/S = 0.976 \text{ lb/ft}^2$	$W_{prop} = 66.87 \text{ lb}$
$W_{av} = 24.53 \text{ lb}$	$W_{af} = 310 \text{ lb}$	$W_{sc} = 39.82 \text{ lb}$
$W_{pl} = 200 \text{ lb}$	$W_{fc} = 199.54 \text{ lb}$	
$S = 838 \text{ ft}$	$S_w = 616.18 \text{ ft}^2$	$S_t = 221.82 \text{ ft}^2$
$b_w = 96.14 \text{ ft}$	$b_t = 57.68 \text{ ft}$	
$c_w = 6.41 \text{ ft}$	$c_t = 3.85$	
$C_L^{3/2}/C_D = 103.2$	$C_L = 1.31$	$C_D = 0.0145$
$L/D = 90.34$	$AR = 15$	$a' = 4^\circ$
$Re = 352,000$	$V = 91.70 \text{ ft/s}$	
Stall angle of wing $\approx 12^\circ$	90-percentile winds = 30 kt (50.63 ft/s)	
$V_{cruise} = 91.7 \text{ ft/s}$ at 36° latitude	$V_c = \text{rate of climb} = 185.3 \text{ ft/min}$ at June 19	$V_{stall} = 70.9 \text{ ft/s}$
Efficiency $_{fc} = 65$ percent	Efficiency $_{sc} = 21$ percent	Efficiency $_{prop} = 76.18$ percent
Design altitude = 20 km (65,600 ft)	Design latitude = 36°	Mission duration = 1 year minimum
Available solar radiation = $1,353 \text{ W/m}^2$ (125.8 W/ft^2)	Atmospheric density = 1.8×10^{-4} slugs/ft 3	
Monoplane; cantilever wings; single motor; two in-line two-bladed props (tractor and pusher); twin-boom tail; two rudders	Course = 4.35 km radius; 287.8 km leg; angle of bank = 1.05° at 1g; covers 2.7° of latitude and 0.08° longitude	Sensor scan coverage = 169.48 nm by 9.40 nm = 1.25 million acres; covered twice during daylight hours (4 times in 24 h)
Could carry 132 lb additional weight and maintain flight year round at 36° latitude at 6° angle of attack.		

REFERENCES

1. Youngblood, J.W., and Jackson, R.D.: "Airborne Reconnaissance in the Civilian Sector: Agriculture Monitoring From High-Altitude Power Platforms." Society of Photo-Optical Instrumentation Engineers 27th Annual International Technical Symposium, August 21-26, 1983.
2. Henderson, B.W.: "Boeing *Condor* Raises UAV Performance Levels." Aviation Week and Space Technology, April 23, 1990.
3. Kuhner, M.B., Earhart, R.W., Madigan, J.A., and Ruck, E.T.: "Applications of a High Altitude Powered Platform (HAPP)." NASA CR 158466, September 1977.
4. Morris, C.E.K.: "Microwave-Powered Unmanned, High-Altitude Airplanes." Journal of Aircraft, vol. 21, No. 12, December 1984.
5. Graves, E.B.: "The Feasibility of a High-Altitude Aircraft Platform With Consideration of Technological and Societal Constraints." NASA TM 84508, June 1982, pp. 60-78.
6. Youngblood, J.W., and Talay, T.A.: "Solar-Powered Airplane Design for Long-Endurance, High-Altitude Flight." AIAA paper 82-0811, 1982.
7. Stender, W.: "Sailplane Weight Estimation." OSTIV, June 1969.
8. MacCready, P.B., Lissaman, P.B.S., Morgan, W.R., and Burke, J.D.: "Sun-Powered Aircraft Design." AIAA paper 81-0916, May 12-14, 1981.
9. Stansell, J.: "Planes That Fly by the Sun." New Scientist, June 25, 1981.
10. Boucher, R.J.: "Project Sunrise." AIAA paper 79-1264, June 13, 1979.
11. Youngblood, J.W., Talay, T.A., and Pegg, R.J.: "Design of Long-Endurance Unmanned Airplanes Incorporating Solar and Fuel Cell Propulsion." AIAA paper 84-1430, June 11-13, 1984.
12. Youngblood, J.W., Darrel, W.L., Johnson, R.W., and Harriss, R.C.: "Airborne Spacecraft—A Remotely Powered, High Altitude RPV for Environmental Applications." Electronic and Aerospace Systems Conference, October 9-11, 1979.
13. Parry, J.F.W.: "A Solar Powered Observation Platform." Defense Advanced Research Projects Agency RDA-TR 4300-088, July 1974.
14. Hall, D.W., Fortenbach, C.D., Dimiceli, E.V., and Parks, R.W.: "A Preliminary Study of Solar Powered Aircraft and Associated Power Trains." NASA CR 36991983, 1983.
15. Hall, D.W., and Hall, S.A.: "Structural Sizing of a Solar Powered Aircraft." NASA CR 172313, April 1984.

16. Jackson, R.D., and Youngblood, J.W.: "Agriculture's Eye in the Sky." *Crops and Soils Magazine*, October 1983.
17. Jackson, R.D.: "Remote Sensing of Vegetation." *SPIE*, vol. 475, *Remote Sensing*, 1984.
18. Interview with Bill Barnes, Goddard Space Flight Center, Greenbelt, MD, August 23, 1990.
19. "Solar Cells for Photovoltaic Generation of Electricity," 1979.
20. "Photovoltaic Energy Program Summary Fiscal Year 1988," vol. I and II, Solar Energy Research Institute.
21. Zweibel, K.: "Second Generation Solar Cells." *The World and I*, May 1988.
22. Irving, F.G., and Morgan, D.: "The Feasibility of an Aircraft Propelled by Solar Energy." AIAA paper 74-1042, September 11-13, 1974.
23. Keith, F.: "Principles of Solar Engineering," 1978.
24. Vogt, S.T., and Proeschel, R.A.: "Space Station Photovoltaic Power Module Design," 1989.
25. "Space Station Battery System Design and Development," 1989.
26. Hubbard, H.M.: "Photovoltaics: Today and Tomorrow." *Science*, vol. 244, April 21, 1989.
27. Personal correspondence with Stan Vernon, Spire Corporation.
28. Personal correspondence with Gary Virshup, Varian, Palo Alto, CA, October 18, 1989.
29. Gale, R.P., KOPIN Corporation, Taunton, MA, October 6, 1989, and January 11, 1990.
30. Personal correspondence with Kim W. Mitchell, ARCO Solar, Inc., Camarillo, CA.
31. Green, M.A., University of New South Wales, Kensington, New South Wales, November 9, 1989.
32. Wortmann, F.X.: "The Quest for High Lift." AIAA paper 74-1018, September 11-13, 1974.
33. Althaus, D.: "Experimental Results From the Laminar Wind Tunnel of the Institut fur Aero- und Gasdynamik Der Universitat Stutart." *Stuttgart Profilkatalog I*, 1972.
34. Ghia, K.N., Osswald, G., and Ghia, U.: "Study of Low-Reynolds Number Separated Flow Past the Wortmann FX 63-137 Airfoil." *Low Reynolds Number Aerodynamics*, June 1989.
35. McMasters, J.H., and Palmer, G.M.: "At the Threshold of Man-Powered Flight." *Astronautics & Aeronautics*, September 1977.
36. Corning, G.: "Supersonic and Subsonic Airplane Design." Braun-Brumfield, Inc., 1970.

37. McCormick, B.W.: "Aerodynamics, Aeronautics, and Flight Mechanics." John Wiley and Sons, 1979.
38. Von Mises, R.: "Theory of Flight." Dover Publications, Inc., New York, 1959.
39. Liebeck, R.G.: "Design of Subsonic Airfoil for High Lift." Journal of Aircraft, September 1978.
40. Miley, S.J.: "On the Design of Airfoils for Low Reynolds Numbers." AIAA paper 74-1017, September 1974.
41. Karpinski, A.P.: "New Application of Silver-Zinc Batteries for Orbiting Spacecraft," 1989.
42. Interview with Paul Prokopuis, NASA/LeRC, March 1990.
43. Interview and personal correspondence with Tom Maloney, Sverdrup, LeRC, Cleveland, OH, February 25, 1991.
44. Bechtel National, Inc., "Handbook for Battery Energy Storage in Photovoltaic Power Systems." DOE contract No. DE-AC03-78ET26902, November 1979.
45. Haas, R.J., and Chawathe, A.K.: "Space Station Nickel-Hydrogen Cell Design and Development," 1989.
46. Interviews with Jeff Brewer, NASA/MSFC, AL, March 1990.
47. Adams, D.R., et al.: "Fuel Cells Power for the Future." Fuel Cell Research Associates, 1960.
48. Appleby, A.J., and Foulkes, R.R.: "Fuel Cell Handbook." Van Nostrand Reinhold, 1989.
49. Interview with Roy Lanier, NASA/MSFC, AL, November 2, 1989.
50. Curran, P., and Faulkner, D.: "A Samarium-Cobalt Motor-Controller for Mini-RPV Propulsion." 17th IECEC, 1982.
51. Curran, P.D., Sundstand Corporation, Rockford, IL, November 6, 1989.
52. Spotts, M.F.: "Design of Machine Elements." Prentice-Hall, Inc., 1978.
53. Interview with Cary Spitzer, NASA/LaRC, VA, March 1990.
54. Stragnac, T.W.: "Wind Study for High Altitude Platform Design." NASA RP-1044, December 1979.
55. Turner, R.E., and Hill, C.K.: "Terrestrial Environment (Climatic) Criteria Guidelines for Use in Aerospace Vehicle Development." NASA TM 82473, 1982.
56. USAF Air Research and Development Command, Air Force Research Division, Geophysics Research Directorate: "Handbook of Geophysics." The MacMillan Co., New York, 1961.


57. Interview with William H. Phillips, NASA/LaRC, VA, June 8, 1989.
58. Interview and personal correspondence with James W. Youngblood, NASA/LaRC, VA, October 25, 1989.
59. Interview with Tom Nelson, DuPont, November 2, 1989.
60. Congiliano, P.E.: "An Experimental Investigation of the Low Reynolds Number Performance of the Lissaman 7769 Airfoil." AIAA paper 83-0647, January 1983.
61. "Soaring," vol. 47, No. 11, November 1983.
62. Department of Energy, Solar Energy Research Institute: "Photovoltaics: Converting Sunlight to Electricity," January 1988.

APPROVAL

HIGH ALTITUDE SOLAR POWERED PLATFORM

By M.D. Bailey

The information in this report has been reviewed for technical content. Review of any information concerning Department of Defense or nuclear energy activities or programs has been made by the MSFC Security Classification Officer. This report, in its entirety, has been determined to be unclassified.

6/20 

J.C. BLAIR
Director, Structures and Dynamics Laboratory



